MACROMOLECULE TRANSPORT IN TUMOURS

MACROMOLECULE TRANSPORT IN TUMOURS: MATHEMATICAL MODELLING AND EXPERIMENTAL STUDIES

By

GEORGE ALEXANDRAKIS, B.A. HON.

A Thesis

Submitted to the School of Graduate Studies

in Partial Fulfilment of the Requirements

for the Degree

Master of Science

McMaster University

MASTER OF SCIENCE (1995) McMaster University

(Physics) Hamilton, Ontario

TITLE: Macromolecule Transport in Tumours: Mathematical Modelling and Experimental Studies

AUTHOR: George Alexandrakis, B.A. Hon. (Oxford University)

SUPERVISOR: Dr. C. S. Kwok

NUMBER OF PAGES: xiv, 147

ABSTRACT

The delivery of immunoreactive macromolecules to tumour cells in solid, heterogeneously perfused tumours is a major problem in the effectiveness of immunotherapy. To help optimize the new experimental treatment method, a published mathematical model of macromolecule transport (Baxter & Jain 1989,1990,1991a) was appraised and verified experimentally. Computational and analytical tools were developed to predict the interstitial plasma fluid pressure and velocity distributions in well perfused spherical tumours. Their published analytical solutions of the formulation were found to have some errors and were corrected in this work. To check the validity of the formulation, a series of animal experiments was performed to quantify the total vascular volume, and plasma fluid extravasation rate in SKOV3ip1 human ovarian tumour xenografts in nude mice. The results compared well with the theoretically predicted total plasma fluid extravasation rate. Computer codes were also developed to predict the spatial and temporal distributions of intact IgG and its $F(ab')_2$ and Fab/Fab' fragments in well perfused spherical tumours using the formulation proposed by Baxter & Jain (1989,1990,1991a). The cases of non-binding and binding macromolecules were treated separately. The codes for both the interstitial pressure and macromolecule distributions were written to include a radially variable vessel surface area for transcapillary exchange per unit volume of tumour tissue (S/V). The sensitivity of the overall tumour perfusion to variation of (a) the macromolecule m.w., binding affinity, and metabolism, (b) S/V, tumour radius, and (c) microvascular permeability were investigated. Comparison of the theoretical predictions with available experimental data leads to the realization of a number of shortcomings in the previously proposed formulations. Finally, a computational method for deriving the effective spherically symmetric spatial distributions for the vascular volume density, and S/V from tumour serial sections was developed. This bridges the gap between the actual topology of vascular distributions in tumours and the format of current formulations.

ACKNOWLEDGEMENTS

I wish to thank McMaster University and the Hamilton Regional Cancer Centre for giving me the opportunity to do graduate studies. Special thanks to Dr. Cheuk Kwok for the guidance, support, and willing assistance that he has offered me throughout this project. I would also like to thank the following individuals that have assisted me in my work: Sharon Lee, Jun Li, Ron Geisler, Debbie Browning, Dr. Andrew Hrymak, Dr. Larry Arsenault, Suzie Cindric and Athanassios Kassidas.

TABLE OF CONTENTS

ABSTRACT iii
ACKNOWLEDGEMENTS iv
TABLE OF CONTENTS v
LIST OF TABLES ix
LIST OF FIGURES x

PART I: INTRODUCTION 1

1. Overview of the Thesis 2

1.0 Literature Review 3

1.0.1 A List of Relevant Physiological Parameters 4

1.0.2 Studies on the Quantification of Macromolecule Uptake by Tumours 7

1.0.3 Studies on the Macromolecule Spatial and Temporal Distributions in Multicellular Spheroids and Vascularized Tumours 9

1.0.4 Pharmacokinetic Models 11

1.0.5 Studies on the Total Plasma Fluid Extravasation Rate and Vascular Permeability P 13

1.0.6 Other Physiological Parameters Relating to Macromolecule Transport in Tumour 17

1.0.7 Tumour Vasculature Morphometric Analyses and Surface Interpolation 19

1.1 Numerical Methods 21

1.1.0 Finite Differences 21

1.1.0.1 Tridiagonal Matrices 24

1.0.1.2 Block-Diagonal Matrices 25

1.1.1 Solution Methods 25

1.1.1.1 Gaussian Elimination 25

1.1.1.2 The Numerical Method of Lines (NUMOL) 26
1.1.2 B-Splines 30

PART II: THE ANIMAL EXPERIMENTS **32**

2. The Nude Mouse Model 33

2.0 The Experiments 33
2.0.1 Materials and Methods 33
2.0.1.1 The Iodination of IgG 33
2.0.1.2 The Animal Experiment Protocol 35
2.0.2 Calculations 36
2.0.3 Results 39
2.0.4 Limitations / Problems of the Experiment 42

PART III: MATHEMATICAL MODELLING OF MACROMOLECULE TRANSPORT IN TUMOURS **43**

3. A Mathematical Model for the Interstitial Plasma Pressure and Velocity Spatial Distributions in Tumours 44

3.0 Definition of the Interstitial Fluid Pressure Equation for a Uniformly Perfused Tumour 44
3.0.1 The Analytical and Numerical Solution for Interstitial Pressure for a Well Perfused Tumour 47
3.0.2 Conservation of fluid 48
3.1 Definition of the Interstitial Fluid Pressure Equation for a Tumour with a Variable Size Necrotic Core, or Radially Variable Surface Area for Transcapillary Exchange per Unit Volume 52
3.1.1 The Analytical and Numerical Solutions for Interstitial Pressure for a Tumour with a Variable Size Necrotic Core, or Radially Variable S/V 53
3.2 The Interstitial Fluid Velocity Distribution 58
3.3 Discussion 60

4. A Mathematical Model for the Spatial and Temporal Macromolecule Distributions in Tumours 64

4.0 A Solute Transport Model for Non-Binding Macromolecules in a Spherical Well Perfused Tumour, or One Having a Necrotic Core 64

4.0.1 The Numerical Solution of the Macromolecule Transcapillary Transport Equation for Non-Binding Macromolecule 67

4.1 A Solute Transport Model for Binding Macromolecules in the Presence of Metabolism for a Spherical Well Perfused Tumour, or one Having a Necrotic Core 76

4.1.1 The Numerical Solution of the Macromolecule Transcapillary Transport Equations for Binding Macromolecule in the Presence of Metabolism 77

4.2 Other Results and Sensitivity Analysis 81

4.2.1 The Effect of Binding Affinity and Metabolism 90

4.2.2 The Effect of S/V and the Tumour Radius 92

4.2.3 The Effect of Diffusive Permeability (P) and Molecular Weight . . . 97

4.3 Limitations of the model 103

PART IV: A COMPUTATIONAL TOOL DERIVING TUMOUR VASCULAR DISTRIBUTION PARAMETERS 112

5. A Proposed Method for the Determination of the Radial Variation of Vascular Volume and Vascular Surface Area per Unit Volume of Tumour . 113

5.0 An Algorithm for 'Peeling' an Arbitrary Convex Object 113

5.1 A Proposed Method for the Determination of Vascular Volume and Surface Area per Unit Volume of Tumour 120

5.2 Limitations of the Method 122

PART V: SUMMARY AND RECOMMENDATIONS FOR FUTURE WORK 125

6. Conclusion 126

6.0 Summary of Conclusions 126
A. The Nude Mouse Model 126
B. The Interstitial Fluid Pressure and Velocity Distributions in Tumours . 126
C. The Spatial and Temporal Macromolecule Distributions in Tumours . .127
D. A Method for Quantifying the Radial Variation of Vascular Density and S/V of Arbitrary Shape Convex Tumours 130
6.1 Recommendations for Future Work 131

APPENDIX I PROGRAMS INFORMATION 138
REFERENCES **139**

LIST OF TABLES

Table 2.1: Vascular Volume and Vascular Permeability of SKOV3ip1 Human Tumour Xenografts in Nude Mice 39

LIST OF FIGURES

Figure 2.1: The total vascular volume (ml) vs tumour weight (g) 41

Figure 2.2: The total plasma fluid extravasation rate (ml/h) vs tumour weight (g) 41

Figure 3.1: The extravasated interstitial fluid pressure and velocity radial profiles for a 1cm radius tumour 49

Figure 3.2: The radial variation of the transcapillary fluid source terms (eqs. 3.3 - 3.4). Negative values indicate that the capillaries are forced to become sinks due to the fluid overflow at the edge of the tumour 51

Figure 3.3: The interstitial fluid pressure radial profile for a tumour with 50%, 75%, 95%, and 99% of its 1cm radius being necrotic 55

Figure 3.4: The interstitial fluid pressure radial profile for an S(r)/V varying as a sigmoid (eq. 3.19, D=0, A=1, B=0.5, C=10) 56

Figure 3.5: The interstitial fluid pressure radial profile for an S(r)/V decreasing exponentially from the tumour surface (eq. 3.20, A=1, B=5) 57

Figure 3.6: The interstitial fluid velocity radial profiles corresponding to the pressure profiles of fig. 3.3 59

Figure 3.7: The average interstitial pressure in a tumour as a function of its radius 61

Figure 3.8: The average interstitial fluid velocity in a tumour as a function of its radius 63

Figure 4.1: The radial variation in a R=1cm tumour of the dimensionless free IgG concentration at 1h (light-filled squares), 8h (dark-filled squares), 24h (asterisks), 72h (empty squares), 9d (light-filled triangles) for constant perfusion 70

Figure 4.2: The radial variation in a R=1cm tumour of the dimensionless free Fab fragment concentration at 1h (light-filled squares), 8h

(dark-filled squares), 24h (asterisks), 72h (empty squares), 9d (light-filled triangles) for constant perfusion 71

Figure 4.3: The radial variation in a R=1cm tumour of the dimensionless free IgG concentration at 1h (light-filled squares), 8h (dark-filled squares), 24h (asterisks), 72h (empty squares), 9d (light-filled triangles) after a single bolus i.v. injection at t=0 (see eq. 4.4) 72

Figure 4.4: The radial variation in a R=1cm tumour of the dimensionless free Fab fragment concentration at 1h (light-filled squares), 8h (dark-filled squares), 24h (asterisks), 72h (empty squares), 9d (light-filled triangles) after a single bolus i.v. injection at t=0 (see eq. 4.4) 73

Figure 4.5: The radial variation of the dimensionless free IgG concentration after a 24hr constant perfusion in a R=1cm tumour having 50% (solid line), 75% (dotted line), 95% (centered line), and 100% (dashed line) of its radius being necrotic 74

Figure 4.6: The radial variation of the dimensionless free Fab fragment concentration after a 24hr constant perfusion in a R=1cm tumour having 50% (solid line), 75% (dotted line), 95% (centered line), and 100% (dashed line) of its radius being necrotic 75

Figure 4.7: The radial variation in a R=1cm tumour of the dimensionless bound IgG concentration at 1h (light-filled squares), 8h (dark-filled squares), 24h (asterisks), 72h (empty squares), 9d (light-filled triangles) for constant perfusion 82

Figure 4.8: The radial variation in a R=1cm tumour of the dimensionless bound Fab fragment concentration at 1h (light-filled squares), 8h (dark-filled squares), 24h (asterisks), 72h (empty squares), 9d (light-filled triangles) for constant perfusion 83

Figure 4.9: The radial variation in a R=1cm tumour of the dimensionless bound Fab fragment concentration at 1h (light-filled squares), 8h (dark-filled squares), 24h (asterisks), 72h (empty squares), 9d

(light-filled triangles) for a single bolus i.v. injection at t=0 (see eq. 4.4) 84

Figure 4.10: The radial variation in a R=1cm tumour of the dimensionless bound Fab fragment concentration at 1h (light-filled squares), 8h (dark-filled squares), 24h (asterisks), 72h (empty squares), 9d (light-filled triangles) for a single bolus i.v. injection at t=0 (see eq. 4.4) 85

Figure 4.11: The radial variation of the dimensionless bound IgG concentration after a 24hr constant perfusion in a R=1cm tumour having 50% (solid line), 75% (dotted line), 95% (centered line), and 100% (dashed line) of its radius being necrotic 86

Figure 4.12: The radial variation of the dimensionless bound Fab fragment concentration after a 24hr constant perfusion in a R=1cm tumour having 50% (solid line), 75% (dotted line), 95% (centered line), and 100% (dashed line) of its radius being necrotic 87

Figure 4.13: The radial variation in a R=1cm tumour of the dimensionless total IgG concentration at 1h (light-filled squares), 8h (dark-filled squares), 24h (asterisks), 72h (empty squares), 9d (light-filled triangles) for constant perfusion 88

Figure 4.14: The radial variation of the dimensionless total (free + bound) IgG concentration after a 24hr constant perfusion in a R=1cm tumour having 50% (solid line), 75% (dotted line), 95% (centered line), and 100% (dashed line) of its radius being necrotic 89

Figure 4.15: The total IgG radial profiles after a 72hr constant perfusion with the binding affinity B_a having values of 10^{-1} (solid line), 10^0 (dotted line), 10^1 (centered line), and 10^3 (dashed line) times the baseline value 93

Figure 4.16: The total IgG radial profiles for constant perfusion and an exponentially decreasing S/V (eq. 3.20, A=1, B=5) at 1h (light-filled squares), 8h (dark-filled squares), 24h (asterisks), 72h

(empty squares), 9d (light-filled triangles), all else being baseline 94

Figure 4.17: The average over a whole tumour of R=1cm of the total bound IgG (solid line), $F(ab')_2$ (dotted line), and Fab (dashed line) concentrations as a function of time after a single bolus i.v. injection at t=0 96

Figure 4.18: The total IgG (solid line), $F(ab')_2$ (dotted line), and Fab (dashed line) concentrations in a R=1cm tumour for a 72hr constant perfusion in the presence of metabolism 98

Figure 4.19: The bound macromolecule concentration at the centre of the tumour expressed as a fraction of the total bound concentration over the whole tumour, as a function of time for IgG (asterisks), $F(ab')_2$ (dark-filled squares), and Fab (light-filled squares). All vascular permeabilities P_{eff} are 10 times their baseline values 101

Figure 4.20: The variation of the ISN (eq. 4.15) for bound IgG (light-filled squares), $F(ab')_2$ (dark-filled squares), and Fab (asterisks) with time in a R=1cm tumour. The plasma clearence is bi-exponential (eq. 4.4) and all parameters are baseline 102

Figure 4.21: The experimentally determined (dotted line) total IgG uptake in human ovarian OVCAR tumours (Kwok *et al.* 1996) and the theoretically predicted one (eqs. 4.15 & 4.16). The binding affinity B_a, and the vascular permeability P_{eff} were assumed to have 32 and 270 times their baselines values respectively, for an R=0.375cm tumour 108

Figure 4.22: The experimentally determined (dotted line) Fab' average concentration in human ovarian OVCAR tumours (Kwok *et al.* 1996) and the theoretically predicted one (eqs. 4.15 & 4.16). The association rate constant k_f, and the vascular permeability P_{eff} were assumed to have 2.5 and 12 times their baselines values respectively, for an R=0.375cm tumour 110

Figure 4.23: The theoretically predicted average over a R=1cm tumour of the total bound IgG (light-filled squares), Fab'$_2$ (dark-filled squares), and Fab (asterisks) using the P_{eff}'s proposed by Fujimori *et al.* 1989 111

Figure 5.1: The new point (r_2,θ,ϕ) is outside the 'source' surface that created it, and is an invalid inner surface data point 116

Figure 5.2: The new point lies inside the 'source' surface. However, if one uses the new point (r_2,θ,ϕ) as the centre of a sphere of radius $|\Delta\mathbf{r}|$ the latter surface intersects the former. This means that there is at least one radial distance $\mathbf{r}_{ij}$ calculated on the regular mesh on the sphere that is larger than the corresponding 'source' surface radial distance for the same θ, ϕ ($r_1 < r_{ij}$). Hence, (r_2,θ,ϕ) is an invalid inner surface point as its minimum distance from the 'source' surface is less than $|\Delta\mathbf{r}|$ 118

Figure 5.3: The result of 'peeling' twice an ellipsoid A with principal axes (1,1,2) in steps of $|\Delta\mathbf{r}|$= 0.25, are ellipsoids B: (0.75,0.75,1.75), and C: (0.5,0.5,1.5) 119

PART I: INTRODUCTION

1. Overview of the Thesis

The purpose of this project was to study the transport of plasma fluid and macromolecules in vascularized tumours. The macromolecules of interest are IgG and its $F(ab')_2$, and Fab fragments. Using molecular biology techniques, the fragments can be produced with high intrinsic binding affinities for selected tumour antigenic sites. If conjugated to a radionuclide having the appropriate emission characteristics, they can be used for medical imaging and radioimmunotherapy applications. A previously proposed model (Baxter & Jain, 1989,1990,1991a) of fluid and macromolecule transport in tumours was expanded to include the spatial variation of surface area of blood vessels for transcapillary exchange per unit volume of tumour tissue (S/V). This allows one to investigate the relative importance of the physiological parameters involved in maximizing the homogeneity of delivered macromolecules of different macromolecular sizes. This introductory chapter outlines the experimental, mathematical, and computational efforts made to achieve this goal. A comprehensive summary of the work done by other researchers in, and around this area is given here. This will help illustrate the position of this project in the overall field picture clearly.

A series of experiments were performed to quantify the total vascular volume and plasma fluid extravasation rate of the SKOV3ip1 human ovarian tumours as a function of tumour size (Song & Levitt 1970) in nude mice. The experimental methods used and a discussion of the results are presented in chapter 2.

The steady-state spatial variation of the interstitial fluid pressure and velocity in a tumour are examined in chapter 3. A fluid transport equation proposed by Baxter & Jain (1989) was revisited. The correct analytical solutions, which are different from the reported ones were evaluated. The sensitivity of results to variation of physiological parameters and the radial profile of S/V were examined. The predicted total fluid extravasation rate was found close to the measured one as presented in chapter 2.

Once the attributes of interstitial fluid flow were determined, the spatial and temporal macromolecule distributions in tumours could be predicted. The equations proposed by the above authors (1989,1990,1991) for both binding and non-binding macromolecules were solved by numerical methods in chapter 4. A number of

shortcomings of the proposed formulations were found and are discussed. The sensitivity of the distributions to a variety of transcapillary transport parameters including a radially variable S/V was investigated. The most important ones in increasing the homogeneity of distributed macromolecule were identified. A set of realistic physiological parameters predicting a total macromolecule uptake matching available experimental data was attempted.

In chapter 5 an experimental method for the determination of the spatial distribution of S/V in real tumours is proposed. No such data is available in the literature. The relevant computational tools needed to deduce this distribution in a form compatible with the formulation of the macromolecule transport equations were developed and tested.

In the concluding chapter a summary of the results and the limitations of the methods used is presented. Directions for further developments are pointed out.

1.0 Literature Review

A large volume of work relating to the mechanisms of transcapillary exchange has been published in the last fifty years. The formulation of the basic equations used by all authors has changed little since they were first proposed. Papers by Pappenheimer et al. (1951), or Kedem & Katchalsky (1958) are still being quoted today. However, the predictions of these formulations are only of qualitative value. The details of transcapillary exchange of large m.w. molecules between plasma fluid and tissue are still largely unknown. This is mainly due to the vast number of factors affecting the process and the obvious difficulty of obtaining them experimentally in vivo, in a consistent system. The fact that this process occurs mainly at the capillary level requires observation and possible manipulation of experimental conditions with micron resolution, which is an additional difficulty.

Curry (1984, pp.309-374) provides a comprehensive review of the mechanics and thermodynamics of transcapillary exchange. A detailed study of the membrane transport equations as proposed by Kedem & Katchalsky are included in his analysis. These equations provide the basis for the macromolecule source term used in the equations proposed by Baxter & Jain (1989), and were studied in this project. The similarity

between the sieving of macromolecules by artificial porous membranes and the extravasation of plasma proteins through the capillary wall led to the pore theory of capillary permeability (Pappemheimer *et al.* 1951). The fenestrations between endothelial cells are described as cylindrical pores having an effective radius. An exhaustive analysis of different formulations relating to pore theory is presented in Curry's review paper. The hypothesis that a three-dimensional network of fibrous molecules in the endothelial cells may be the principal determinant of the selectivity of the capillary wall (Michel 1978) is examined in the above paper. The contribution of charged solutes to osmotic pressure and capillary wall selectivity, as well as vesicle and lipophilic solute transport are also studied.

Jain (1987a,b) gave reviews of the transport of molecules across tumour vasculature. Tumour vessels have wide interendothelial junctions , large number of fenestrae, and a discontinuous or absent basement membrane. The objective of immunotherapy is to exploit the resulting higher permeability of these vessels to increase the uniformity of perfusion with an immunoreactive macromolecule like IgG, or its fragments $F(ab')_2$, and Fab. The parameters characterizing the transvascular transport of fluid and solute molecules were emphasized. The methods of measurement and modulating these key physiological parameters were described. The implications for tumour growth, detection, and treatment were discussed.

1.0.1 A List of Relevant Physiological Parameters

In order for a mathematical model of tumour fluid and macromolecule transport to give quantitative predictions, it is imperative that the values of the relevant physiological parameters be specified on input. The purpose of this section is to define these parameters, as they will be appearing repeatedly in this work. It is however useful to describe first the gross structure of the macromolecules of interest in immunotherapy.

IgG : A protein molecule of globular shape in its natural form (immunoglobulin) but Y-shaped when unfolded of m.w. 150kD. The 'arms' of the Y each consist of a heavy and a light chain connected by a disulfide bond. The free tips of the 'arms' manifest the

greatest variability in aminoacid sequence giving them a wide range of immuno-reactivities. The leg of the Y is the structurally constant (Fc) molecule portion. It consists of two chains connected by two disulfide bonds situated near the 'arm-leg' junction.

$F(ab')_2$: If the Fc portion of the IgG is cleaved by restriction enzymes near, but below the two disulfide bonds, then the 'arms' and a short two-chain 'leg' remain. In the resulting IgG fragment (F) the subscript (2) signifies that there are two 'arms' and the superscript (') indicates that a short 'leg' is attached to the 'arms'.

Fab' : If the disulfide bonds of the $F(ab')_2$ are chemically cleaved, two Fab' fragments each with an 'arm' and a short single-chain 'leg' are produced.

Fab : If the short 'leg' of an Fab' is cleaved leaving only a heavy-light chain pair, the accent is dropped from the notation. Fab' and Fab were assumed to have identical transport parameters in this work as their small m.w. difference (~5kD) does not have a significant impact on the value of these parameters.

mAb : Monoclonal Antibody. These macromolecules are IgG's all originating from the same 'source' cell and hence have identical structural and chemical properties.

The physiological parameters defined below apply to both normal and tumour tissue.

B_i = Interstitial concentration for bound macromolecule (M).

B_{max} = Concentration of bound macromolecule at saturation of binding sites (M).

C = Interstitial free macromolecule concentration (M).

C_p = Macromolecule plasma concentration (M).

D = Diffusion coefficient (cm^2/sec). It quantifies the velocity of spread of macromolecule in the interstitium for a given macromolecule concentration gradient, in the absence of convection. It is a macroscopic quantity.

J_V/V = Volume flow rate out of the vasculature per unit volume of tissue (sec^{-1}). If integrated over the tumour volume it will give the total fluid extravasation rate.

J_L/V = Volume flow rate out of the lymphatics per unit volume of tissue (sec^{-1})

J_S/V = Solute mass out of the vasculature per unit time, per unit volume of tumour tissue ($M\ sec^{-1}$).

K = Hydraulic conductivity of the interstitium ($cm^2/mmHg/sec$). It quantifies velocity

for a given pressure gradient.

k_f = Association rate constant (M^{-1} sec^{-1}). It quantifies the rate of macromolecule binding to antigen.

k_r = Macromolecule-antigen dissociation rate constant (sec^{-1}).

B_a = The macromolecule binding affinity defined as k_f/k_r.

k_e = Metabolism rate constant (sec^{-1}).

L_p = Hydraulic conductivity of the microvascular wall (cm/mmHg/sec). It is an analog of the electric conductivity and quantifies the fluid transport rate through a semipermeable membrane for a given pressure difference across it. The membrane refers to vessel walls.

P = Effective vascular diffusive permeability coefficient (cm/sec). It is the velocity with which a solute will cross a semipermeable membrane for a given concentration difference across the latter. The diffusive and convective of permeability have been lumped into a single parameter.

p_V = Vascular hydrostatic pressure (mmHg).

p_L = Hydrostatic pressure in the lymphatics (mmHg).

π_V = Osmotic pressure of the plasma proteins (mmHg). It is the pressure exerted on surrounding solvent molecules by proteins of different m.w.'s dissolved in plasma fluid in virtue of their motion. It may be measured by exerting an equal and opposite hydraulic pressure on the solvent to prevent osmosis.

π_i = Osmotic pressure of the interstitial fluid (mmHg).

r_F = Retardation factor. For a stationary observer the effective solute velocity should be the one as seen in the reference frame of the solvent, multiplied by r_F, the ratio of solute to fluid velocities.

S/V = Vessel surface area for transcapillary exchange per unit volume of tissue (cm^{-1}).

σ_T = Average osmotic reflection coefficient for plasma proteins (no units). The geometric structure of proteins in solution and the finite size of the pores in a semi-permeable membrane, result in only a fraction of the incident molecules making it through the membrane. This determines the relative magnitude of the equilibrium osmotic and hydraulic pressures on either side of the membrane.

σ = Macromolecule osmotic reflection coefficient.

t = Time (sec).

u_i = Interstitial fluid velocity (cm/sec), +ve in the radially outward direction.

π_V, π_i, and σ_T are average quantities in order to simplify the effect of the multitude of proteins floating in plasma fluid contributing to their values. It should also be noted that P is a theoretical parameter that has the units of velocity (cm/sec) and should not be confused with total fluid extravasation rate per gram of tissue (ml/g/h) that experimentalists refer to as vascular permeability.

1.0.2 Studies on the Quantification of Macromolecule Uptake by Tumours.

The promise of monoclonal anti-tumour antibodies for immunodetection and therapy has attracted the attention of a large number of researchers since the early 1980's. The target in immunodetection is to achieve highly specific uptake with a high tumour to blood ratio in order to increase the signal to noise ratio, and rapid clearance from normal tissues to reduce the radiation exposure of the patient. For therapy, the highest possible non-toxic mAb doses and uniformity of perfusion are desired. The number of publications in the area is very large and only a few are mentioned here to outline some of the standard methods employed in the area.

Wahl *et al.* (1983) reported the superiority of the $F(ab')_2$ fragment in radioscintigraphy. Its smaller molecular weight than the intact IgG produced higher tumour to blood activity ratios. The higher uptake of the Fab fragment by the liver and kidney made it a less favourable option in the particular application. Buraggi *et al.* (1985) used ^{131}I-labelled IgG and $F(ab')_2$ specific to a particular melanoma antigen, to study their localization in patients carrying such tumours. The superiority of $F(ab')_2$ to whole IgG for radioscintigraphy because of background reduction was reported. Hagan *et al.* (1985) reported that the specific mAb uptake per g of tumours appeared to be inversely proportional to tumour size. No such correlation for non-specific mAb uptake was found. Williams *et al.* (1988) pooled the data of Hagan *et al.* (1985) with those obtained in a similar series of experiments using the same antibody-antigen model and fitted the results

for specific and non-specific mAb's to an expression of the form $u = Bm^{A}$, where u is the tumour uptake, m its mass, and A and B are constants. Williams *et al.* found a wide scatter of data reflecting the very large individual differences in tumour accumulation and also a mismatch of the two sets of data. Sharkey *et al.* (1990) compared the biodistribution of the NP-4 antibody and its fragments labelled with ^{111}In, ^{88}Y, and ^{131}I. The former two nuclides were linked to the mAb's with appropriate organic chelates and the latter chemically. Tumour to non-tumour ratios for a large number of organs of mice bearing human tumour xenografts were obtained and the radiation doses in those organs were estimated. They concluded that the ^{131}I-labelled IgG and fragments gave a greater flexibility to permit tumoricidal doses without excessive toxicity to normal tissues. Shockley *et al.* (1992) studied the effect of the immunological properties of anti-melanoma mAb's and tumour antigen expression levels in two tumours on the uptake of the mAb. The latter were found to differ in their antigen expression levels which were different in vivo than in vitro. Plasma fluid extravasation rates using ^{131}I-labelled mAb's were quantified and the importance of vascular volume and permeability in tumour perfusion were emphasized. Fand *et al.* (1992) compared the effectiveness of two antitumour IgG's and their fragments in achieving tumour localization by obtaining macroautoradiographic images over the whole body of a mouse. Quantitative densitometry indicated higher tumour:blood ratios and rapid plasma clearance for the IgG fragments as reported by other authors. Kairemo *et al.* (1994) used a beta camera of their own design to image the spatial distribution of ^{90}Y-labelled antifibrin mAb's in serial frozen sections of a tumour. This allowed them to do a 3D reconstruction of the radioactivity distribution and estimate the total absorbed dose over the whole tumour. Although tumour stroma contains a lot of fibrin, they did not investigate the effect that a radiolabelled antifibrin mAb would have on other organs of a mouse that may have a high fibrin content e.g. the bones. Using the same tumour model that Williams *et al.* (1988) and Fand *et al.* (1992) used, Vogel *et al.* (1993) compared the tumour uptake of IgG and its $F(ab')_2$ fragment and arrived at results similar to the ones reported by the former authors. Buist *et al.* (1995) quantified the uptake of radiolabelled mAb's in ovarian carcinoma patients. Tumour uptake and tumour to normal tissue ratios were studied in relation to

histopathological classification, prior treatment, site of tumour, time interval post-injection, antigen expression, volume percentage of malignant epithelium, and the size of the tumour. The antibody uptake was positively correlated to antigen expression and inversely correlated with the time interval between injection and surgery. No correlation was observed with any of the other factors studied, not even tumour size in contrast with the animal data by Williams *et al.* (1988). Kobayashi *et al.* (1994) studied the tumour uptake of ^{131}I-labelled biotinylated mAb followed by infusion of avidin as a 'chase' molecule to reduce the accumulation of the former in other organs. Following the injection of avidin, the radioactivity was promptly cleared from the blood and deposited in the liver and spleen. There, radioiodine was rapidly detached from the mAb and excreted in the urine. Hence, the tumour to blood ratio as well as the mAb concentration in healthy organs ware reduced. The same group (Kobayashi *et al.*, 1995) compared the chase effects of avidin, streptavidin, neutravidin, and avidin-ferritin following the administration of a radioiodine-labelled biotinylated monoclonal antibody. Avidin was the most effective chasing agent of the latter among the four avidin derivatives tested.

1.0.3 Studies on the Macromolecule Spatial and Temporal Distributions in Multicellular Spheroids and Vascularized Tumours.

The methods determining the total macromolecule uptake in tumour yield no information about its spatial and temporal distributions within the tumour volume, or around individual vessels. Hence, it is instructive to build mathematical models predicting the latter in order to guide experiment in optimizing macromolecule delivery. The physical mechanisms of macromolecule transport into the tumour interstitium depend on whether the tumour is vascularized, or simply is a multicellular aggregation. The resulting two categories of modelling are reviewed here separately.

Early tumours are avascular multicellular nodules obtaining their nutrient supply via passive diffusion from surrounding healthy tissue, into the interstitial spaces between cancer cells. Hence, the most important parameters determining the spatial-temporal macromolecule distributions in tumour nodules are the macromolecules' diffusion

coefficient D and their binding affinity B_a. D, and the reversible binding (k_f,k_r) and metabolism (k_e) rate constants for human melanoma spheroids, grown and perfused in culture, have been determined by fitting the measured mAb concentration profiles to the relevant mathematical models developed (McFadden & Kwok 1988, Kwok *et al.* 1995). The optimal combination of antitumour mAb quantity, specific activity, and treatment time are also an issue of interest for optimizing radioimmunotherapy of such spheroids in vivo (Kwok *et al.* 1989). Macromolecule transport in vascularized tumours is governed by the complicated mechanics and thermodynamics of transcapillary exchange. To overcome the insurmountable difficulty of dealing with realistic tumour and vascular tree shapes, Baxter & Jain (1988,1989,1990,1991a) proposed a 'distributed source' model. This means that only an average over the viable tumour tissue, but not the exact form of the vascular distribution have to be specified. The work by Baxter & Jain was the basis for the mathematical modelling done in this project.

The steady state interstitial pressure and velocity distributions in tumour are required to be determined first, before one proceeds to macromolecule distribution calculations. This is because the pressure and velocity distributions will determine the areas where convective transport can occur. The key result of mathematical modelling of plasma fluid transport in tumours is that the higher permeability of tumour vessels relative to those in surrounding normal tissue, and the lack of lymphatics in tumour, result in an elevated interstitial pressure in the tumour (Baxter & Jain 1989). The latter reduces the driving force for extravasation of fluid and macromolecules and leads to an experimentally verifiable, radially outward fluid convective transport which washes the macromolecule out of the tumour. The presence of a necrotic core does not have a significant effect on the pressure build-up, but the presence of lymphatics helps a lot in its reduction (Baxter & Jain 1990). Reversible binding and metabolism of bound macromolecules in vascularized tumours have similar effects on the macromolecule distribution (Baxter & Jain 1991a) to the ones found in multicellular spheroids. Higher binding affinity and antigen density increase the macromolecule uptake, but decrease the homogeneity of its distribution. The new result was that increasing the vascular permeability P of tumour vessels increased the macromolecule uptake. Also, all

macromolecule types (even non-binding ones) did not travel far from the point where they extravasated, leading to poor perfusion of areas far from vessels.

In order to verify whether the 'distributed source' models are a reasonable approximation to the actual macromolecule distributions, it is instructive to model fluid and macromolecule transport across individual capillaries (Baxter & Jain 1991b). Also, the outgoing fluid from a capillary may be opposed by the outgoing fluid flow from a neighbouring one. Intercapillary interaction may substantially reduce the amount of fluid filtered from a single capillary (Fleischman *et al.* 1986). There is currently no model in the literature linking the microscopic scale of pericapillary macromolecule distributions and intercapillary interactions to the macroscopic scale of averaged out 'solute source' models.

1.0.4 Pharmacokinetic Models

A lot of attention has been paid in the last fifteen years in the global pharmacokinetics of IgG and its $F(ab')_2$ and Fab fragments in humans and experimental animals. A commonly used technique for deriving pharmacokinetics data in animals involves chemically conjugating the above macromolecules to an isotope for detection, administering the labelled macromolecules in mice, and measuring the uptake of the labelled macromolecules in each vital organ and blood of the animals at selected time points. The data are then fitted into a compartmental model. The structure of the model and the choice of fitting parameters is largely dependent on the design of the experiment. A common objective of the pharmacokinetics study is to maximize the tumour uptake and minimize the uptake of the macromolecules in critical organs, such as liver, kidney, lung etc. in radioimmunotherapy. Such considerations also apply to radiolabelled tumour-specific protein toxins. 'Hybrid' models have also been developed, linking macromolecule global pharmacokinetics with their detailed spatial-temporal distributions in the bulk of the tumour, as well as around individual capillaries. Compartmental and 'hybrid' pharmacokinetic models are reviewed separately in this section.

Important parameters in assessing the cumulative exposure of different tissues in experimental animals are the macromolecule biodistribution, catabolism and excretion

(Covell *et al.* 1986), ligand molecular size and binding affinity (Thomas *et al.* 1989,1991), and capillary permeability (Sung *et al.* 1990). A two-pore formalism for transcapillary exchange fits experimental data better than a single pore one (Baxter *et al.* 1994) without having to use as fitting parameters unrealistic physiological values. Pharmacokinetic models can serve to scale up data from experimental animals to humans (Baxter *et al.* 1995). However, differences in organ volumes, blood flow rates, vascular permeabilities, and anatomical connection of different organs need to be taken into account.

Compartmental models have also been built for two-step approaches in delivering macromolecules to tumours using bifunctional antibodies (BFA), or enzyme-conjugated antibodies (ECA). The principle of the approaches is that BFA (or ECA) is injected into a patient, permitted to bind to antigenic sites in the tumour, and then cleared from normal tissues either by being excreted naturally, or by the use of 'chase' macromolecules which increase the catabolism and excretion rate of the conjugate from the body. After an appropriate time interval, a radionuclide attached to a low molecular weight hapten (or a prodrug) is injected. The advantage of the latter is their rapid movement in the tumour and clearance from the body. The problems tackled relate to the optimal timing for injection and the injected dose of the second drug, in order to find a compromise between the desired tumour concentration and tumour:blood concentration ratio (Yuan *et al.* 1991). The intermediate 'chase' step produces higher tumour:blood ratios and reduced normal organ uptakes (Goodwin *et al.* 1994). The higher concentrations of mAb that one can afford to inject without toxicity problems using this method has considerable promise for improved radioimmunotherapy.

'Hybrid' models incorporate both macroscopic aspects of antibody distribution in the whole body, as well as microscopic ones of the spatial-temporal distributions in tumour. The models splice together information on global pharmacokinetics, transport across the capillary wall, diffusive penetration through the tumour interstitial spaces, and antigen-antibody interaction. In the case of tumour spheroids, transcapillary transport refers to healthy tissue vessels in the vicinity of the nodule. High mAb binding affinity decreases the homogeneity of its distribution leading to an experimentally verifiable 'binding site barrier' (Fujimori 1990, Fujimori *et al.* 1990, Juweid *et al.* 1992). Lymphatic

outflow of surrounding normal tissue and an increased antigen density of tumour cells increase the mAb distribution heterogeneity in a nodule (Van Osdol *et al.* 1991). Two-step 'hybrid' models have also been investigated in optimizing radioimmunotherapy of avascular tumour nodules in vivo. A popular choice is the biotin-streptavidin pair. Biotin haptens against streptavidin-conjugated mAb's (Van Osdol *et al.* 1993) and streptavidin haptens against biotinylated mAb's (Sung *et al.* 1974) have been investigated. A common observation is that the high binding affinity of the pair reduces the homogeneity of the radiolabelled hapten distribution in the nodule.

In the case of vascularized tumours, assuming purely diffusive transcapillary transport, 'hybrid' models show that there is considerable interaction between the binding kinetics, initial drug doses, and antigen density with optimal parameter ranges depending on whether the goal is treatment, or detection (Baxter *et al.* 1992). No hybrid model currently exists linking a 'distributed source' model including both diffusive and convective macromolecule transport in tumour, with global pharmacokinetics.

1.0.5 Studies on the Total Plasma Fluid Extravasation Rate and Vascular Permeability P

This section describes the variety of methods used to quantify vascular permeability and the models developed to describe its physical mechanism. Data obtained in physiological experiments have interpreted the transport of protein molecules across capillaries assuming diffusion and convection through small ($r< 12nm$) and large ($r= 20$-$50nm$) cylindrical 'pores'. They represent interendothelial gaps mostly, although they could also represent effective pinocytic pathways across the endothelium. Factors like the relative size of pore and macromolecule, the possible fibrous matrix in the capillary basal lamina, the macromolecule concentration gradients, and the differences in hydraulic and osmotic pressures across the capillary wall, will determine the transport characteristics of the particular macromolecule. Transendothelial transport could also occur by way of vesicles forming, engulfing the macromolecule and releasing it on the other side of the capillary wall. The size of the molecule and its binding affinity to some component of the

endothelial surface may influence the rate and pathways of its transport (Milici *et al.* 1987). However, the hydrodynamic laws relating to the 'pore' description will not be as important if pinocytosis is the dominant form of transport. Hence, it is crucial to determine the relative importance of interendothelial versus transendothelial transport in different tissues. For tumours, the rapid angiogenesis leads to capillaries with large fenestrations and a possible absence of basement membrane making a pore model the favourable mode of transport (Jain 1987). However, no conclusive evidence is available as yet.

Early work on the mechanics and thermodynamics of transcapillary exchange has set the basis for the pore theory of capillary permeability used today by most researchers to interpret experimental data. The basic principle is that the net rate of fluid movement across the capillary wall is proportional to the difference between hydrostatic and osmotic forces (Landis 1927). The 'vascular permeability' is usually quantified experimentally as the total plasma fluid extravasation rate per gram of tissue. The very first, and currently outdated, method of deducing fluid filtration rates in vivo relied on controlling the arterial and venous pressures in an experimental animal's limb and measuring the resulting changes in its weight due to oedema (Pappenheimer *et al.* 1951). The microscopic properties of capillaries could only be indirectly inferred from the macroscopic data. Their estimated pore sizes were about a factor of 10 lower than what they are known to be today for fenestrated capillaries. They also claimed that diffusion is dominant over convection in the transport of large macromolecules across capillaries, contrary to current beliefs. In the early second half of this century mathematical methods of irreversible thermodynamics were applied to combine the then independent volume and solute flow equations into a unified formulation in terms of parameters that can be verified experimentally (Kedem & Katchalsky 1958, Patlak *et al.* 1963). The expressions developed by Patlak *et al.* (1963) were the ones used by Baxter & Jain (1989), and in this project to describe the distributed source term representing transcapillary transport across the tumour vasculature. Historically, the most recent substantial step towards progress in understanding transcapillary transport came by Rippe & Haraldsson (1987) who developed a two-pore theory to describe the fluid and solute fluxes across small and large pores.

Comparison with animal data gave estimates of relevant capillary transport parameters. They predicted that 75-90% of the transvascular passage of albumin was due to convection through large pores, the remaining portion being mainly due to diffusion across small pores, and that for larger molecules the transport would be almost exclusively convective. The proposed model also explained the apparent variations for different net filtration rates in the experimentally observed permeability-surface area product (PS) and the reflection coefficient (σ) interpreted by a single pore model, as well as the overestimation of P.

An established method of measuring macroscopic transport constants is the use of fluorescent dye-tagged macromolecules in combination with intravital microscopy. The area of interest is confined into a transparent window attached to a living animal, and the view through the microscope is recorded by a video-camera. The latter records the variation of fluorescence intensity as a function of space, effectively in two dimensions, and is then converted to an effective macromolecule concentration distribution. The results are then fitted to a relevant transcapillary transport equation and values for macroscopic transport parameters are estimated from the fit. The first to propose the method were Gerlowski & Jain (1986) who deduced interstitial diffusion and permeability coefficients, D and P respectively (see section 1.0.1), assuming purely diffusive transcapillary transport. This was in contradiction to later results from mathematical modelling of macromolecule transport in tumours (Baxter & Jain 1989) predicting that the dominant form of transport is convective. Hence, it is believed that the value of P in the intravital microscopy experiments (Gerlowski & Jain 1986) was overestimated, which is also supported by Fujimori *et al.* (1989). The intravital microscopy method has been used to estimate the P of vessels to albumin and mAb-liposome conjugates, vascular surface area, vascular volume, and the effect of the blood-brain barrier on tumour perfusion of intra-cranial tumours implanted as human tumour xenografts in nude mice (Yuan *et al.* 1993,1994a,1994b).

Another way of determining the total vascular volume and the total plasma fluid extravasation rate in tumours is based on the use of radiolabelled tracers. The principle of this method is that RBC's are labelled with one radioisotope and tracer molecules for

plasma with another having different emissions so that one can distinguish the two. Since RBC's stay in the blood circulation, they give a measure of the blood volume and hence the vascular volume. On the other hand, the tracer molecule extravasates and distributes fairly uniformly in the extravascular space with enough time post injection, giving a measure of the extravasated plasma fluid volume. Using this method, the total vascular volume and plasma fluid extravasation rate per gram of healthy and tumour tissue in tumour-bearing rats has been estimated (Song & Levitt 1970, Peterson *et al.* 1973). This method was used in this project for measuring the above physiological parameters for SKOV3ip1 human ovarian tumours grown in nude mice, as described in chapter 2. Changes in fluid filtration rates due to vasodilators such as histamine (Rippe *et al.* 1978) and free IL-2 (Ballmer-Webber *et al.* 1995) can be measured using this method. The capillary permeability-surface area product (PS) can be deduced if the method is combined with grated rarefaction of the capillary network by microsphere injection, and alterations in capillary permeability (Rippe *et al.* 1978). The effect of X-irradiation and radioimmunotherapy on tumour fluid filtration has also been quantified using this method (Song & Levitt 1970, Blumenthal *et al.* 1995). The latter authors complemented their work with immunohistochemical staining of tumour sections and found that radiolabelled antibodies in the perivascular spaces lead to a significant decline of vascular volume and a thickening of the basement membrane surrounding the endothelium. As a result of the decreased permeability, a 90% decrease in accretion of a second dose of a radiolabelled antibody was observed which did not necessarily bind in areas near viable tumour cells that had survived the first dose. This obviously is a severe limitation in the efficacy of radioantibody fractionated regimen therapy.

Measurements of permeability and related physiological parameters using functional computed tomography have been reported by a number of authors. The advantages of the method are that it is non-invasive, thus providing more than one experimental time point for the same tumour. It also offers a spatial distribution for the measured parameters rather than a lumped value over the whole tumour, though the resolution is far from adequate in imaging individual capillaries. 200ms temporal and 0.05μl spatial resolutions (Hamberg *et al.* 1994) were among the highest achieved with any presently available

imaging technique, yet inadequate to image individual capillaries. The method has been mostly used for quantitative measurement of cerebral vascular permeability of patients carrying intra-cranial tumours using X-ray CT and an iodinated contrast medium. The time-density curves of the pixel CT numbers were fitted to a theoretical model to provide values for aggregate physiological parameters such as inward and outward flux constants and intra- and extra-vascular plasma volumes (Terada *et al.* 1992, Bartolini *et al.* 1992), extravascular space and regional blood flow (Warnke *et al.* 1994). Functional maps were also created for each of these parameters.

1.0.6 Other Physiological Parameters Relating to Macromolecule Transport in Tumour.

The mathematical modelling of macromolecule distributions in tumour inevitably requires specifying the values for a number of transport parameters on input. These are listed in section 1.0.1. The accuracy of these parameters obtained from experiment and the depth in the knowledge of the mechanisms of transcapillary exchange will determine how close the modelling predictions are to reality. In this section, some conventional methods used to measure the required transport parameters are presented. It is obvious through the work of most investigators in this field that the same parameters may assume different values in vivo than in vitro. Other factors like the cancer line, the location of the tumour, or even differences among individual patients are also important.

Experimental data from a large number of investigators estimating effective macromolecule diffusion coefficients D_{eff} for different tissues in experimental animals and humans showed that D_{eff} is a function of the macromolecule's m.w. (Swabb *et al.* 1974). The principle of the method is to fit the spatial spread of a dye-tagged macromolecule in the tissue of interest to the solution of the diffusion equation to obtain a value for D_{eff}. In vivo measurements of D_{eff} in experimental animals can be implemented using the 'window' method (Gerlowski & Jain 1986, Clauss & Jain 1990, Kaufman & Jain 1991) which makes it easier locating macromolecules in tissue. The values of D_{eff} measured with the above methods are macroscopic effective values and should not be confused with the

diffusivity of individual macromolecules in the interstitium (El-Kareh *et al.* 1993).

The 'window' method can also be used to deduce the concentration of binding sites, the macromolecule equilibrium binding constants (Kaufman & Jain 1991), and the effect of bivalent versus monovalent interaction on the apparent antibody affinity (Kaufman & Jain 1992). An improved method for measuring intrinsic equilibrium constants for the reversible interactions in an antibody-hapten system was based on particle counting of uniform polystyrene spheres to which the hapten is coupled covalently. An optical pulse particle size analyzer quantitated with high precision the specific aggregation of spheres cross-linked by antibody which was then correlated to intrinsic equilibrium constants. The technique offers high resolution and low concentration measurements, but is time consuming because of the time required for the spheres to reach equilibrium (2-5 days).

The hydraulic conductivity of tissue K can be measured in vitro by monitoring the pressures on either side of a tissue slab and measuring the fluid flow through it (Swabb *et al.* 1974). The average value of the microvascular hydraulic conductivity L_p in a tissue can be deduced by quantifying the total fluid extravasation rate using radiolabelled tracers, as described in section 1.0.5, and simultaneously varying the capillary hydrostatic pressure (Rippe *et al.* 1978). Optimal values of L_p to achieve maximum filtration of fluid in different tumours have been theoretically predicted (El-Kareh & Secomb 1995) and a stronger dependence of fluid filtration on tumour size was found rather than on tumour shape.

Capillary pressure can be measured using the method proposed by Pappenheimer *et al.* (1951). Interstitial pressure can be measured by imbedding a needle pressure transducer in tissue (Brace & Guyton 1977). Capillary and interstitial osmotic pressures can be measured by connecting an osmometer to a catheter in arterial and lymphatic vessels respectively (Brace & Guyton 1977), or can be inferred from compartmental models of fluid exchange (Wiederhielm 1978). The osmotic reflection coefficients σ of a number of macromolecules with very different m.w.'s was measured by monitoring volume changes in the subcutaneous tissue of experimental animals when hydrophilic solutes were added to the perfusate (Ballard & Perl 1978). Reflection coefficients for

proteins can be theoretically estimated by calculating their equivalent Stoke's radii (Curry 1974, Covell *et al.* 1986).

1.0.7 Tumour Vasculature Morphometric Analyses and Surface Interpolation.

In addition to the total vascular volume and the average S/V for a tumour, it is important to know the spatial distribution of such vessel parameters within its volume. Since macromolecules do not travel far from the point where they extravasated, the inhomogeneity of the vascular distribution dictates the inhomogeneity in the macromolecule distribution. Hence, knowledge of the former is an important tool in predicting the macroscopic distribution of immunoconjugates in all vascularised tumours of a specific cancer line. The actual shape of the tumour also comes into play in calculating the inhomogeneity of the vascular distribution. Some computational tools that can be used to interpolate an arbitrary shape smooth tumour surface from a discrete input set of surface coordinate points are also presented in this section.

Hilmas & Gillette (1973) proposed a method to estimate the vascular volume, average vessel diameter, mean vessel length, vessel surface area per unit volume of tumour tissue, and necrotic tissue volume in solid tumours. They also studied the effects of X-ray irradiation on the above parameters. The most important changes were a decrease in vascular surface area, and an increase in colloidal carbon filling the tumour microvasculature, both decreasing tumour filtration. The method is based on random sampling of tumour slides and statistical analysis. Although the parameters calculated had good confidence intervals, the method does not provide any information about their spatial distribution within the tumour volume. Dvorak *et al.* (1988) identified and characterised blood vessel patterns in solid tumours that are leaky to circulating macromolecules. They used 70kD and 150kD FITC-labelled dextrans in combination with fluorescence microscopy, as well as light and electron microscopy. They found that the most leaky vessels were veins or venules lined by a continuous endothelium with most of its interendothelial cell junctions closed. Immature vessels that had not differentiated yet to arterioles or venules, at the normal tissue-tumour interface vessels and inside the tumour

did not leak these macromolecule tracers significantly. Henri & Peters (1996a) presented a fully automated algorithm for 3D reconstruction of vascular trees as applied to angiography. The principle is to generate a 3D view of a tortuous object from a minimum number of 2D projections via a series of connectivity and consistency checks. In a companion paper (1996b) they performed an experimental evaluation of their algorithm by comparing the results with those from stereoscopic coronary and cerebral angiograms. The agreement was impressive and demonstrated that adequate reconstructions may be obtained with as few as three distinct views. However, the spatial resolution of angiography (>1mm), or other medical imaging modalities (at most 350μm) does not allow this method to be applied to the capillary level. Bossi *et al.* (1995) quantified the microvessel density (MVD) in random samples of microscopic fields in sections of gastrointestinal tumours. The MVD for carcinomas was found higher than that of normal tissue although it has to be mentioned that only highly vascularized tumour regions had been selected for the calculation of the former. No correlation of the MVD with metastases, disease stage and patient survival was found. They concluded that the MVD is important in tumorigenesis, but does not provide significant prognostic information.

There is a multitude of computational tools commercially available for the interpolation of surfaces smooth or otherwise, using a random set of discrete coordinate points on the surfaces as input. What limits the applicability of most of these tools to the case of interpolating a tumour surface are the irregularities in the spacing between input points and that the surface is a closed one. A large number of programs that can calculate surface areas, centroids, volumes, weights, moments, and products of inertia of complicated surfaces is also available commercially as well as in the literature (e.g. Messner & Taylor, 1980). Chamayou (1982) developed a program for B-spline interpolation of surfaces with application to computer tomography. Using the same basic concepts, Dierckx (1993) developed a code that determines a smooth bicubic spherical spline approximation to a random set of data points as input. The latter was incorporated as a subroutine in the codes developed in this project for calculations on the spatial distributions of vascular attributes in a tumour, as explained in more detail in chapter 5.

1.1 Numerical Methods

The differential equations describing the transport of plasma fluid and macromolecule in tumours, described in chapters 3 and 4, were solved using the principle of Gaussian elimination, and the numerical method of lines (Schiesser 1991). The derivations of effective spherically symmetric distributions for the vascular volume, and S/V of arbitrary shape tumours, described in chapter 5, employed B-splines to interpolate a smooth surface from an input set of discrete coordinate points. The purpose of this section is to give a rudimentary introduction to the principles of these numerical methods, to help improve the understanding of this work by a reader not familiar with applied numerical analysis. It is by no means a comprehensive review of these methods.

1.1.0 Finite Differences

The spatial derivative du(x)/dx of a function u(x) can be approximated by dividing continuous space into a grid of discrete points labelled by an index i. The value of u(x) at x_{i+1} can be calculated exactly if the value of $u(x_i)$ and all its derivatives are known. It is assumed that u(x) is always differentiable. Hence, by Taylor expansion around x_i:

$u(x_{i+1})= u(x_i) + (du(x_i)/dx)(x_{i+1} - x_i) + (1/2!)(d^2u(x_i)/dx^2)(x_{i+1} - x_i)^2 + \ldots$ (1.1)

or

$$\frac{du(x_i)}{dx} = \frac{u(x_{i+1}) - u(x_i)}{\Delta x} + O(\Delta x^2) \qquad (1.2)$$

where $\Delta x= x_{i+1} - x_i$ and $O(\Delta x^2)$ includes the second and higher order terms of the expansion. This is called a forward finite difference as the value of the derivative du(x)/dx is determined by $u(x_{i+1})$ which is the point next to $u(x_i)$ in an increasing i direction. It is a first order difference because second, and higher order terms are excluded from the evaluation of the derivative. By Taylor expansion in the reverse direction:

$u(x_{i-1})= u(x_i) + (du(x_i)/dx)(-\Delta x) + (1/2!)(d^2u(x_i)/dx^2)(-\Delta x^2) + \ldots$ (1.3)

where $-\Delta x = x_{i-1} - x_i$, or

$$\frac{du(x_i)}{dx} = \frac{u(x_i) - u(x_{i-1})}{\Delta x} + O(\Delta x^2) \qquad (1.4)$$

With a similar reasoning as above, this is called a backward first order finite difference. Subtracting equation (1.3) from (1.1):

$u(x_{i+1}) - u(x_{i-1}) = (2\Delta x)du(x_i)/dx + (2/3!)(d^3u(x_i)/dx^3)(\Delta x^3) + \ldots$ (1.5)

or

$$\frac{du(x_i)}{dx} = \frac{u(x_{i+1}) - u(x_{i-1})}{2\Delta x} + O(\Delta x^2) \qquad (1.6)$$

This is called a second order central finite difference. It is termed 'central' because the dependent variable is evaluated at points x_{i+1} and x_{i-1} which are located symmetrically (or centrally) around point x_i, at which the first order derivative is evaluated. It is termed 'second order' because the error term $O(\Delta x^2)$ follows the third derivative term, as the second order ones cancelled out.

The second order derivative approximation can be found by adding (1.1) to (1.3). The first order terms cancel, and upon rearranging one gets:

$$\frac{d^2u(x_i)}{dx^2} = \frac{u(x_{i+1}) - 2u(x_i) + u(x_{i-1})}{\Delta x^2} + O(\Delta x^3) \qquad (1.7)$$

To avoid fictitious points at the edges of an interval where a differential equation is defined ($x_1 \le x_i \le x_N$) second order finite difference expressions for $du(x_1)/dx$ and $du(x_N)/dx$ can be derived in terms of neighbouring $u(x_i)$'s within that interval. Thus, for $du(x_1)/dx$ we need two Taylor series for $u(x_2)$ and $u(x_3)$:

$u(x_2) = u(x_1) + (du(x_1)/dx)(\Delta x) + (1/2!)(d^2u(x_1)/dx^2)(\Delta x)^2 + \ldots$ (1.8)

$u(x_3) = u(x_1) + (du(x_1)/dx)(2\Delta x) + (1/2!)(d^2u(x_1)/dx^2)(2\Delta x)^2 + \ldots$ (1.9)

where $\Delta x = x_{i+1} - x_i$. Multiplying (1.8) by 4 and subtracting (1.9) we can drop out the second derivative term, and rearranging:

$$\frac{du(x_1)}{dx} = \frac{-3u(x_1) + 4u(x_2) - u(x_3)}{2\Delta x} + O(\Delta x^2) \qquad (1.10)$$

where $\Delta x = x_2 - x_1$.

Similarly, at the other end of the interval (x_N):

$$\frac{du(x_N)}{dx} = \frac{3u(x_N) - 4u(x_{N-1}) + u(x_{N-2})}{2\Delta x} + O(\Delta x^2) \qquad (1.11)$$

where $\Delta x = x_N - x_{N-1}$.

Alternatively, one can apply first order forward and backward differences at the beginning and end of the $[x_1,x_N]$ interval respectively. If the physical system described by the equation forces the first derivative to vanish at both ends of the $[x_1,x_N]$ interval then $u(x_1)=u(x_2)$ and $u(x_N)=u(x_{N-1})$. Hence:

$$\frac{d^2u(x_1)}{dx^2} = \frac{2(u(x_2) - u(x_1))}{\Delta x^2} + O(\Delta x^2) \qquad (1.12)$$

and similarly for $d^2u(x_N)/dx^2$.

Second order finite differences are used to evaluate most of the first and second order spatial derivatives encountered in the transport equations of fluid and macromolecules solved in chapters 3 & 4. There are systematic methods of finding linear combinations of a larger number of neighbouring grid points around $u(x_i)$ to create higher order finite difference formulas. The advantage these methods offer, if $u(x_i)$ is differentiable, is faster convergence for fewer grid points which saves RAM space during computation. However, they make computer codes a lot more cumbersome to implement.

1.1.0.1 Tridiagonal Matrices

The second order finite difference methods outlined above, transform a differential equation of a continuous dependent variable u(x), to a set of discrete ones. Hence, complex, non-linear equations are transformed to sets of linear equations constituting of linear combinations of $u(x_i)$ evaluated at three neighbouring grid points (i-1,i,i+1) per equation. Exceptions are the boundary grid points. Forward finite differences are applied to the first points (x_1,x_2) and backward differences to the last ones (x_{N-1},x_N), allowing only two variables per equation in order to create the matrix form shown below in eq.(1.14). The discrete equations are then rearranged, by grouping together all coefficients of $u(x_i)$ sharing the ith index. The result is a set of N linear coupled equations, where N is equal to the number of grid points that continuous space has been divided into. The general format of the equations for N=4 is:

$$\begin{aligned} a_{11}u(x_1) + a_{12}u(x_2) &= b_1 \\ a_{21}u(x_1) + a_{22}u(x_2) + a_{23}u(x_3) &= b_2 \\ a_{32}u(x_2) + a_{33}u(x_3) + a_{34}u(x_4) &= b_3 \\ a_{43}u(x_3) + a_{44}u(x_4) &= b_4 \end{aligned} \qquad (1.13)$$

In matrix form, $\mathbf{A} \cdot \mathbf{u(x)} = \mathbf{b}$:

$$\begin{pmatrix} a_{11} & a_{12} & 0 & 0 \\ a_{21} & a_{22} & a_{23} & 0 \\ 0 & a_{32} & a_{33} & a_{34} \\ 0 & 0 & a_{43} & a_{44} \end{pmatrix} \cdot \begin{pmatrix} u(x_1) \\ u(x_2) \\ u(x_3) \\ u(x_4) \end{pmatrix} = \begin{pmatrix} b_1 \\ b_2 \\ b_3 \\ b_4 \end{pmatrix} \qquad (1.14)$$

A is called a tridiagonal matrix because it has non-zero elements only on the diagonal and in the positions immediately adjacent to it. The above outlines the method with which equation (3.5) in section 3.0 was discretized.

1.1.0.2 Block-Diagonal Matrices

In the case of two coupled differential equations of the dependent variables u(x,t) and w(x,t), the same second order difference techniques were applied to obtain the relevant discretized equations for the spatial variable, as described in section 4.0.1. Since the two equations were simultaneously evaluated at the same grid points, the resulting general matrix structure resembles that of 'steps' or 'blocks', two rows wide each. These are called 'block-rows' and have their axis of symmetry along the main diagonal of the matrix. Each 'block-row' consists of three consecutive 2×2 blocks where the non-zero elements may lie. If the total number of equations is n, block rows 2 to n-1 are centred about the main diagonal. Block-rows 1 and n are the diagonal blocks and the two adjacent to the diagonal block. This means that the resulting matrix structure of the spatially discretized macromolecule transport equations is a tridiagonal one, as described in section 1.1.0.1, but each row is a 'block-row' rather than a single one. The method can be applied to larger numbers of coupled differential equations and higher order finite differences by appropriately increasing the block size.

1.1.1 Solution Methods

The time independent equations that were transformed to sets of linear equations as described in section 1.1.0.1 were solved by the method of Gaussian elimination. Time dependent problems were solved by implementing algorithms based on the numerical method of lines.

1.1.1.1 Gaussian Elimination

In a set of linear equations, one can multiply any one equation by a constant and add, or subtract it from another, thus creating new linear combinations without affecting the final result. The use of this principle to eliminate all but one variable for each equation and hence find the solution to the system is called Gaussian elimination.

In a tridiagonal matrix the second row is multiplied by an appropriate constant and added to the third one, thus eliminating a subdiagonal element of the former, leaving the diagonal and the super-diagonal elements as the only two non-zero ones in that row. The procedure is repeated for all consecutive rows until the last one is reached. Since the last only had two undetermined coefficients initially (see section 1.1.0.1), it only has one left to be determined after elimination of the subdiagonal element. Hence this is the first coefficient to be determined (a_{44} in eq. 1.8). Its value is then back-substituted to the second last equation to reduce its number of undetermined coefficients to one, etc.. In the end, **A** (eq. 1.8) is transformed to a diagonal matrix of coefficients. Hence, the system is solved unless there are not enough equations for the given number of variables and the system is said to be underdetermined.

This method of Gaussian elimination can be applied to time independent discretized differential equations of the general form:

$$\frac{d^2u(x)}{dx^2} + g(x)\frac{du(x)}{dx} + f(x) = 0 \qquad (1.15)$$

given that u(x) is a differentiable function and g(x) and f(x) can be evaluated at all x_i in $[x_1,x_N]$. The method will work because the discretization will result in a set of N linear equations in $u(x_i)$. Another solution method has to be employed if the discretized equations describing a physical problem contain non-linear $u(x_i)$ terms.

1.1.1.2 The Numerical Method of Lines (NUMOL)

In section 1.1.0 the spatial discretization of a differential equation with one dependent variable, u(x), was described. The NUMOL deals with dependent variables that are also a function of time. Hence, the index i is retained to account for spatial variation of $u(x_i)$ w.r.t. x, but t is treated as a continuous variable. This leads to a system of linear, constant coefficient ordinary differential equations (ODEs) where the only independent variable is t. Trial solutions of the form $u_i=C_ie^{\lambda t}$ are then used to solve the resulting

algebraic problem. The name NUMOL originates from the evolution of u(x,t), from t=0, along lines of constant x, where each grid point is. To demonstrate the principle we can apply this to the simplest form of two simultaneous ODE's:

$$\frac{du_1}{dt} = a_{11}u_1 + a_{12}u_2 \qquad (1.16)$$

$$\frac{du_2}{dt} = a_{21}u_1 + a_{22}u_2 \qquad (1.17)$$

and apply trial solutions

$$u_1(t) = C_1 e^{\lambda t} \qquad u_2(t) = C_2 e^{\lambda t} \qquad (1.18) \quad (1.19)$$

Substituting (1.18) and (1.19) in (1.16) and (1.17):

$$\lambda C_1 e^{\lambda t} = a_{11}C_1 e^{\lambda t} + a_{12}C_2 e^{\lambda t} \qquad (1.20)$$

$$\lambda C_2 e^{\lambda t} = a_{21}C_1 e^{\lambda t} + a_{22}C_2 e^{\lambda t} \qquad (1.21)$$

After cancelling the common factor $e^{\lambda t}$ and rearranging, we arrive at two homogeneous, linear, algebraic equations for the two constants C_1 and C_2:

$$(\lambda - a_{11})C_1 - a_{12}C_2 = 0 \qquad (1.22)$$

$$-a_{21}C_1 + (\lambda - a_{22})C_2 = 0 \qquad (1.23)$$

A non-trivial solution exists if and only if the determinant of the coefficient matrix is zero:

$$\lambda^2 - (a_{11} + a_{22})\lambda + (a_{11}a_{22} - a_{12}a_{21}) = 0 \qquad (1.24)$$

In the above equation λ is of the same order as the number of initial equations (2 in this case). The roots of (1.22) are λ_1 and λ_2 allow the general solution of (1.16) and (1.17) to be evaluated:

$$u_1 = C_{11}e^{\lambda_1 t} + C_{12}e^{\lambda_2 t} \qquad (1.25)$$

$$u_2 = C_{21}e^{\lambda_1 t} + C_{22}e^{\lambda_2 t} \qquad (1.26)$$

The above equations are linear combinations of the assumed solutions. This superposition of solutions is possible since equations (1.16) and (1.17) are linear. For a convergent solution to exist all eigenvalues must have negative real parts. The separation of the eigenvalues determines the stiffness of the ODE problem.

The same principles applied to linear ODEs can also be applied to non-linear ODEs like eq.(4.1) for non-binding macromolecule and eq.(4.15) and (4.16) for binding macromolecule. This involves approximating the non-linear ODEs in a linear regime. The mathematical details of the process are involved and only the basic principle is shown here. The matrix form of the non-linear equations to be solved is:

$$\frac{d\boldsymbol{u}}{dx} = \boldsymbol{f}(\boldsymbol{u},t) \qquad (1.27)$$

and

$$\boldsymbol{y}(t_0) = \boldsymbol{y}_0 \qquad (1.28)$$

where

$$\boldsymbol{u} = [u_1\ u_2\ \ldots\ u_N]^T \qquad (1.29)$$

$$\boldsymbol{f} = [f_1\ f_2\ \ldots\ f_N]^T \qquad (1.30)$$

$$\boldsymbol{y}_0 = [y_{1,0}\ y_{2,0}\ \cdots\ y_{N,0}]^T \qquad (1.31)$$

If **f** in eq.(1.27) is expanded in a Taylor series around the point ($\mathbf{y}_s$,t_s) and then truncated after the linear terms:

$$\frac{d\boldsymbol{u}}{dt} = \boldsymbol{f}(\boldsymbol{u}_s,t_s) + \boldsymbol{J}(\boldsymbol{u}_s,t_s)(\boldsymbol{u}-\boldsymbol{u}_s) \qquad (1.32)$$

where **u_s** is the dependent variable vector **u** at a particular value of t, t_s. **J** is the ODE Jacobian matrix

$$\boldsymbol{J} = \begin{pmatrix} f_{11} & f_{12} & \cdot & f_{N1} \\ f_{21} & f_{22} & \cdot & f_{N2} \\ \cdot & \cdot & \cdot & \cdot \\ f_{N1} & f_{N2} & \cdot & f_{NN} \end{pmatrix} \qquad (1.33)$$

where $f_{ij}=\partial f_i/\partial y_j$; i=1,2,...,N ; j=1,2,...,N. Thus the Jacobian matrix is the NxN matrix of all possible first order derivatives of f_1 to f_N with respect to the dependent solution vector **y**. This matrix allows the approximation of a set of non-linear equations to a set of linear

ODEs and plays a significant role in scientific numerical computing.

1.1.2 B-Splines

The derivation of effective spherically symmetric distributions of the vascular volume per unit volume of tumour and S/V requires the knowledge of blood vessel coordinates w.r.t. the tumour surface. Since a discrete set of coordinates on the tumour's surface is usually obtained experimentally, a way of interpolating a smooth surface through them was required. B-splines are a widely used tool in computer graphics for this purpose. They have the important property of staying within the polygon determined by the given points. Also, changes in the position of the points will have a 'local' effect on the surface rather than a 'global' one, as is the case for the cubic splines. In regular cubic and B-splines a separate cubic polynomial is derived for each pair of neighbouring points of the set for interpolating points inbetween. However, the B-spline needs not pass through any points of the input set, whereas the cubic spline is defined to do so.

Given the point $p_i=(x_i,y_i)$, i=0,1,...,N the cubic B-spline for interval (p_i,p_{i+1}), i=1,2,...,N-1, is given by:

$$B_i(u) = \sum_{k=-1}^{2} b_k p_{i+k} \qquad (1.34)$$

where

$$b_{-1} = \frac{(1-u)^3}{6} \qquad (1.35)$$

$$b_0 = \frac{u^3}{2} - u^2 + \frac{2}{3} \qquad (1.36)$$

$$b_1 = -\frac{u^3}{2} + \frac{u^2}{2} + \frac{u}{2} + \frac{1}{6} \qquad (1.37)$$

$$b_2 = \frac{u^3}{6} \qquad 0 \le u \le 1 \qquad (1.38)$$

The weighted sum, as u varies from 0 to 1, generates the B-spline curve. The form of the B-polynomials is such that the continuity of the curve and its first and second derivatives at all points where the B-spline segments connect, is ensured. Appropriate coordinate transformations can yield B-splines in spherical polars.

PART II: THE ANIMAL EXPERIMENTS

2. The Nude Mouse Model

This chapter describes the experimental procedures, calculations and interpretation of the results, and discussion of the limitations of the methodology for a few experiments designed to quantify the total vascular volume and vascular permeability of the SKOV3ip1 human ovarian tumours (Yu Dihua *et al.* 1993) grown in nude mice. The vascular permeability is defined as the plasma extravasation rate per gram of tumour. The results also show how these quantities vary with tumour weight.

2.0 The Experiments

A previously reported experimental protocol was used (Song 1970), the only differences being :

1) A non-specific human IgG was used instead of human serum albumin for vascular permeability measurements.

2) ^{131}I was used instead of ^{125}I as the 0.364 MeV gamma of the former is much more penetrating than that of the latter, so we didn't have to correct for self-absorption in the tumours that were up to 1cm in size.

3) ^{99m}Tc rather than ^{51}Cr was used to label red blood cells, because the former was more readily available to this project than the latter.

4) Red blood cell labelling was done in vivo rather than in vitro. This simplified procedure took advantage of the high affinity of ^{99m}Tc for red blood cells.

2.0.1 Materials and Methods

2.0.1.1 The Iodination of IgG

The first step in the experiments was to iodinate a non-specific human IgG in vitro for later injection in the mouse. The protocol used for the iodination had been developed

in our lab for the iodination of IgG with ^{125}I, or ^{131}I (Kwok *et al.* 1989). In brief, the following method was followed:

First, the following three buffer solutions were prepared:

(1) 5% v/v KI solution in double distilled H_2O (DDH_2O)

(2) 0.1 M Metabisulfate in DDH_2O

(3) 0.1 M Hepes solution pH 7.4 in DDH_2O

Iodogen coated tubes were prepared by adding 200µl of 57.9µM iodogen in chloroform in each of 1ml micro-tubes and then letting nitrogen at 8psi (flow rate ~1 l/min) blow in the tubes to coat a thin layer of iodogen on the bottom of the tubes. This coated area was larger than the area occupied by the usual volume of reaction which was 150µl, so that the iodination reaction could take place efficiently. The tubes were stored at −20°C before iodination. An estimated 50µg of IgG was needed to inject 4-5 mice per experiment. There should also be enough radioactivity in the tumours to obtain significantly higher count rate than background in gamma-counting. To obtain that, 2mg of IgG were diluted in 1ml of the Hepes buffer. A 25µl aliquot of the IgG solution and 25µl of Hepes were added to a clean tube. Upon the addition of 100µl (100µCi) carrier free sodium ^{131}I iodide solution to the tube, the total reaction volume was about 150µl. The iodination reaction took place in a fume hood in an isotope room as some ^{131}I vapour could be created during the reaction. All work was done behind a lead glass and such safety measures as wearing double disposable gloves, a lead apron and a TLD badge were observed. Once the reaction solution was transferred into an iodogen tube, it was placed inside a styrofoam cup containing 37°C water surrounded by a lead container for 10 minutes while it was being occasionally stirred. The reaction was stopped by transferring the entire mixture into a clean uncoated tube.

The efficiency of the iodination reaction was tested by ITLC (Instant Thin Layer Chromatography). 2µl of the reaction mixture was added to 50µl of metabisulfate solution. After mixing for 30 sec, 2µl of the mixture was spotted at the origin of an ITLC paper. The paper was in the form of a narrow rectangular strip measuring 1cm x 10cm and the origin was chosen to be 1cm away from one of its short sides. The strip was allowed to dry for 5 minutes in air. 5ml of 5% v/v KI solution was poured in a 150ml beaker and

the ITLC paper was placed vertically in it for 2min 30s. The IgG-^{131}I fraction stayed at the origin and free iodide washed to the upper end of the ITLC paper. The lower third of the ITLC paper, being considered as the origin, was cut from the upper two thirds being considered as the front. A gamma counter was set to have an acceptance window that would encompass the ^{131}I principal gamma-ray at 0.364 MeV. The efficiency of the iodination is then calculated as the gamma count rate for the origin divided by the sum of count rates for the origin and the front.

The stock IgG-^{131}I solution was stored at a 4°C fridge where it could remain stable chemically for about a week. This is supported by the fact that when the ITLC procedure was repeated a week later on a batch of IgG-^{131}I, the percentage of iodine bound to antibody was reduced from an original value of ~80% to ~27%.

2.0.1.2 The Animal Experiment Protocol

The first step in this part was to label the red blood cells of the mice with ^{99m}Tc-pertechnetate in vivo. For that purpose a previously reported clinical protocol was used (Pavel 1977), adjusted for mice. The following agents were obtained from the nuclear medicine department of the Hamilton Henderson Hospital for each experiment:

(1) 0.1ml $SnCl_2$ (0.106M) undiluted

(2) 1.9ml Pyrophosphate (0.074M) undiluted

(3) 1mCi ^{99m}Tc-pertechnetate in 1ml

The vials for (1) and (2) had to be purged of air by flushing with nitrogen gas before adding the reagents. (1) and (2) made a mixture of 2ml total volume which was diluted 5 times with 0.9% saline to 10ml. This was done so that the injection volume to each mouse would not be too small. It is important that this happens only immediately before injecting in the mice as the pyrophosphate would be reduced by $SnCl_2$ upon mixing in the vial. The amount of reagent mixture to be injected i.v. in the tail of each mouse was determined as follows:

The average human adult weighs 70Kg and the average adult mouse 30g. Since the recommended dose for humans is 2ml of the undiluted reagent mixture, the quantity

to be injected per mouse should be reduced by the respective weight ratio multiplied by 10 thus approximately compensating for the higher metabolic rate of the mice. This works out to be 8.6μl which was rounded to 10μl of the original mixture, or 50μl of the diluted reagent mixture.

Since nude mice are hard to inject multiple times because of their fine tail veins, 30min after the injection of the pyrophosphate mixture both ^{99m}Tc-pertechnetate and ^{131}I-IgG were injected as a mixture in one shot. Approximately 100μCi of ^{99m}Tc and 100μCi of ^{131}I-IgG were injected in each mouse and a known volume of the radioactive mixture was also kept as a standard. The injection volume per mouse was approximately 100μl. 30 minutes later the animals were sacrificed by cervical dislocation and immediately cut open to withdraw blood from the heart before clotting occurred. The blood was placed in pre-marked heparinized tubes (50μl of 10,000 i.u./ml heparin per tube, 0.5ml of blood per mouse).

The tumours were carefully excised so that as little surrounding tissue remained on them as possible and were weighed and gamma-counted together with the blood samples. The gamma counter had been adjusted to have two windows open to encompass the 0.141 MeV ^{99m}Tc and the 0.364 MeV ^{131}I gammas. The dual labelled standard was also counted so that the counting efficiency of the gamma counter could be found. The blood samples were then spun at 1000rpm for 20min which is a relatively low speed to avoid RBC lysing during centrifugation. As much plasma as possible in each blood sample was extracted. The volumes of plasma were measured and the gamma emissions counted.

2.0.2 Calculations

In all experiments the same data processing method was followed. In this section window A refers to the ^{99m}Tc counting window and window B to the ^{131}I counting window:

(1) First the fraction of spill-over of ^{131}I in the ^{99m}Tc window was calculated by simply taking the ratio of the count rates in windows A and B for the ^{131}I standard. The ratio of ^{131}I to ^{99m}Tc activity in the dual labelled mixture was determined at the time of mixing

and there was enough activity in the standard for the background to be negligible. The percentage spill-over was determined to be 10.15 ± 0.17 %.

(2) For each tumour the ^{99m}Tc activity associated with each gram of the tumour was calculated:

(i) The ^{99m}Tc window counts per minute (CPMA) were corrected for background.

(ii) The ^{131}I window counts per minute (CPMB) were corrected for background.

(iii) Using the calculated spill-over percentage above, the spill-over in window A from ^{131}I was determined.

(iv) The corrected CPMA for ^{99m}Tc activity was the difference between (i) and (iii).

(v) The ^{99m}Tc activity per gram of tissue was finally calculated by dividing (iv) by the individual tumour weight.

(3) Knowing (2) and the measured ^{99m}Tc activity for the measured volume of whole blood for each mouse, the vascular volume in 1g of tumour could be calculated according to (Song 1970) :

Vascular Volume per g of tissue = ml of blood / g of tissue

$$= \frac{99m\text{-}Tc \text{ activity / g of tissue}}{99m\text{-}Tc \text{ activity / ml of whole blood}} \qquad (2.1)$$

(4) The vascular permeability of the tumour blood vessels was then calculated as follows:

(i) The counts per minute for ^{131}I (CPMB) in the tumour samples were corrected for background and divided by the individual tumour weights.

(ii) The ^{131}I activity per ml of plasma was calculated by dividing the background corrected CPMB's for plasma with their respective plasma volumes.

(iii) The total plasma volume in each tumour was calculated by dividing (i) by (ii) and correcting for the time difference between the time of measurement of whole blood in the tumour and that of plasma for each mouse.

(iv) The intravascular plasma volume in tumour was then calculated by multiplying (1 - Haematocrit) to the vascular volume calculated above by eq. (2.1). The

haematocrit was obtained for each mouse from the centrifugation of the whole blood samples using haematocrit tubes.

(v) Finally, the vascular permeability was calculated by subtracting (iv) from (iii). Thus, the final result was quantified as ml of plasma extravasated in 1 hour / g of tissue (see section 2.0.4 for comments).

(vi) The in vivo labelling efficiency of ^{99m}Tc to RBC's was calculated in retrospect by subtracting the ^{99m}Tc count in plasma from that in whole blood and dividing by the whole blood count. Ideally, there should be no ^{99m}Tc counts in the plasma except perhaps for some debris from RBC's that have lysed during centrifugation.

(5) Since the labelling efficiency of the RBC's as well as that of IgG was not 100% and was variable for each experiment, the following procedure was followed in order to correct for the variation. Pooling results from different experiments would then be possible.

By defining the following relevant parameters:

x = Tc activity associated with RBC's per gram of tissue,

A_{RBC} = Tc activity associated with RBC's per ml of blood,

A_B = total Tc activity per ml of blood,

A_P = Tc activity associated with plasma per ml of blood,

A_T = Tc activity in 1g of tissue,

A_{TP} = Tc activity associated with plasma in 1g of tissue, and

A_{EF} = Tc activity associated with the extracellular fluid compartment of 1g of tissue,

$A_T = x + A_{EF} + A_{TP} = A_{EF} + x*(1 + A_P/A_{RBC})$ (2.2)

where $A_{EF} \simeq 0.243*A_P/(1 - \text{Haematocrit})$, and 0.243 is an estimated fraction of extracellular space in a human tumour xenograft (Sung 1990).

And so, the vascular volume can be calculated as:

$$v.v.\ (ml/g) = \frac{(A_T - A_{EF})}{(1 + A_P / A_{RBC}) * A_{RBC}} \qquad (2.3)$$

2.0.3 Results

The results of three experiments were analysed. In the first experiment the labelling efficiency of the RBC's was around 90%. In the latter two it was around 40%. This complicated the interpretation of the results especially for larger tumours that had larger volumes of blood in them. In all the cases where the numbers didn't make sense e.g. negative numbers when using eq. (2.2), the respective tumours were not considered as valid data points and were not included in Table 2.1.

Table 2.1 Vascular Volume and Vascular Permeability of SKOV3ip1 Human Tumour

Tumour Weight ± 0.001 (g)	Total vascular volume ± σ (ml × E-05)	Total Vascular Permeability ± σ (ml/h)
0.006	6 ± 1	0.0055 ± 0.0010
0.019	10 ± 2	0.0105 ± 0.0006
0.025	37 ± 2	0.0266 ± 0.0013
0.030	24 ± 2	0.0144 ± 0.0006
0.041	44 ± 2	0.0174 ± 0.0008
0.050	71 ± 2	0.0165 ± 0.0010
0.082	54 ± 2	0.0043 ± 0.0016
0.145	45 ± 2	0.0860 ± 0.0029
0.166	101 ± 2	0.0451 ± 0.0009
0.183	130 ± 2	0.0916 ± 0.0036
0.183	116 ± 2	0.0552 ± 0.0011
0.245	137 ± 3	0.1260 ± 0.0021
0.581	335 ± 5	0.3014 ± 0.0051

Xenografts to a Non-specific Human IgG.

Fig. 2.1 shows the variation of total vascular volume (ml) with tumour weight (g). A linear equation was fitted through the data points. The fitted equation was found to be y=(0.001±0.001) + (0.055±0.004)*x. There is no fundamental reason why the data points should obey a strict proportionality law although the fitted curve should pass through the origin. This means that in the SKOV3 tumour-nude mouse model, for tumours up to ~1cm^3 in size, necrotic cores are absent. This suggests that for up to that tumour size angiogenesis occurs as rapidly as the tumour grows. Presumably, necrotic cores can be seen in bigger tumours in a rat or a rabbit. The average value of vascular volume per gram for the above data points was 0.0797±0.0350 ml/g (coeff. of determination r^2= 0.955) showing a large degree of variability between tumours, which is expected. Fig. 2.2 shows the variation of total vascular permeability (ml of extravasated plasma/h post-injection) with tumour weight. The fitted equation was y=(-0.008±0.007) + (0.512±0.036)*x. The average value for all data points was 0.502±0.263 ml/g/h (r^2=0.948). The large S.D. suggests possible variations in total vascular volume between tumours of the same weight there are also variations in the permeability of the vessels themselves.

The measured activity of the standard which is a sample of the dual-labelled injection mixture can be used to estimate the total blood volume and hence the total vascular volume of the mouse. Knowing the activity of a known blood volume in the standard, the injected volume of radioactive solution for each mouse plus the respective measured activity / ml of blood, we can do the following calculation:

(i) The count rate / volume of standard (10µl) in window A is first corrected for spill-over from the iodine window, for background and the time difference between the measurement of the blood sample and that of the standard.

(ii) The net count rate per 10µl in (i) is converted to cpm/µl of radioactive solution and multiplied by the injected volume.

(iii) The result of (ii) in cpm is divided by the cpm/ml of whole blood for each mouse. The calculated total blood volume of each mouse varied from 40ml/kg (or 1ml for a 25g mouse) to over 200ml/kg. The textbook value (Harkness & Wagner) is 76-80 ml/kg. The

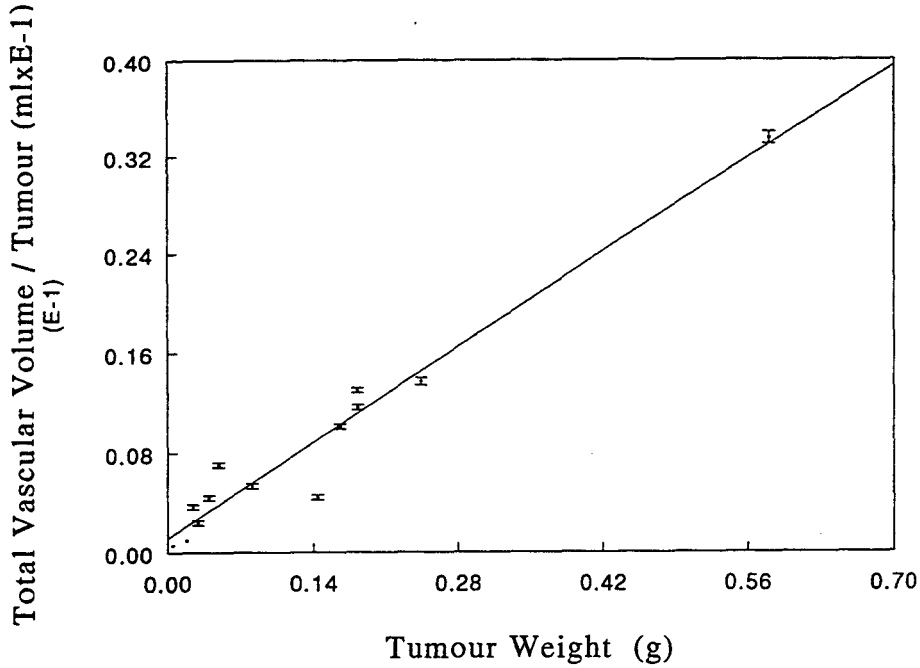

Fig 2.1 The total vascular volume (ml) vs tumour weight (g).

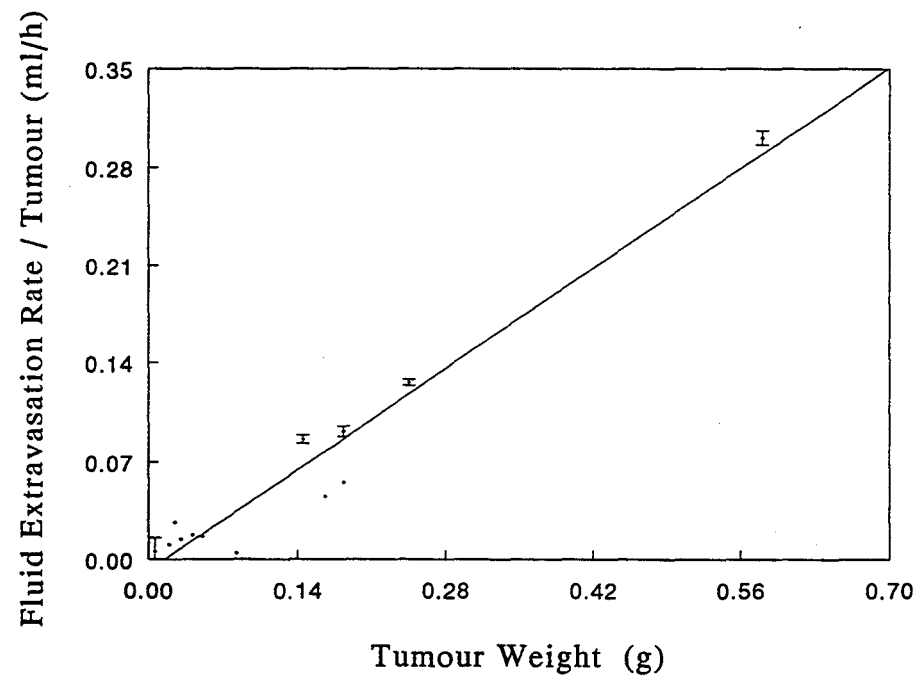

Fig 2.2 The total plasma fluid extravasation rate (ml/h) vs tumour weight (g).

reason that the total blood volume for several mice, which were excluded from the final results, was significantly higher than the literature value was that the unbound ^{99m}Tc escaped into the extravascular space.

2.0.4 Limitations / Problems of the Experiment

The following limitations / problems were realised in retrospect:

(i) The efficiency of labelling of IgG with ^{131}I was not sufficiently high at times and was variable between different iodination experiments. This seems to imply that the protocol was not optimized for labelling relatively large quantities of protein. Also, there was a time lapse of a few days between the receipt of ^{131}I from its supplier and the IgG iodination, so one has to ensure that enough activity is available at the time of experiment.

(ii) The in vivo labelling efficiency of RBC's with ^{99m}Tc was very variable with very little control available to the experimenter. It is proposed that the labelling should be done in vitro (incubation and washing) with the RBC's and the labelled RBC's be injected back in the mice so that there is better control over the efficiency of the labelling.

(iii) The amount of IgG extravasating is not a linear function of time (Hamberg 1994). In order to convert all permeability values to ml/g/h one multiplies all calculated permeabilities by the time difference between the radioactivity injection and the time of sacrifice of each mouse expressed as a fraction of the hour, thus implicitly doing a linear extrapolation.

(iv) Since the tumours were variable in size and shape and an antibody could practically be anywhere in them, there is a variable degree of self-absorption of the gammas in the tumour before they reach the detector. That difficulty was largely overcome by using ^{131}I which emits hard gammas rather than using ^{125}I and then trying to create a calibration curve for increasing tissue thicknesses. However, greater care had to be taken in shielding for the ^{131}I gammas during handling.

PART III: MATHEMATICAL MODELLING OF MACROMOLECULE TRANSPORT IN TUMOURS

3. A Mathematical Model for the Interstitial Plasma Pressure and Velocity Spatial Distributions in Tumours.

This chapter examines a model proposed by Baxter and Jain (1989) predicting the steady-state spatial variation of the interstitial pressure and velocity radial profiles for a tumour imbedded in normal tissue. The correct analytical solutions of the equations, which are different from the ones reported, were found. The changes and sensitivity of these profiles to variation of vascular perfusion conditions were investigated.

3.0 Definition of the Interstitial Fluid Pressure Equation for a Uniformly Perfused Tumour

The previously proposed macroscopic fluid transport model (Baxter & Jain 1989) is briefly presented here :

The interstitial velocity u_i of an incompressible fluid in a porous medium is given by Darcy's law

$$\mathbf{u}_i = -K\nabla p_i \qquad (3.1)$$

where K is the hydraulic conductivity of the interstitium (cm^2/mm Hg-sec) and p_i is the interstitial pressure (mm Hg). The continuity of flow equation inside and outside the tumour is defined as

$$\nabla \cdot \mathbf{u}_i = \phi_V(r) - \phi_L(r) \qquad (3.2)$$

where $\phi_V(r)$ is the fluid source term (sec^{-1}), and $\phi_L(r)$ is the lymphatic drainage term (sec^{-1}) which were defined as follows:

$$\phi_V(r) = \frac{J_V}{V} = \frac{L_p S}{V}(p_V - p_i - \sigma_T(\pi_V - \pi_i)) \qquad (3.3)$$

$$\phi_L(r) = \frac{J_L}{V} = \frac{L_{pL} S_L}{V} (p_i - p_L) \qquad (3.4)$$

The parameters in the above equations were defined as :

J_V/V = Volume flow rate out of the vasculature per unit volume of tissue (sec^{-1})

J_L/V = Volume flow rate into the lymphatics per unit volume of tissue (sec^{-1})

S/V = Surface area per unit volume for transcapillary exchange (cm^{-1})

= 200 for tumour (Jain 1987b)

= 70 for normal tissue (Pappenheimer *et al.* 1951)

L_p = Hydraulic conductivity of the microvascular wall (cm/mm Hg-sec)

= 2.80×10^{-7} for tumour (Baxter & Jain 1989)

= 0.36×10^{-7} for normal tissue (Rippe *et al.* 1978)

L_{pL} = Hydraulic conductivity of the lymphatic wall (cm/mm Hg-sec)

= 0 for tumour

$L_{pL} S_L/V = 5.56 \times 10^{-5}$ for normal tissue (Baxter & Jain 1990)

p_V = Vascular pressure (mm Hg)

= 15.6 for both tumour and normal tissue (Brace & Guyton 1977)

p_L = Hydrostatic pressure in the lymphatics (mm Hg)

= 0 for both tumour and normal tissue (no existing data, rapid fluid removal assumed)

σ_T = Average osmotic reflection coefficient for plasma proteins

= 0.82 for tumour (Ballard & Perl 1978)

= 0.91 for normal tissue (Curry 1984)

π_V = Osmotic pressure of the plasma (mm Hg)

= 20 for both tumour and normal tissue (Brace & Guyton 1977)

π_i = Osmotic pressure of the interstitial fluid (mm Hg)

= 15 for tumour (Baxter & Jain 1989)

= 10 for normal tissue (Wiederhielm 1979)

Combining equations (3.1) to (3.4) one gets :

$$\nabla^2 p_i = \frac{\alpha^2}{R^2}(p_i - p_{ss}) \qquad (3.5)$$

where

$$\alpha = R\sqrt{\frac{(L_p S + L_{pL} S_L)}{K V}} \qquad (3.6)$$

and

$$p_{ss} = \frac{(L_p S p_e + L_{pL} S_L p_L)}{(L_p S + L_{pL} S_L)} \qquad (3.7)$$

In the above,

$$p_e = p_V - \sigma_T(\pi_V - \pi_i) \qquad (3.8)$$

is an effective pressure (mm Hg) and R is the radius of the tumour. The negative sign in the osmotic pressure component of p_e implies that a higher protein concentration in the vasculature, will induce plasma flow in it, and out of the tumour interstitial space. This will tend to make the two concentrations equal, and to reduce the interstitial plasma pressure.

The following boundary conditions apply to eq. (3.7) :

(i) No-flux condition at the centre of the tumour due to radial symmetry.

$$\nabla p_i \,|_{r=0} = 0 \qquad (3.9)$$

(ii) Continuity of pressure at a long distance outside the tumour.

$$p_i \,|_{r\to\infty} = p_{ss} = p_\infty \qquad (3.10)$$

(iii) Continuity of pressure at the tumour - normal tissue interface.

$$p_i \big|_{r=R^-} = p_i \big|_{r=R^+} \qquad (3.11)$$

(iv) Continuity of fluid velocity at the tumour - normal tissue interface.

$$- K_T \frac{dp_i}{dr}\bigg|_{r=R^-} = - K_N \frac{dp_i}{dr}\bigg|_{r=R^+} \qquad (3.12)$$

where $K_T = 4.13 \times 10^{-8}$, and $K_N = 8.53 \times 10^{-9}$ (cm^2/mm-Hg).

3.0.1 The Analytical and Numerical Solution for Interstitial Pressure for a Well Perfused Tumour

The analytical solution of (3.5) is shown below.

(a) Inside the tumour, it was verified to be :

$$\hat{p}_1 = \frac{p_i - p_\infty}{p_e - p_\infty}$$

$$= 1 - \frac{1}{\hat{r}} \frac{(1 + \alpha_N) \sinh[\alpha_T \hat{r}]}{(1 + \alpha_N) \sinh[\alpha_T] + \hat{K}(\alpha_T \cosh[\alpha_T] - \sinh[\alpha_T])} \quad , \quad r<R \qquad (3.13)$$

where $\hat{r}$ is the dimensionless radial position (r/R). When α (eq. 3.6) is evaluated in the tumour area it is denoted as α_T, and in normal tissue as α_N.

(b) Outside the tumour, with $\hat{p}_2$ defined as in eq. (3.12), the proposed corrected solution is :

$$\hat{p}_2 = \frac{1}{\hat{r}} \frac{\hat{K}(\alpha_T \cosh[\alpha_T] - \sinh[\alpha_T])(\sinh[\alpha_N \hat{r}] - \cosh[\alpha_N \hat{r}])}{(\hat{K}(\alpha_T \cosh[\alpha_T] - \sinh[\alpha_T]) + (1 + \alpha_N)\sinh[\alpha_T])(\sinh[\alpha_N] - \cosh[\alpha_N])} ,$$

$$r>R \qquad (3.14)$$

where $\hat{K}$ is the ratio K_T/K_N.

The difference with the previously proposed form of eq. (3.14) is that the second left parenthesis in the denominator has been added. Equations (3.13) and (3.14) are plotted in fig. 3.1. Because of the homogeneity of perfusion both inside and outside the tumour the radial pressure profile switches between two plateau values (p_e, eq. 3.8) steeply at the interface where the physiological parameters change abruptly.

Equation (3.5) was also solved numerically using first order finite differences for the spatial discretization. This resulted in a tridiagonal matrix structure where the number of rows was equal to the number of grid points (N) assumed along the tumour radius. Subroutine PDIAG (Gerald & Wheatley 1989) was inserted in a FORTRAN 77 code written to perform Gaussian elimination on the tridiagonal system. The coefficients of N equations were stored in an N×4 array A. The first column of A stored the elements to the left of the diagonal, the second held the diagonal ones ,and the third the ones to the right. The fourth column held the right hand side terms. The solution vector was returned in the fourth column of A.

The numerical results fitted the analytical ones very closely and were stable to variations of the radial grid spacing.

3.0.2 Conservation of fluid

Since the interstitial pressure equation is time independent the total amount of plasma extravasating should be equal to the total amount of plasma being reabsorbed by the lymphatics or going back into the capillaries, or else there would be an ever increasing pressure build-up. This was first proved analytically by integrating two

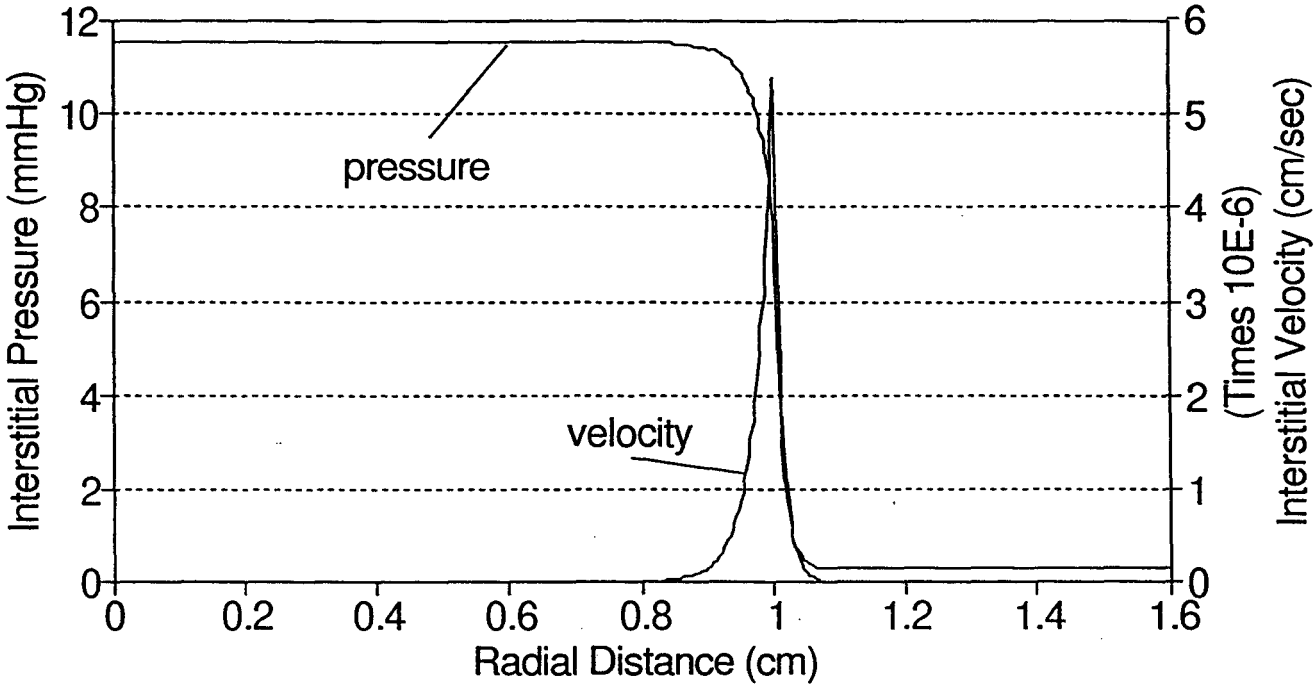

Fig. 3.1 The extravasated interstitial fluid pressure and velocity radial profiles for a 1cm radius tumour.

arbitrary functions $p_1(r)$, and $p_2(r)$ that obey eq. (3.5) over all space. It was shown that:

$$\int_0^{R_T^-} [\phi_V(r) - \phi_L(r)]4\pi r^2 dr = -4\pi R_T^2 K_T \left.\frac{\partial p_1(r)}{\partial r}\right|_{r=R_T^-} \tag{3.15}$$

and

$$\int_{R_T^+}^{\infty} [\phi_V(r) - \phi_L(r)]4\pi r^2 dr = 4\pi R_T^2 K_N \left.\frac{\partial p_2(r)}{\partial r}\right|_{R_T^+} \tag{3.16}$$

The above, together with eqs. (3.11) and (3.12) prove that there will always be conservation of fluid for this formulation irrespective of the actual form of the analytical solution, or the values that physiological parameters take.

It was also proved that $p_1(R_T) = p_2(R_T)$. When the actual analytical solution was evaluated for the particular form of $\phi(r)$ at the tumour - normal tissue interface the solution on either side of the interface collapsed to the identical analytical expression:

$$\hat{p}(R_T) = \frac{\hat{K}\,(\alpha_T \cosh(\alpha_T) - \sinh(\alpha_T))}{(\hat{K}\,(\alpha_T \cosh(\alpha_T) - \sinh(\alpha_T)) + (1 + \alpha_N)\sinh(\alpha_T))} \tag{3.17}$$

The respective analytical integral was also evaluated and fluid conservation was confirmed. Fig. 3.2 shows the variation of $\phi(r)$ with radial distance.

For the numerical solution case, conservation of fluid was verified using the following two methods:

(i) The trapezoidal rule using an integration step equal to the grid spacing.

(ii) The CSITG imsl-library cubic spline integrator calling subroutine CSINT which evaluated the local cubic spline coefficients. It was found that the accuracy of the integrator was optimal, when comparing with the analytical solution integral, when the number of piecewise intervals was defined equal to the number of grid points where $\phi(r)$

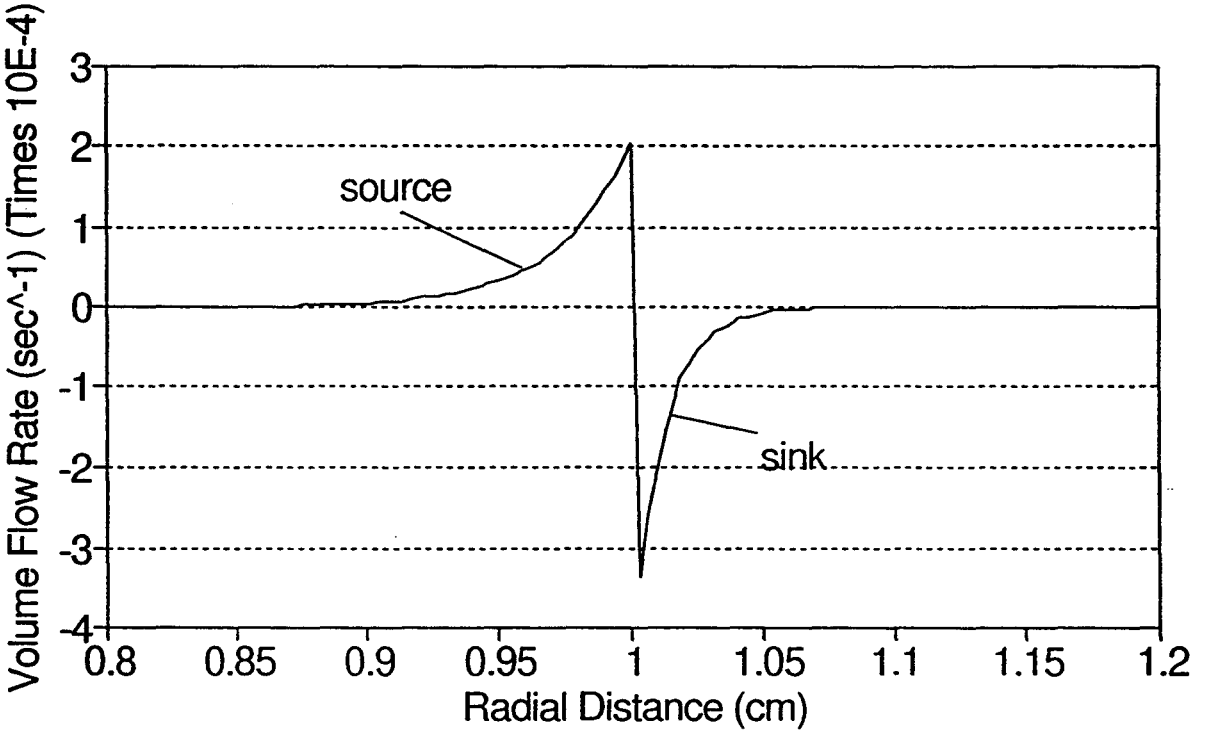

Fig. 3.2 The radial variation of the transcapillary fluid source terms (eqs. 3.3 - 3.4). Negative values indicate that the capillaries are forced to become sinks due to the fluid overflow at the edge of the tumour[1].

[1] The parenthesis accompanying the y-axis title and units, e.g. (Times 10E-4), implies that all y-axis values are being multiplied by that number. This applies to all the graphs in this thesis where this type of parenthesis appears.

was evaluated.

3.1 Definition of the Interstitial Fluid Pressure Equation for a Tumour with a Variable Size Necrotic Core, or Radially Variable Surface Area for Transcapillary Exchange per Unit Volume.

The interstitial fluid equation has the same form as eq. 3.2, the only difference being that within the necrotic core there are no fluid sources:

$$\phi(r) = 0 \quad , \quad r<R_n \qquad (3.18)$$

Boundary conditions (3.10) - (3.11) also apply to the viable tumour - necrotic core interface.

In the case of a radially variable S/V, a weighting function was defined and multiplied to the baseline value of S/V. It defined an array of dimension equal to the total number of grid points assumed in the tumour area when the finite difference method was used, or the total number of points where eq. 3.13 was evaluated.

Two forms of weighting functions were used:

(i) A sigmoid of the form,

$$g(r) = D + \frac{A}{1 + e^{-\frac{(r-B)}{C}}} \quad , r < R_T \qquad (3.19)$$

(ii) An exponential of the form,

$$g(r) = A\, e^{\frac{B(r-R_T)}{R_T}} \quad , r < R_T \qquad (3.20)$$

all other parameters remaining unchanged.

3.1.1 The Analytical and Numerical Solutions for Interstitial Pressure for a Tumour with a Variable Size Necrotic Core, or Radially Variable S/V.

The correct analytical solution which is different from the one previously proposed (Baxter & Jain 1990) was found. First, one defines

$$\Psi_1 = \hat{K}\{(\alpha_T^2 \nu - 1)\sinh(\alpha_T[1 - \nu]) + \alpha_T(1 - \nu)\cosh(\alpha_T[1 - \nu])\} \tag{3.21}$$

$$\Psi_2 = (1 + \alpha_N)\{\alpha_T \nu \cosh(\alpha_T[1 - \nu]) + \sinh(\alpha_T[1 - \nu])\} \tag{3.22}$$

$$\Psi_3(r) = (1 + \alpha_N)\{\alpha_T \nu \cosh(\alpha_T[\mu - \nu]) + \sinh(\alpha_T[\mu - \nu])\} \tag{3.23}$$

where $\hat{K}= K_T/K_N$,$\nu= R_n/R$, and $\mu= r/R$. Then, the solution can be written as:

(i) Inside the necrotic core,

$$p_{NC}(r) = p_{SST} - \frac{(p_{SST} - p_{SSN})(1 + \alpha_N)\alpha_T}{(\Psi_1 + \Psi_2)} \tag{3.24}$$

where p_{SST} and p_{SSN} are the evaluated forms of eq.(3.7) in tumour and normal tissue respectively.

(ii) In the viable tumour tissue,

$$p_T(r) = p_{SST} - \frac{(p_{SST} - p_{SSN})}{\mu} \times \frac{\Psi_3(r)}{(\Psi_1 + \Psi_2)} \tag{3.25}$$

(iii) In normal tissue,

$$p_N(r) = p_{SSN} + \frac{(p_{SST} - p_{SSN})}{\mu} \times \frac{\Psi_1}{(\Psi_1 + \Psi_2)} \times e^{\alpha_N(1-\mu)} \qquad (3.26)$$

It was also shown that the above solutions for different regions were identical at the interfaces where they met, by evaluating eqs. 3.25 and 3.26 for μ=1. This makes $\Psi_3(r)$ equal to Ψ_2 and the two above equations collapse to the identical expression. Fig. 3.3 shows the results for necrotic cores of size 0.5, 0.75, 0.95, and 0.99 times R. The smaller volumes of fluid sources in the tumour result in reduced pressure build-up. The effect is only significant for necrotic cores over ~90% of R for which there is a steep reduction of the tumour pressure plateau value, eventually becoming equal to the normal tissue plateau value at 100% of R. The latter case is equivalent to that of a multicellular spheroid.

The above formulation was also solved numerically using the same formulation described in section 3.0.1 for the well perfused case. The code developed could solve the problem for any necrotic core size, even zero, thus being able to solve the well perfused case too. Conservation of fluid and boundary condition continuity was verified for a number of different necrotic core sizes. All results were stable upon variation of the radial grid density and fitted very closely the analytical solution.

In the case of a radially variable S/V there is no general analytic solution as its form would heavily depend on g(r). The equation was solved numerically, again by using the method described in section 3.0.1. Fig. 3.4 shows the resulting pressure distribution from a sigmoid-S/V (eq. 3.19, D=0, A=1, B=0.5, C=10). Fig. 3.5 shows the respective result for an exponential-S/V (eq. 3.20, A=1, B=5). Both figures show that the pressure distribution is insensitive to g(r). It was found that only for very narrow g(r) profiles one gets a pressure plateau reduction similar to that of a large percentage necrotic core, as expected.

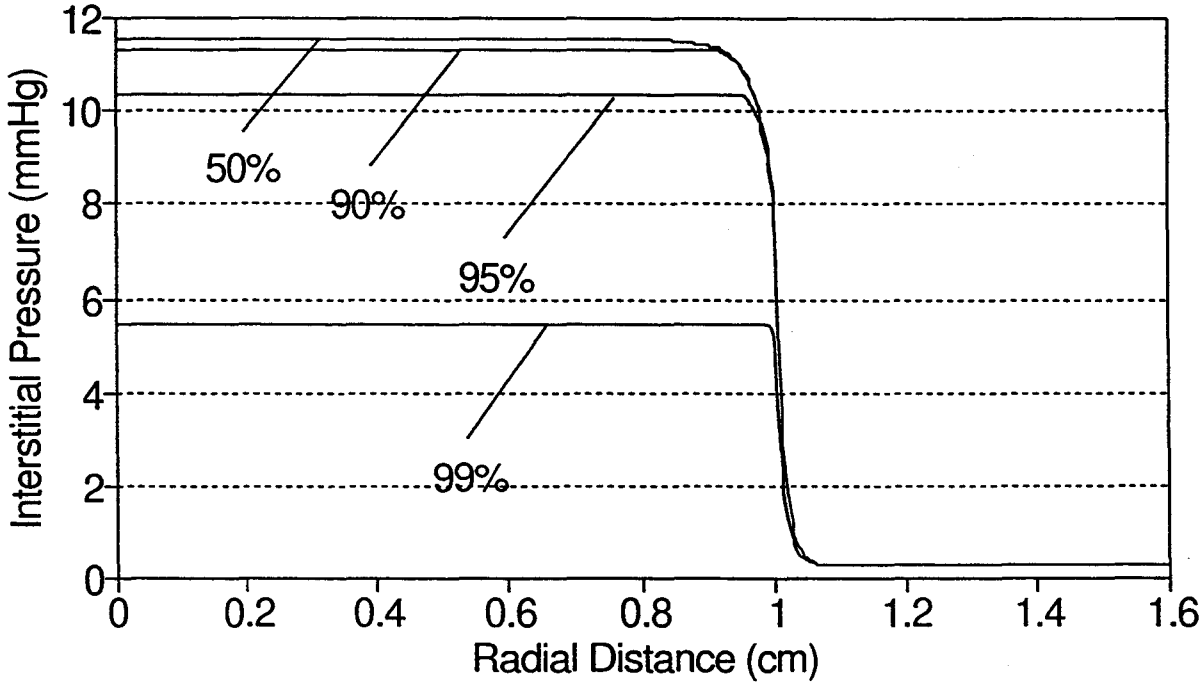

Fig. 3.3 The interstitial fluid pressure radial profile for a tumour with 50%, 75%, 95%, and 99% of its 1cm radius being necrotic.

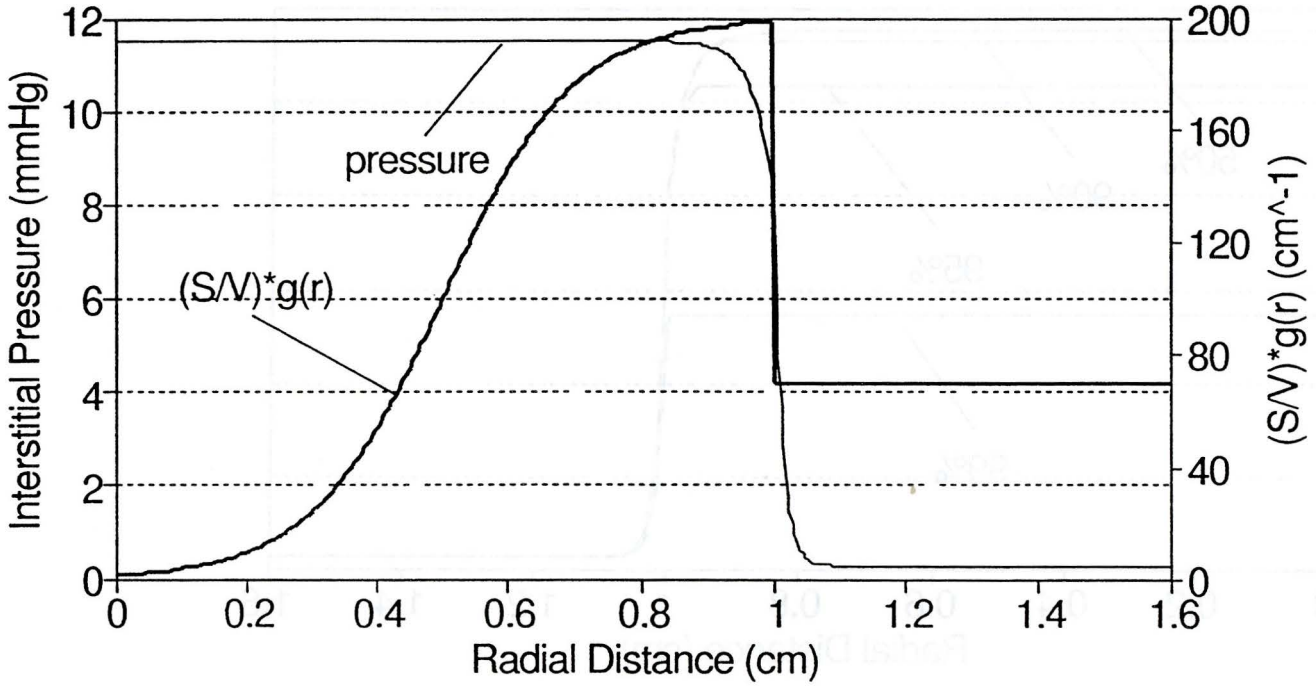

Fig. 3.4 The interstitial fluid pressure radial profile for an S(r)/V (heavy solid line) varying as a sigmoid (eq. 3.19, D=0, A=1, B=0.5, C=10).

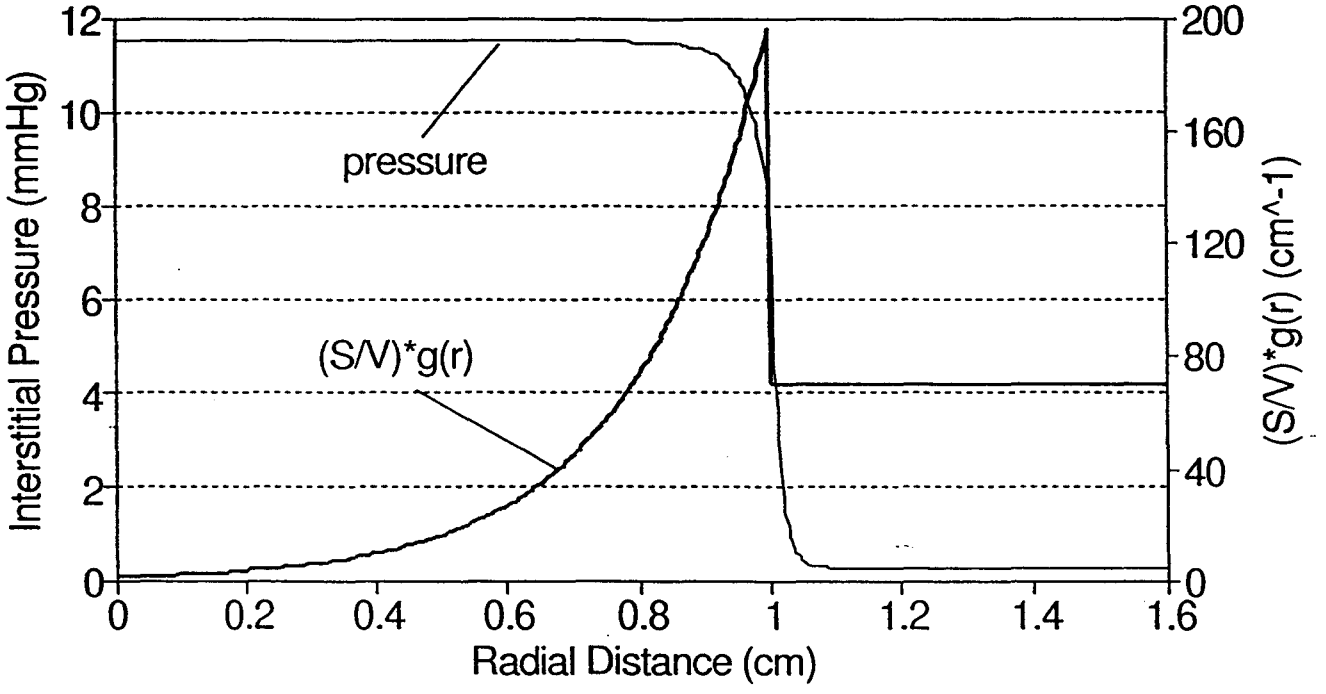

Fig. 3.5 The interstitial fluid pressure radial profile for an S(r)/V (heavy solid line) decreasing exponentially from the tumour surface (eq. 3.20, A=1, B=5).

3.2 The Interstitial Fluid Velocity Distribution

Darcy's law ,eq. (3.1), was used to calculate the resulting interstitial fluid velocity distributions from eqs. (3.24) - (3.26) for the cases of a tumour with a necrotic core, or a uniformly perfused one. The correct solution which is different from the previously proposed one (Baxter & Jain 1990) is:

(i) Inside the necrotic core,

$$u_{NC}(r) = 0 \qquad (3.27)$$

(ii) In the viable tumour tissue area,

$$u_T(r) = K_T \times \frac{(p_{SST} - p_{SSN})(1 + \alpha_N)}{\mu r} \times \frac{\Psi_4(r)}{(\Psi_1 + \Psi_2)} \qquad (3.28)$$

(iii) In the normal tissue area,

$$u_N(r) = K_N \times \frac{(p_{SST} - p_{SSN})(\alpha_N \mu + 1)e^{\alpha_N(1-\mu)}}{\mu r} \times \frac{\Psi_1}{(\Psi_1 + \Psi_2)} \qquad (3.29)$$

where

$$\Psi_4(r) = (\alpha_T^2 \mu\nu - 1)\sinh(\alpha_T[\mu - \nu]) + \alpha_T(\mu - \nu)\cosh(\alpha_T[\mu - \nu]) \qquad (3.30)$$

and $(\Psi)_1$ - $(\Psi)_3$ as defined in section 3.1.1. The solution for a uniformly perfused tumour can be found from the above by simply setting $\nu = 0$. Fig. 3.6 shows the resulting fluid velocity distributions form the pressure distributions shown in Fig. 3.3.

The fluid velocity distribution was also calculated numerically using a modified version of subroutine DSS002 (Schiesser 1991). Both the analytic and numerical solutions

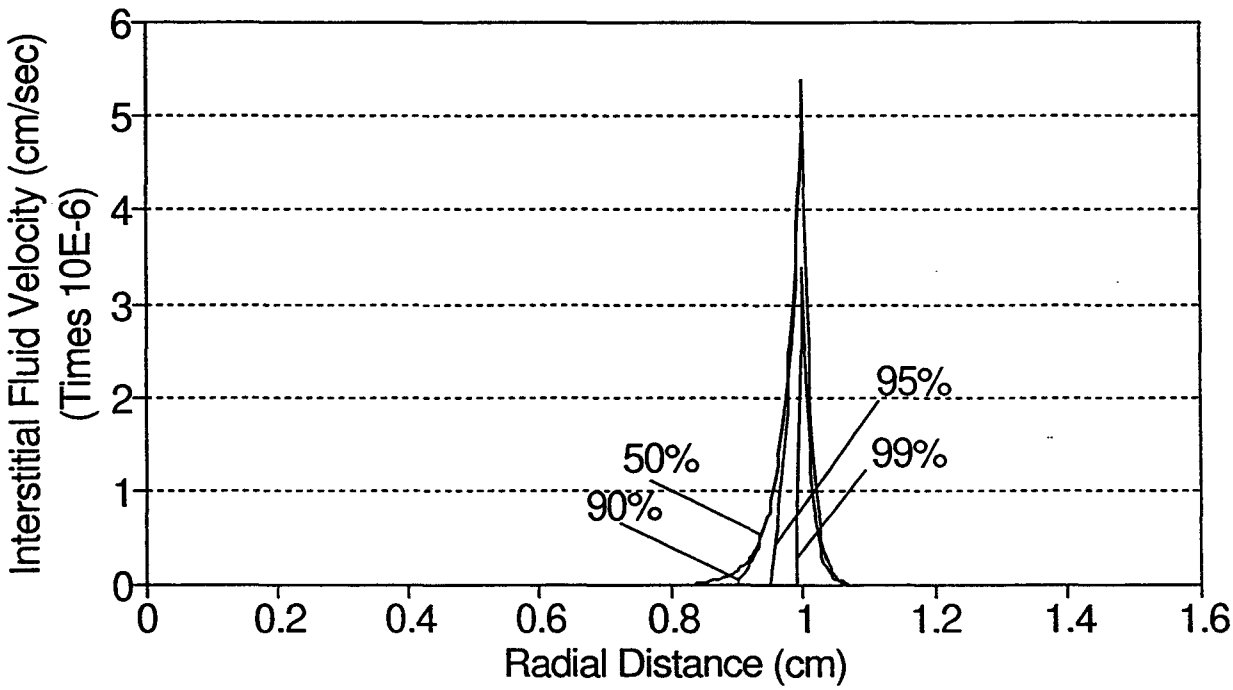

Fig. 3.6 The interstitial fluid velocity radial profiles corresponding to the pressure profiles of fig. 3.3.

of the pressure distribution were tested as input. All results matched very closely equations (3.27)-(3.29) and were stable upon variation of the radial grid spacing.

3.3 Discussion

The above results show that a fundamental problem in macromolecule delivery to the inner parts of a tumour is the pressure build-up that limits convective transport to a very narrow region near its edge. Pure diffusive macromolecule transport is very slow and perfusion is poor. In the current model local inhomogeneities are averaged out. The uniformity of perfusion overestimates the value and spatial extent of the pressure plateau as indicated by available experimental data (Jain 1987b). The total interstitial fluid extravasation rate in the tumour is predicted to be 1.046 ml/g/h without, and 0.473 ml/g/h with lymphatics in the surrounding normal tissue, all parameter values being baseline. The latter give a permeability-surface area product (PS) of 0.413 ml/g/h for the capillaries in the tumour. These values compare well with the own measured extravasation rate in SKOV3ip1 tumours (0.502±0.263 ml/g/h, section 2.0.3), or the one reported by Song (0.588 ml/g/h, 1970) for Walker 256 carcinomas subcutaneous in rat. The above may indicate that it is not essential to have a very detailed model to estimate the total fluid extravasation rate in tumours.

The size of a well-perfused tumour is important in determining the pressure plateau value only for tumour radii less than 0.2 cm where the plateau pressure will be significantly less than p_e (eq. 3.8), as can be seen in fig. 3.7. The latter shows how the pressure averaged over the whole tumour varies with its radius. As $R \rightarrow 0$, the average pressure approaches the healthy tissue one as required by eq. 3.11. As previously reported (Jain & Baxter 1989a), the larger the tumour, or the larger the source term, the steeper the pressure profile becomes at its edge thus further reducing the size of the area of convective transport. It was found that an increase in L_p, S/V ,or p_v, or a decrease in σ_T, or K increased the pressure build-up in a way similar to that of increasing R. However, these latter changes also increase the net transcapillary fluid flux thus creating two competing factors in macromolecule delivery.

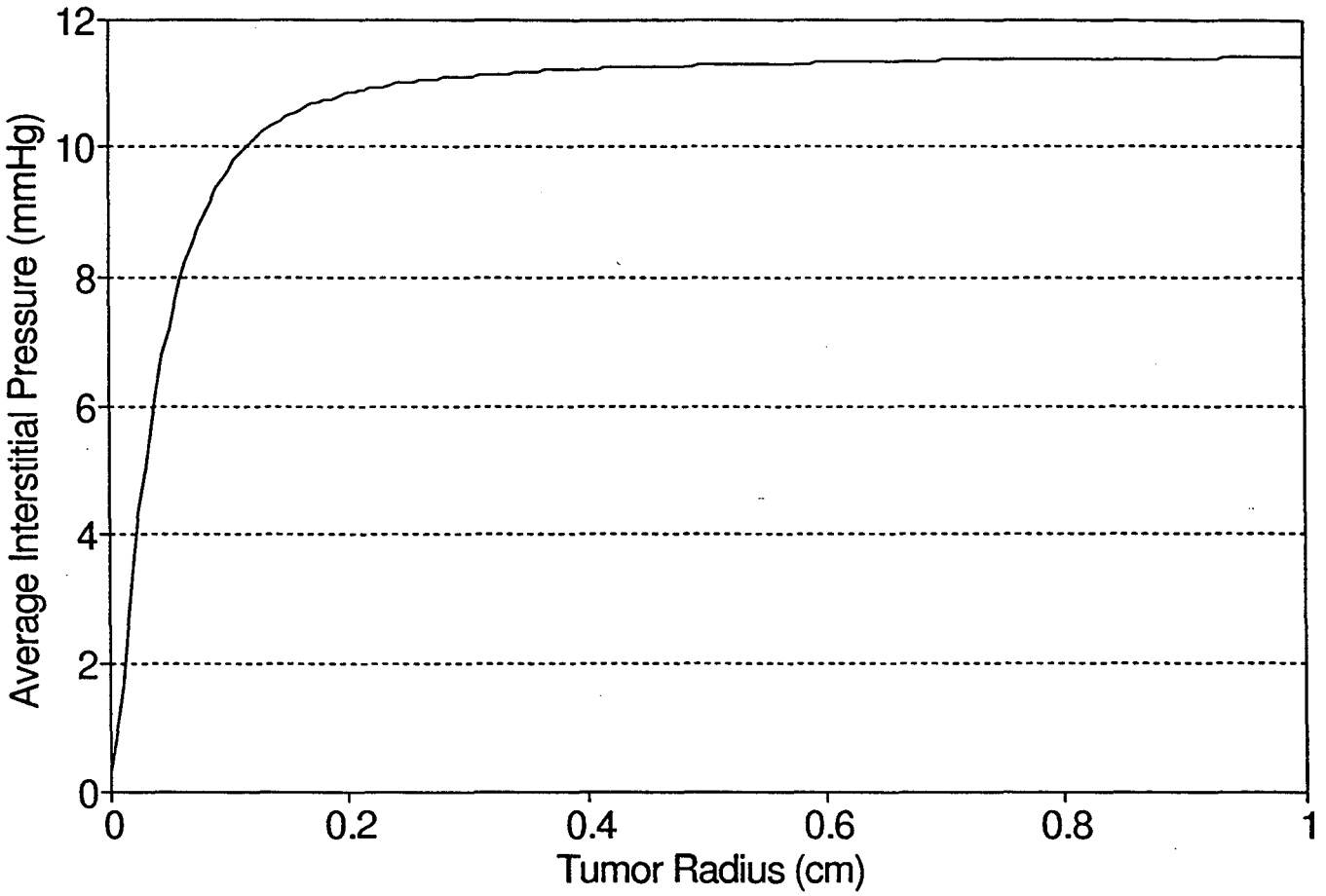

Fig. 3.7 The average interstitial pressure in a tumour as a function of its radius.

Fig. 3.8 shows the variation of the average interstitial fluid velocity with tumour size. For small tumour radii the low pressure build-up (fig. 3.7) favours an increase in convective velocity. For larger radii, the increasing percentage volume at plateau pressure monotonically lowers the average. This would be the case for tumours in which rapid angiogenesis keeps them well perfused while they grow, as with the SKOV3ip1. There are currently no data available on how the necrotic core as a fraction of the total radius varies with tumour size. The former is a quantity strongly dependent on the cancer cell line. However, it is a reasonable guess that in real tumours the scattered necrotic areas, and the inhomogeneity of perfusion would reduce the slope of approach and value of the interstitial pressure plateau, as well as the velocity profiles w.r.t. what is predicted in figs. 3.7 and 3.8. The pressure value at the centre of the tumour remains constant and equal to p_e (11.5 mmHg for the particular choice of baseline parameters) for all possible tumour radius values except for zero, which is not in agreement with reported experimental data (Jain 1987). The convective velocity at the edge monotonically increases with tumour size as the pressure profile becomes ever steeper.

As it will be shown in chapter 4, the macromolecule perfusion is further limited by clearance of the macromolecule from blood circulation with time, or in the case of continuous infusion, by non-specific binding and the resulting systemic toxicity. Hence, there may be areas of cancer cells not near the tumour surface that are in a dormant state, starting to proliferate when the ones near the surface have been killed because of good perfusion there, rendering the therapy ineffective. Therefore, once an interstitial fluid transport model has been established it is worthwhile to investigate how a change in transport parameters affects the spatial and temporal distributions of the injected macromolecules in order to increase the uniformity of perfusion.

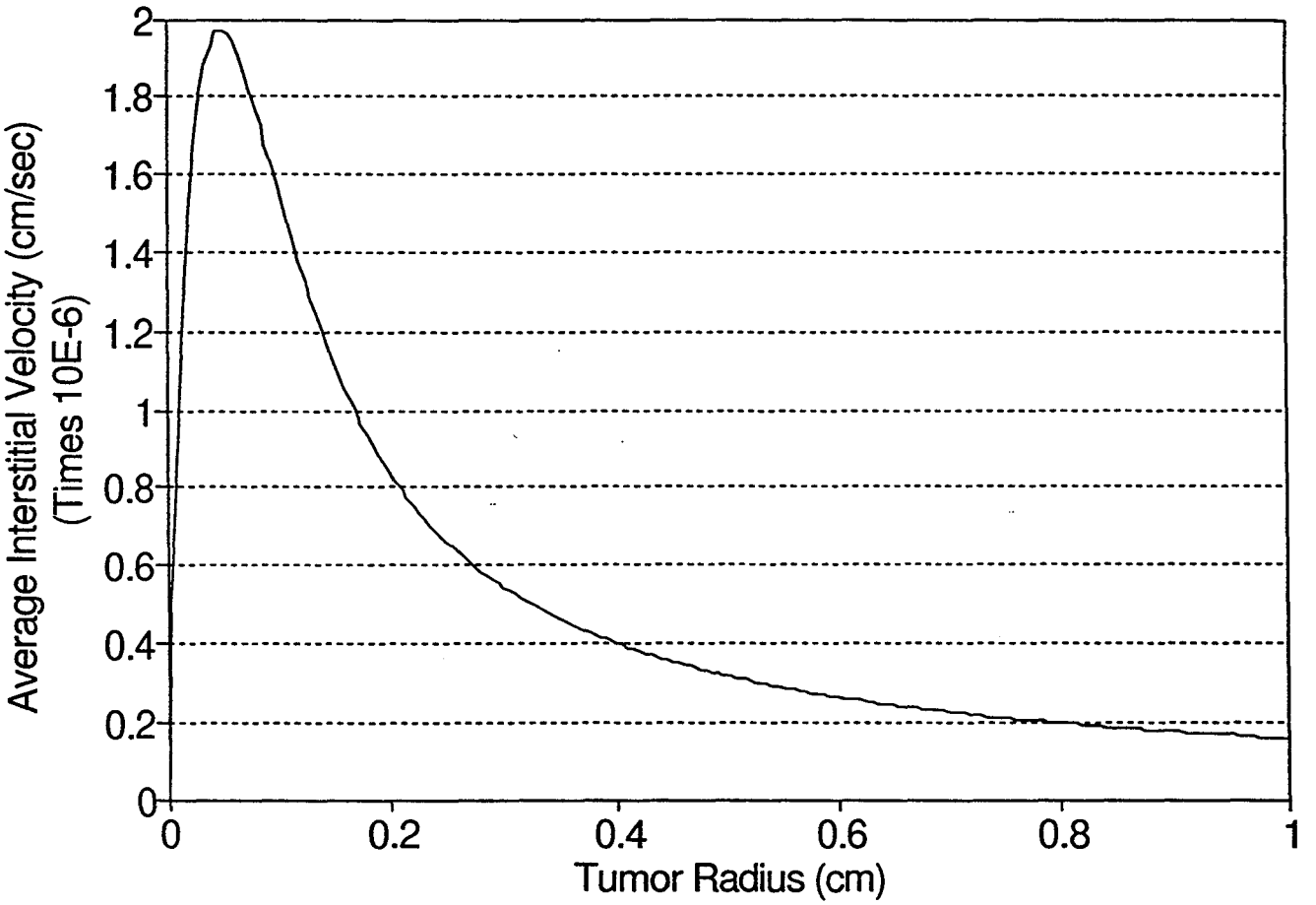

Fig. 3.8 The average interstitial fluid velocity in a tumour as a function of its radius.

4. A Mathematical Model for the Spatial and Temporal Macromolecule Distributions in Tumours

This chapter tackles the delivery aspect of IgG, $F(ab')_2$, and Fab/Fab' macromolecules in tumours. A model proposed by Baxter & Jain (1989,1990,1991a) has been solved by the numerical method of lines (Schiesser 1991). The cases of non-binding and binding macromolecule were studied separately. The model was expanded to include the radial variation of surface area for transcapillary exchange per unit volume. The relative importance of a number of physiological parameters in optimizing delivery was investigated and the model's limitations are discussed.

4.0 A Solute Transport Model for Non-Binding Macromolecules in a Spherical Well Perfused Tumour, or One Having a Necrotic Core

In the model previously reported by Baxter & Jain (1989) non-binding macromolecule interstitial transport is described by the convective-diffusion equation:

$$\frac{\partial C_i}{\partial t} + \nabla \cdot (r_F u_i C_i) = \nabla \cdot (D \nabla C_i) + \phi_S(r) \qquad (4.1)$$

where,

C_i = Interstitial free macromolecule concentration (M)

t = Time (sec)

D = Diffusion coefficient ($\times 10^{-8}$ cm^2/sec) (Gerlowski & Jain 1986)

Tumour:

IgG= 1.3, $F(ab')_2$= 2.0, Fab= 4.4

Normal Tissue:

IgG= 0.048, $F(ab')_2$= 0.16, Fab= 1.2

u_i = Interstitial fluid velocity, +ve in the radially outward direction, as determined in section 3.0.1 (cm/sec)

r_F = Retardation factor, the ratio of solute to fluid velocities, set to unity (Swabb *et al.* 1974)

$\phi_S(r)$ = Distributed solute source term using a single pore model (Kedem & Katchalsky 1958, Patlak *et al.* 1963, Curry 1984, Dean 1987) (M-sec)

Assuming radial symmetry in the source term and no spatial variation in the diffusion coefficient, eq. (4.1) can be re-written as:

$$\frac{\partial C_i}{\partial t} + \frac{1}{r^2}\frac{\partial (r^2 u_i C_i)}{\partial r} = D\frac{1}{r^2}\frac{\partial}{\partial r}\left(r^2\frac{\partial C_i}{\partial r}\right) + \phi_S(r) \qquad (4.2)$$

The solute transcapillary transport term, adapted from the expression for a bicomponent solution consisting of a solvent and a single neutral solute through a porous membrane as derived by Patlak *et al.* (1963) is written as:

$$\phi_S(r) = \frac{J_S}{V} - \frac{J_V}{V}C_i = \frac{J_V(1-\sigma)}{V}\cdot\frac{C_p e^{Pe_V} - C_i}{e^{Pe_V} - 1} - \frac{J_L}{V}C_i \qquad (4.3)$$

where $Pe_V = J_V(1-\sigma)/PS$ defined as an effective Peclet Number, the ratio of convective to diffusive flux across the capillary wall. All parameters appearing in eqs. 4.2 and 4.3 are as defined in section 3.0 with the addition of:

J_S/V = Solute mass extravasated per unit time, per unit volume of tumour tissue ($M \cdot sec^{-1} \cdot cm^3$)

P = Effective vascular diffusive permeability coefficient (cm/sec) (Gerlowski & Jain 1986)

Tumour:

IgG= 5.73, $F(ab')_2$= 17.3, Fab= 149

Normal Tissue:

IgG= 0.73, $F(ab')_2$= 2.2, Fab= 19.1

C_p = Macromolecule plasma concentration (M)

Constant infusion: = C_p^o

Bolus injection: $= C_p^o(\alpha_1 \exp(-\lambda_1 t) + \alpha_2 \exp(-\lambda_2 t))$ (4.4)

Both tumour and normal tissue: $C_p^o = 10^{-9}$ M for all macromolecule types. The actual M value for each macromolecule type is not important as all concentrations were normalized w.r.t. the initial plasma concentration. The pharmacokinetic parameters corresponding to eq. 4.4 for a bolus injection were assumed as follows (Fujimori 1989):

IgG : $\alpha_1 = 0.27$, $\alpha_2 = 0.73$, $\lambda_1 = 1.9\times10^{-4}$, $\lambda_2 = 7.4\times10^{-6}$ s^{-1}

$F(ab')_2$: $\alpha_1 = 0.61$, $\alpha_2 = 0.39$, $\lambda_1 = 1.5\times10^{-4}$, $\lambda_2 = 6.3\times10^{-6}$ s^{-1}

Fab : $\alpha_1 = 0.68$, $\alpha_2 = 0.32$, $\lambda_1 = 2.4\times10^{-4}$, $\lambda_2 = 9.9\times10^{-6}$ s^{-1}

σ = Macromolecule osmotic reflection coefficient (Covel *et al.* 1986)

Both tumour and normal tissue:

IgG= 0.95, $F(ab')_2$= 0.90, Fab= 0.50

Eq. 4.2 is subject to the following boundary conditions:

(i) No solute flux due to radial symmetry at the centre of the tumour

$$- D\left.\frac{\partial C_i}{\partial r}\right|_{r=0} + (u_i C_i)|_{r=0} = 0 \qquad (4.5)$$

(ii) Continuity of solute concentration at the tumour - normal tissue interface

$$C_i\,|_{r=R} = C_i\,|_{r=R'} \qquad (4.6)$$

(iii) Continuity of solute flux at the tumour - normal tissue interface

$$-D_T\left.\frac{\partial C_i}{\partial r}\right|_{r=R} + (u_i C_i)|_{r=R} = -D_N\left.\frac{\partial C_i}{\partial r}\right|_{r=R'} + (u_i C_i)|_{r=R'} \qquad (4.7)$$

In the case of a tumour having a fraction of its radius necrotic, but being well perfused in the viable tumour tissue area the above formulation holds with the following

additional conditions (Baxter & Jain 1990):

(i) Continuity of solute concentration at the necrotic core - viable tumour interface

$$C_i\big|_{r=R_n^-} = C_i\big|_{r=R_n^+} \qquad (4.8)$$

(ii) Continuity of solute flux at the necrotic core - viable tumour interface

$$-D_T \left.\frac{\partial C_i}{\partial r}\right|_{r=R_n^-} + (u_i C_i)\big|_{r=R_n^-} = -D_T \left.\frac{\partial C_i}{\partial r}\right|_{r=R_n^+} + (u_i C_i)\big|_{r=R_n^+} \qquad (4.9)$$

where it is assumed that the diffusion coefficient of the macromolecules in necrotic tissue is the same as that of the viable tumour tissue.

(iii) Since there are no blood vessels in the necrotic area the solute source term is set to zero in that area:

$$\phi_S(r) = 0 \quad , \quad r<R_n \qquad (4.10)$$

4.0.1 The Numerical Solution of the Macromolecule Transcapillary Transport Equation for Non-Binding Macromolecule

A FORTRAN 77 code was written to solve eqs. 4.2 to 4.9. It incorporated subroutine LSODE (Hindmarsh) which is a solver for ordinary differential equations of the form:

$$\frac{\partial y(i)}{\partial t} = f(i,y(1)...,y(neq)) \qquad (i=1,...,neq) \qquad (4.11)$$

where neq is the number of coupled differential equations to be solved. The equations are represented in a semi-discretized form treating time as a continuous independent

variable. A brief description of the code is given here:

(i) The main program defines all the physiological parameters defined above, the spatial discretization to be used, the initial conditions, and the RAM workspace needed. It also calls subroutine LSODE which solves the system and performs integration of y(i) over time, and formats the output files. The solver option for stiff systems was used. To carry out integration with time, after every successful return, LSODE was called on the next output time point t_{out} that the solution was desired.

(ii) A subroutine of the form **f**(neq,t,y,∂y/∂t) is called which supplies the vector function **f**. All physiological parameters are passed to this subroutine through the use of labelled common blocks. The set of equations resulting from the spatial discretization of eqs. 4.2 to 4.9 is defined here. First order finite differences were used. The discretized macromolecule transport equation at the first grid point including the no-flux condition (eq. 4.5) was:

$$\frac{dC(1)}{dt} = P\,Pe_v(1)\,\frac{S(1)}{V}\cdot\frac{(C_p{}^{o}\,(\alpha_1 e^{-\lambda_1 t} + \alpha_2 e^{-\lambda_2 t})e^{Pe_v(1)} - C(1))}{e^{Pe_v(1)} - 1} \tag{4.12}$$

At the *ith* grid point the discretized equation was:

$$\frac{dC(i)}{dt} = D\frac{(C(i+1) - C(i-1))}{(i-1)\,\delta r^2} + \frac{(C(i+1) - 2C(i) + C(i-1))}{\delta r^2}$$

$$- \frac{2u(i)C(i)}{(i-1)\,\delta r} - \frac{(u(i+1) - u(i))C(i)}{\delta r} - \frac{u(i)(C(i+1) - C(i))}{\delta r}$$

$$+ P\,Pe_v(i)\,\frac{S(i)}{V}\cdot\frac{(C_p{}^{o}(\alpha_1 e^{-\lambda_1 t} + \alpha_2 e^{-\lambda_2 t})e^{Pe_v(i)} - C(i))}{e^{Pe_v(i)} - 1} - L_{pL}(p(i) - p_L)C(i) \tag{4.13}$$

where $Pe_V(i) = L_p (p_{SST} - p(i)) (1 - \sigma)/ P$ for i=1,...,N (4.14)

N is the number of discrete points in which the tumour continium was divided. If the resulting N-1 discretization intervals is small enough, the C(i) value in them can be assumed constant. In normal tissue the form of the discrete equations remained the same, but the physiological parameters were changed to the normal tissue ones shown in section 4.0. Boundary conditions 4.6 to 4.9 were applied accordingly at the necrotic core - viable tumour and viable tumour-normal tissue interfaces. At all points in the tumour with no net pressure difference across the vasculature, J_V/V was zero, and so the source term was also zero. The resulting matrix had tridiagonal form, as explained in section 1 1, and so the half-bandwidth parameters required by LSODE were set to unity The vector function **f** was adjusted to include the necrotic core case by including no source term in discretized equations describing macromolecule transport in that region.

(iii) The Jacobian of the system was not provided externally, and so, a solver option was chosen where it is being generated internally by difference quotients.

In all the above, only non-zero matrix elements needed be loaded. The solute concentration profiles were slightly unstable to variations of the radial grid step size (see section 4.3, part 1). Fig. 4.1 shows the radial variation of the free IgG (m.w 150kD) concentration normalized w.r.t. the plasma concentration (C_p^o) for continuous infusion. The tumour radius was assumed to be 1cm. Fig. 4.2 shows the respective results for the Fab fragment (m.w 50kD). Results were also obtained for the $F(ab')_2$ fragment (m.w 100kD), but are not shown here. Because of its molecular weight, its behaviour characteristics fall between those of IgG and Fab. This holds true for everything to be mentioned below Figs. 4.3 and 4.4 show the radial variation of the IgG and Fab profiles respectively, when the plasma concentration followed bi-exponential clearance rates (eq. 4.4). Fig. 4.5 shows the free IgG radial profile after a 24hr constant perfusion for a tumour with 50%, 75%, 95%, and 100% of its 1cm radius being necrotic. The very last case is equivalent to that of a multicellular spheroid imbedded in healthy, well perfused tissue. Fig. 4.6 shows the respective results for the Fab fragment. It can be seen that because of the smaller size and molecular weight of the Fab fragment a larger quantity of it extravasates near the periphery, and more of it diffuses deeper into the necrotic core

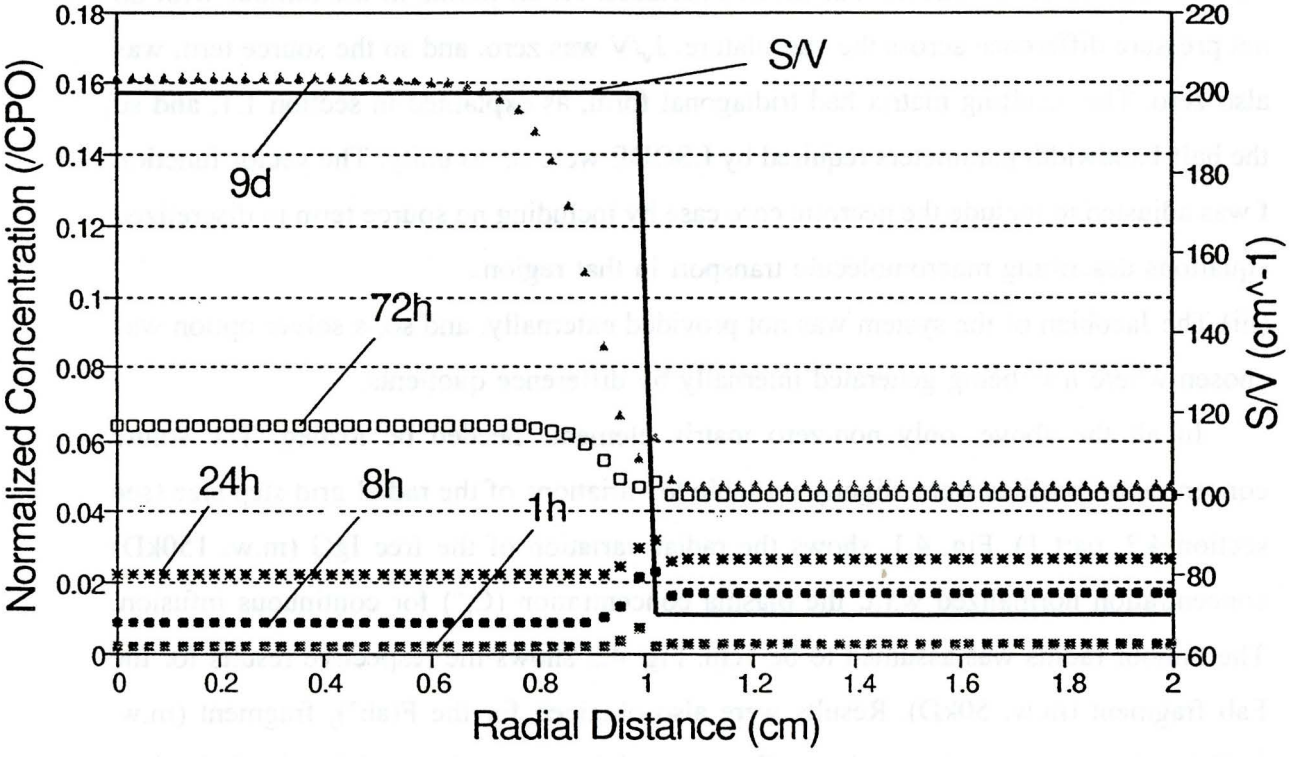

Fig. 4.1 The radial variation in a R=1cm tumour of the dimensionless free IgG concentration at 1h (light-filled squares), 8h (dark-filled squares), 24h (asterisks), 72h (empty squares), 9d (light-filled triangles) for constant perfusion.

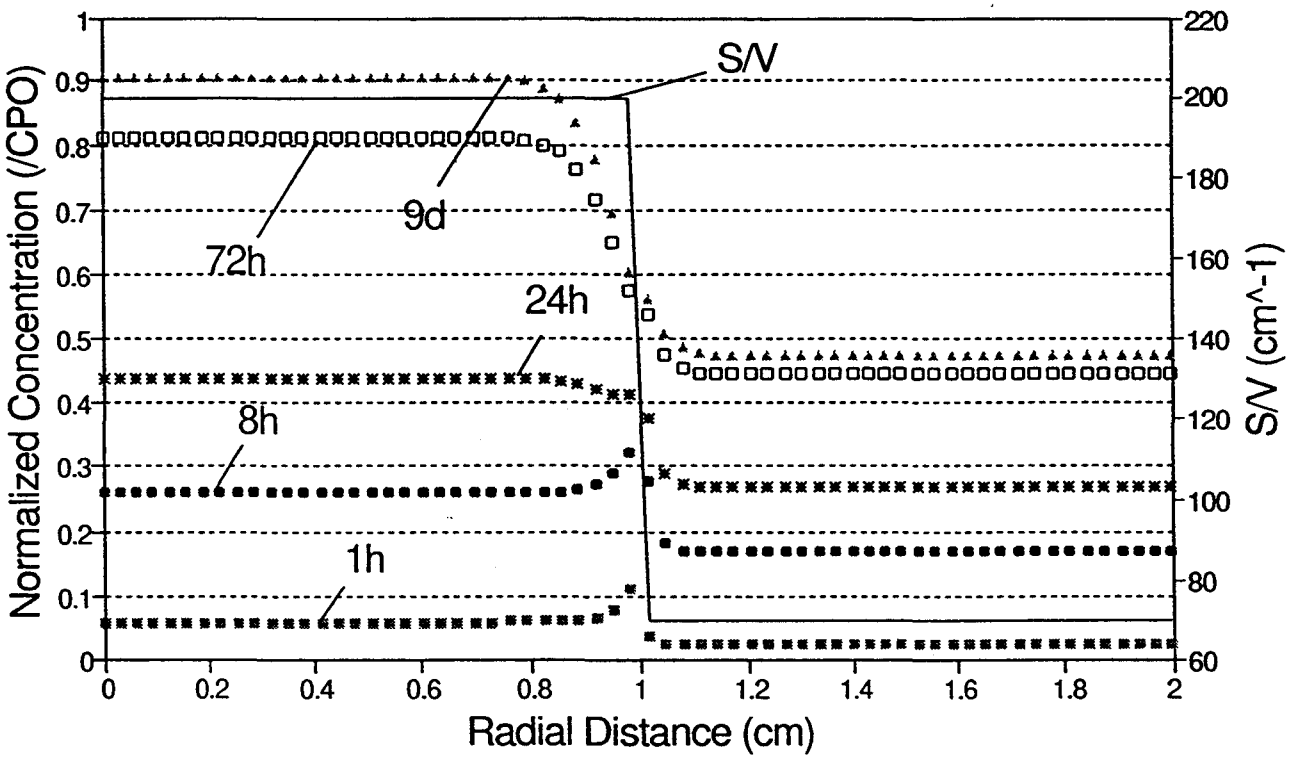

Fig. 4.2 The radial variation in a R=1cm tumour of the dimensionless free Fab fragment concentration at 1h (light-filled squares), 8h (dark-filled squares), 24h (asterisks), 72h (empty squares), 9d (light-filled triangles) for constant perfusion.

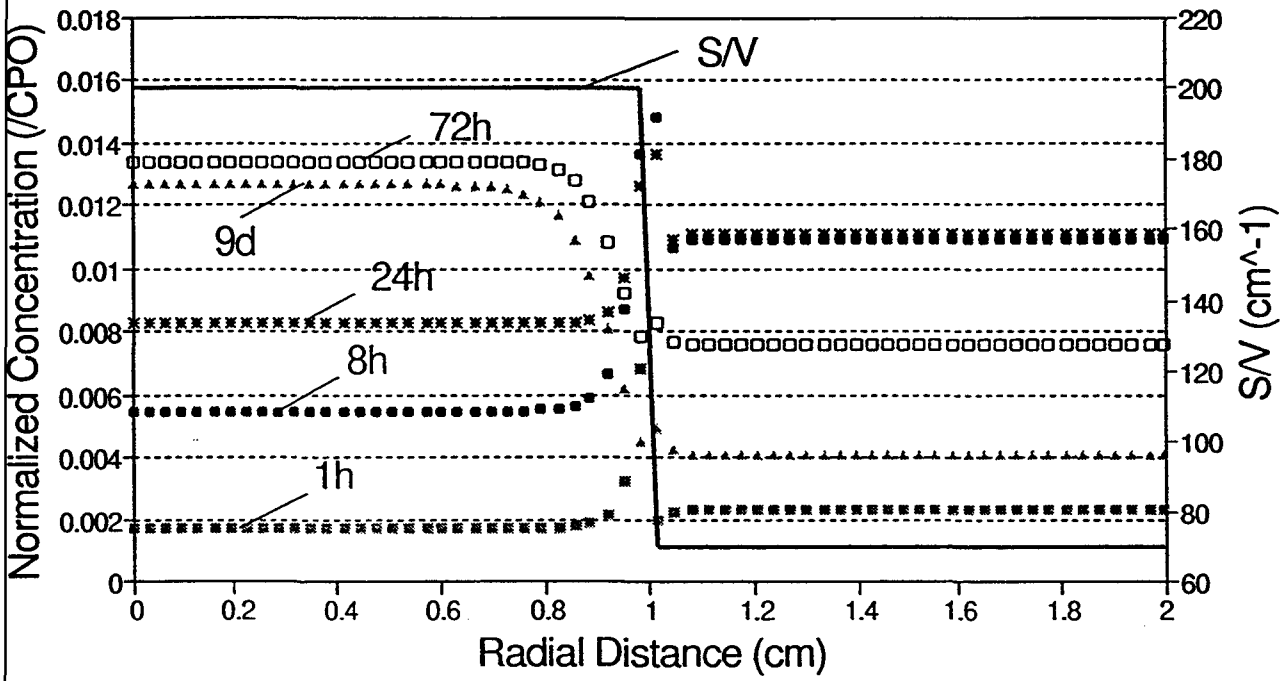

Fig. 4.3 The radial variation in a R=1cm tumour of the dimensionless free IgG concentration at 1h (light-filled squares), 8h (dark-filled squares), 24h (asterisks), 72h (empty squares), 9d (light-filled triangles) after a single bolus i.v. injection at t=0 (see eq. 4.4).

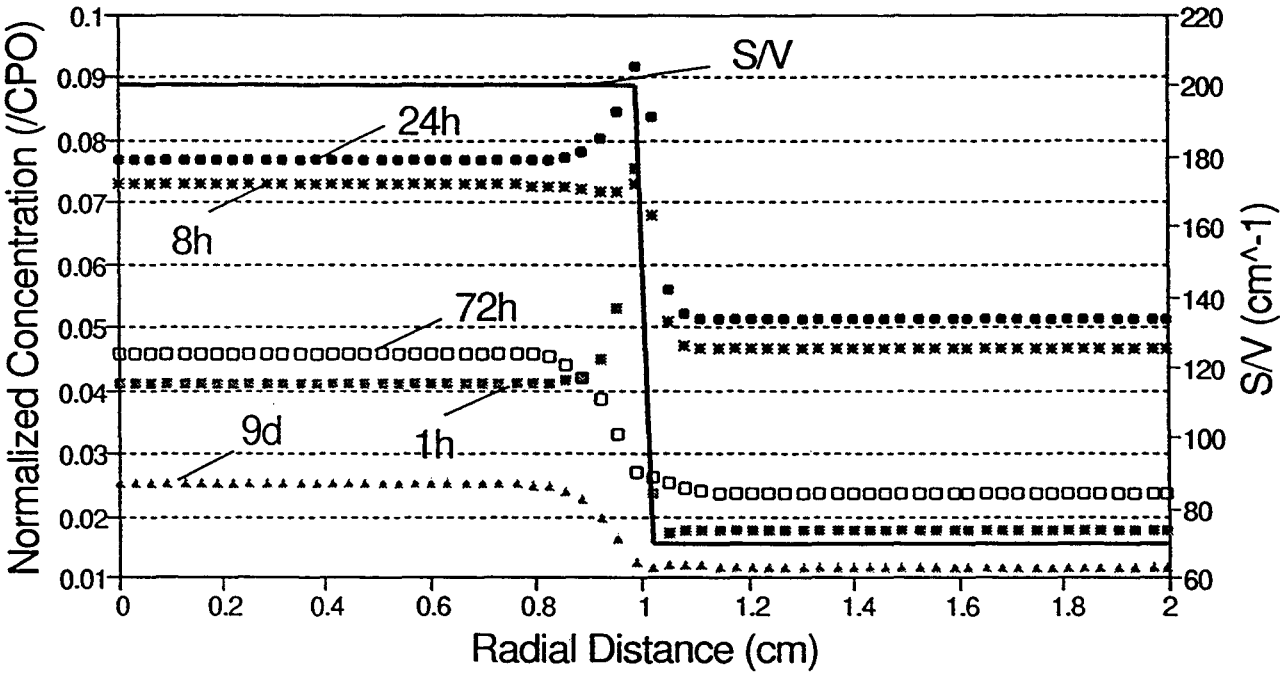

Fig. 4.4 The radial variation in a R=1cm tumour of the dimensionless free Fab fragment concentration at 1h (light-filled squares), 8h (dark-filled squares), 24h (asterisks), 72h (empty squares), 9d (light-filled triangles) after a single bolus i.v. injection at t=0 (see eq. 4.4).

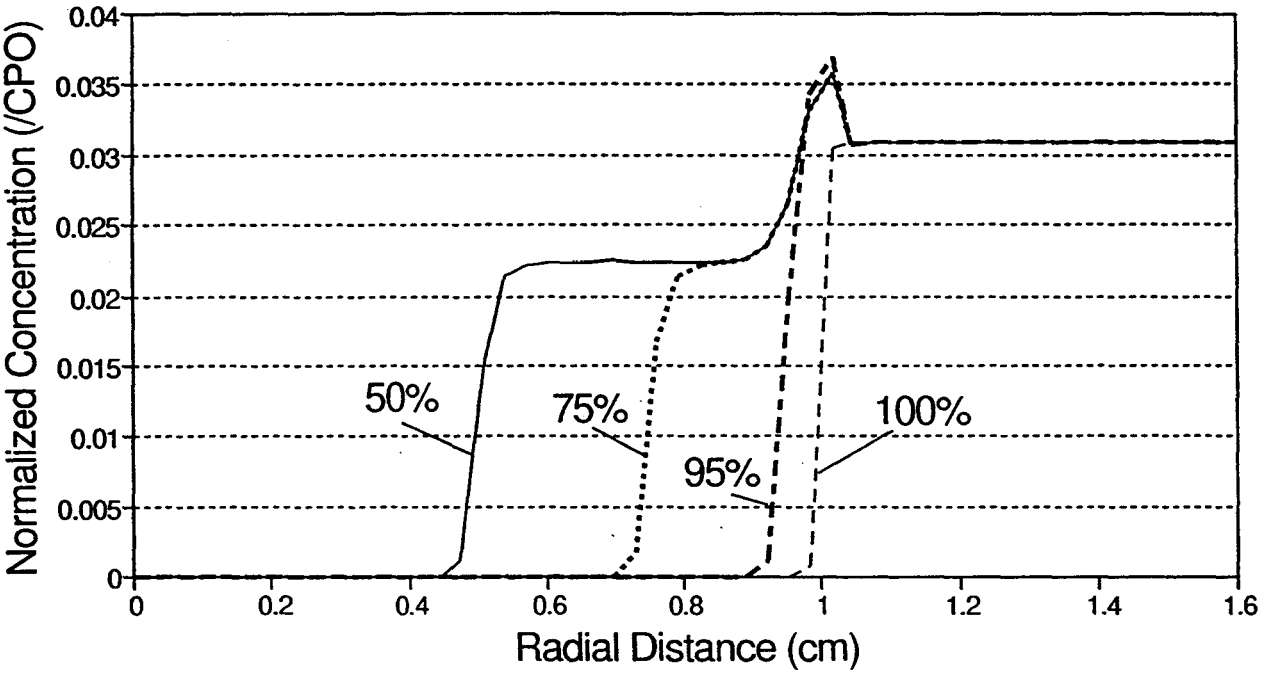

Fig. 4.5 The radial variation of the dimensionless free IgG concentration after a 24hr constant perfusion in a R=1cm tumour having 50% (solid line), 75% (dotted line), 95% (centered line), and 100% (dashed line) of its radius being necrotic.

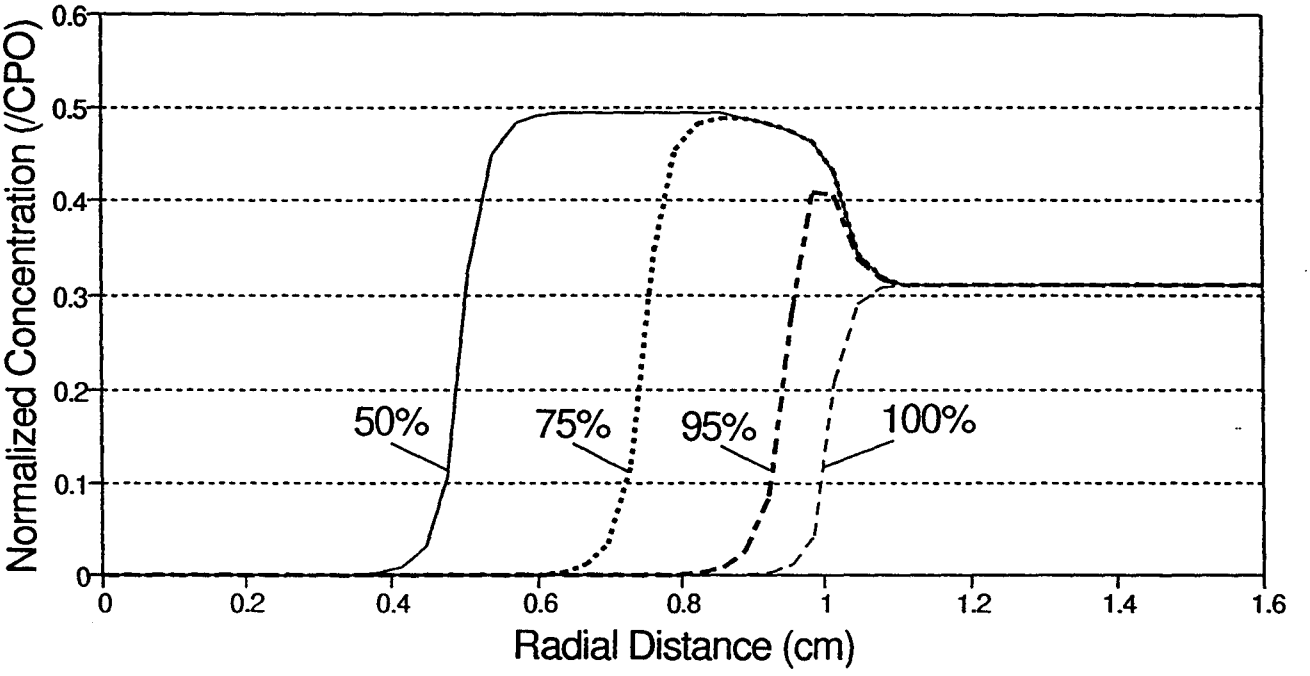

Fig. 4.6 The radial variation of the dimensionless free Fab fragment concentration after a 24hr constant perfusion in a R=1cm tumour having 50% (solid line), 75% (dotted line), 95% (centered line), and 100% (dashed line) of its radius being necrotic.

area for the same duration of constant perfusion.

4.1 A Solute Transport Model for Binding Macromolecules in the Presence of Metabolism for a Spherical Well Perfused Tumour, or one Having a Necrotic Core

In the model previously reported by Baxter & Jain (1991a) the binding macromolecule interstitial transport in the presence of metabolism is described by the following two coupled equations:

$$\frac{\partial C_i}{\partial t} = D\frac{1}{r^2}\frac{\partial}{\partial r}\left(r^2\frac{\partial C_i}{\partial r}\right) - \frac{1}{r^2}\frac{\partial(r^2 u_i C_i)}{\partial r} + \phi_S - k_f C_i(B_{max} - B_i) + k_r B_i \qquad (4.15)$$

$$\frac{\partial B_i}{\partial t} = k_f C_i(B_{max} - B_i) - k_r B_i - k_e B_i \qquad (4.16)$$

where C_i, t, D, u_i, and $\phi_S(r)$ (eq. 4.3) are as defined in section 4.0 above. Also, from Baxter & Jain (1991a):

B_i = Interstitial concentration for bound macromolecule (M)

B_{max}= Concentration of bound macromolecule at saturation of binding sites (M)

1.175×10^{-8} for IgG and $F(ab')_2$ in tumour

2.35×10^{-8} for Fab in tumour

For all macromolecule types (upper limit estimates):

B_{max}(normal tissue) = $10^{-1} \times B_{max}$ (tumour)

B_{max}(necrotic core) = $10^{-1} \times B_{max}$ (tumour)

k_f = Association rate constant (M^{-1} sec^{-1})

4.333×10^4 for IgG and $F(ab')_2$ in tumour

1.333×10^4 for Fab in tumour

For all macromolecule types:

k_f(normal tissue) = 10^{-3} × k_f (tumour)

k_f(necrotic core) = 10^{-3} × k_f (tumour)

k_r = Dissociation rate constant (sec^{-1})

1.417×10^{-4} for IgG and $F(ab')_2$ in tumour

1.517×10^{-4} for Fab in tumour

For all macromolecule types:

k_r(normal tissue) = 10^{-3} × k_r (tumour)

k_r(necrotic core) = 10^{-3} × k_r (tumour)

k_e = Metabolism rate constant (sec^{-1})

2.167×10^{-5} for IgG, $F(ab')_2$, and Fab

For all macromolecule types it was assumed that:

k_e(normal tissue) = 10^{-1} × k_e (tumour)

k_e(necrotic core) = 0

In the above, radial symmetry has been assumed for the source term, and D, k_r, k_r, k_e for all macromolecule types are assumed spatially invariant. The difference in the magnitude of k_f between IgG and Fab is partly attributed to their valence difference. Intact IgG has two heavy-light chain complexes whereas Fab has only one. Hence, to a first crude approximation the IgG interaction should be bivalent and that of Fab monovalent. The effect of valency is incorporated in the value of k_f. Fujimori *et al.* (1989) assumed a similar magnitude difference in k_f for these two macromolecules.

Boundary conditions 4.5 to 4.9 apply here. In the case where the tumour has a necrotic core condition 4.10 holds too.

4.1.1 The Numerical Solution of the Macromolecule Transcapillary Transport Equations for Binding Macromolecule in the Presence of Metabolism

A FORTRAN 77 code was written to solve eqs. 4.12 and 4.13 subject to conditions 4.5 to 4.10. The subroutine used to solve the above equations was LSOIBT (Hindmarsh 1983). It solves the initial value problem for linearly implicit systems of first order ordinary differential equations of the form:

$$\boldsymbol{a}(t,\mathbf{y}) \times \frac{\partial \mathbf{y}}{\partial t} = \boldsymbol{g}(t,\mathbf{y}) \qquad (4.17)$$

where **a**(t,**y**) is a square matrix. Eqs. 4.16 are the semi-discretized form of eqs. 4.14 and (3.39). A brief description of the code is given here:

(i) The main program is defined in a manner similar to paragraph (i) of section 4.0.1, this time the main calling subroutine being LSOIBT. The program is versatile in that it can evaluate results for a wide range of physiological parameters (e.g. necrotic core size, macromolecule type) with minor adjustments. It can also produce results for all three macromolecule types in one run. Sets of loops were included that calculate an index of spatial non-uniformity (ISN) of S/V, the free, bound, and total macromolecule distributions. It was defined as (Fujimori *et al.* 1990):

$$ISN = \frac{\sqrt{\sum_{j=1}^{N} (y_j - \bar{y})^2}}{\bar{y}\sqrt{N(N-1)}} \qquad (4.18)$$

where N is equal to the number of radial grid points assumed in the spatial discretization of eqs. 4.12 and 4.13, y_j is the value of the parameter of interest at the jth grid point, and $\bar{y}$ is the average value of that parameter over the whole tumour volume. Another loop calculates the concentration at the centre of the tumour as a percentage of the average.

(ii) A subroutine of the form **res**(neq,t,**y**,**s**,**r**) is called where the residual matrix

$$\mathbf{r} = \mathbf{g}(t,\mathbf{y}) - \mathbf{a}(t,\mathbf{y}) \times \mathbf{s} \qquad (4.19)$$

was calculated. In this particular case,the **g** matrix contains the discretized form of the right-hand-side of eqs. (4.12) and (4.13), and **a** is a diagonal matrix defining the non-zero elements of **s**, which is an internally generated approximation to $\partial \mathbf{y}/\partial t$. For the discretized form of equations 4.14 and 4.15, **a** is a matrix with non-zero elements only along its main diagonal. The latter are all equal to unity except for the zero ones at the tumour center

and at interfaces where boundary conditions apply. The residual matrix is a block-diagonal one as described in section 1.1. Its bandwidth parameters are defined below in (iii). The discretized free macromolecule ttransport equation in the first block is the no-flux condition at the center (eq. 4.5). The form of the discretized bound macromolecule equation has the same form for all grid points.

$$r(1,1) = -D\frac{C(1,2) - C(1,1)}{\delta r} + u(1)C(1,1) \tag{4.20}$$

$$r(2,1) = k_f C(1,1)(B_{max} - C(2,1)) - k_r C(2,1) - k_c C(2,1) - s(2,1) \tag{4.21}$$

The first index refers to the type of macromolecule concentration. 1 refers to the free concentration and 2 to the bound one. The second index refers to the discrete point in space where that concentration is evaluated by LSOIBT.

The equations for free and bound macromolecule in the i*th* block were:

$$r(1,i) = D\frac{C(1,i+1) - C(1,i-1)}{(i-1)\,\delta r^2} + \frac{C(1,i+1) - 2C(1,i) + C(1,i-1)}{\delta r^2}$$

$$- \frac{2u(i)C(1,i)}{(i-1)\,\delta r} - \frac{(u(i+1) - u(i))C(1,i)}{\delta r} - \frac{u(i)(C(1,i+1) - C(1,i))}{\delta r}$$

$$+ P\,Pe_V \frac{S(i)}{V} \cdot \frac{(C_p^{\,o}(\alpha_1 e^{-\lambda_1 t} + \alpha_2 e^{-\lambda_2 t})e^{Pe_1(i)} - C(1,i))}{e^{Pe_1(i)} - 1} - L_{pL}(p(i) - p_L)C(1,i)$$

$$- k_f C(1,i)(B_{max} - C(2,i)) + k_r C(2,i) - s(1,i) \tag{4.22}$$

$$r(2,i) = k_f C(1,i)(B_{max} - C(2,1)) - k_r C(2,i) - k_c C(2,i) - s(2,i) \quad (4.23)$$

The FORTRAN code for the **res** subroutine includes loops for the case of an arbitrary size necrotic core. The macromolecule binding parameters and the lack of the source term $\phi_S(r)$ (eq. 4.3) are automatically adjusted for the specified necrotic core radius. The physiological parameters were changed appropriately for the normal tissue area and the relevant boundary conditions (eq. 4.5 to 4.9) defined the interface discretized equations. (iii) The block structure of the matrices **a**(t,**y**) and **dr/dy**, which is internally generated by LSOIBT, are identified. The latter must deal internally with a linear combination, **p**, of the two. The matrix **p** has a block-tridiagonal form with fixed structure parameters, defined by the form of the discretized equations in (ii) above:

mb= block size, mb≥1, and

nb= number of blocks, nb≥4

with mb×nb= neq. When solving eqs. 4.14 and 4.15 mb=2, nb=6300, and neq= 12600 were chosen, as they provided fine enough spatial discretization intervals to obtain accurate solutions for the inerstitial fluid transport equations described in chapter 3, when results were compared to the respective analytical solutions, where available. Matrix **p** is described by three arrays each of size mb × mb × nb:

pa= array of diagonal blocks

pb= array of superdiagonal blocks

pc= array of subdiagonal blocks

as pictorially described in section 1.1.

(iv) Once the block-diagonal structure of **p** has been identified, one can provide a subroutine of the form adda(neq,t,y,mb,nb,pa,pb,pc) which adds the non-zero blocks of **a** to the contents of the arrays **pa**, **pb** and **pc**, following the structure description in (iii). (v) The jacobian matrix of the system was not provided externally, and so, a solver option was chosen where it is being approximately computed internally by difference quotients.

The solute concentration profiles were slightly unstable to the radial grid step size in a manner similar to the results of section 4.0.1 (see section 4.3, pert 1). Fig. 4.7 shows

the variation of the plasma-normalized bound IgG concentration with radial distance for continuous infusion. Fig 4.8 shows the respective results for the Fab fragment. Figs. 4.9 and 4.10 show the radial variation of the bound IgG and Fab profiles respectively, assuming that their corresponding plasma concentrations follow bi-exponential clearance laws (eq. 4.4). Fig. 4.11 shows the bound IgG radial profile after a 24hr constant perfusion for a R=1cm radius tumour with 50%, 75%, 95%, and 100% of R being necrotic. Fig. 4.12 shows the respective results for the Fab fragment. The total macromolecule concentration, equal to the sum of free and bound ones, was also calculated in all of the above cases. Since the bound molecule concentration is much greater than the free concentration, it was the former that essentially determined the total macromolecule concentration radial profile. Fig. 4.13 showing the total IgG distribution for continuous perfusion and fig. 4.14 showing the sum of figs. 4.5 and 4.11 illustrate this point.

4.2 Other Results and Sensitivity Analysis

As can be seen in sections 4.0 and 4.1, the solution of eqs. 4.2, 4.12, and 4.13 requires the knowledge of a large number of physiological parameters. Once the baseline results were obtained, it was of interest to vary the value of individual parameters, or several parameters in combination, keeping the others at their baseline values. This helped assess the relative importance of these parameters in optimizing macromolecule delivery.

Three important spatial attributes of macromolecule concentration and their sensitivity to variation of physiological parameters are also investigated:

(i) The average value of the macromolecule concentration over the whole tumour (C_{av}), as function of time. It is calculated by integrating the local value of the macromolecule concentration over the whole of the tumour volume for a fixed point in time and dividing by its volume. The calculation is then repeated for consecutive time points. C_{av} reflects the total macromolecule uptake by the tumour which can be directly compared to experimental values (e.g. Kwok *et al.* 1996).

(ii) The bound macromolecule concentration at the centre of the tumour (C_c) as expressed

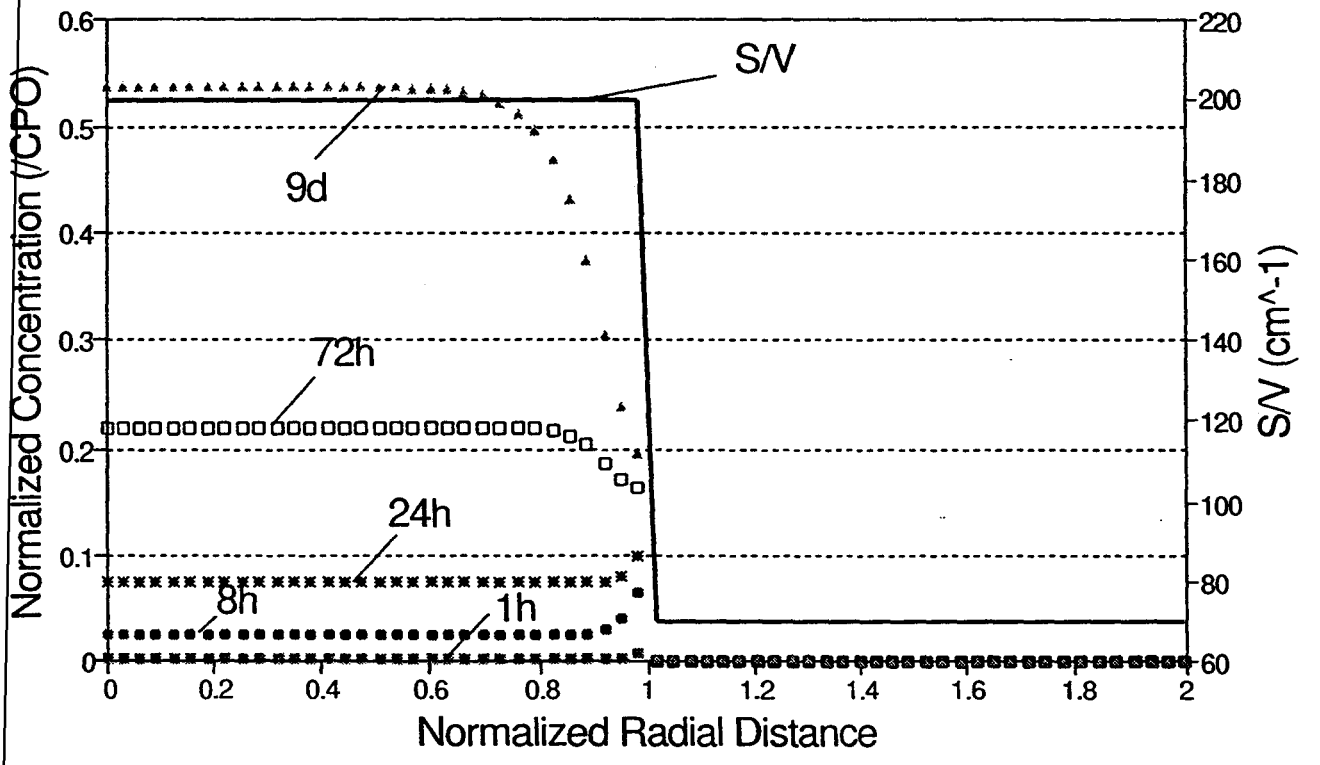

Fig. 4.7 The radial variation in a R=1cm tumour of the dimensionless bound IgG concentration at 1h (light-filled squares), 8h (dark-filled squares), 24h (asterisks), 72h (empty squares), 9d (light-filled triangles) for constant perfusion.

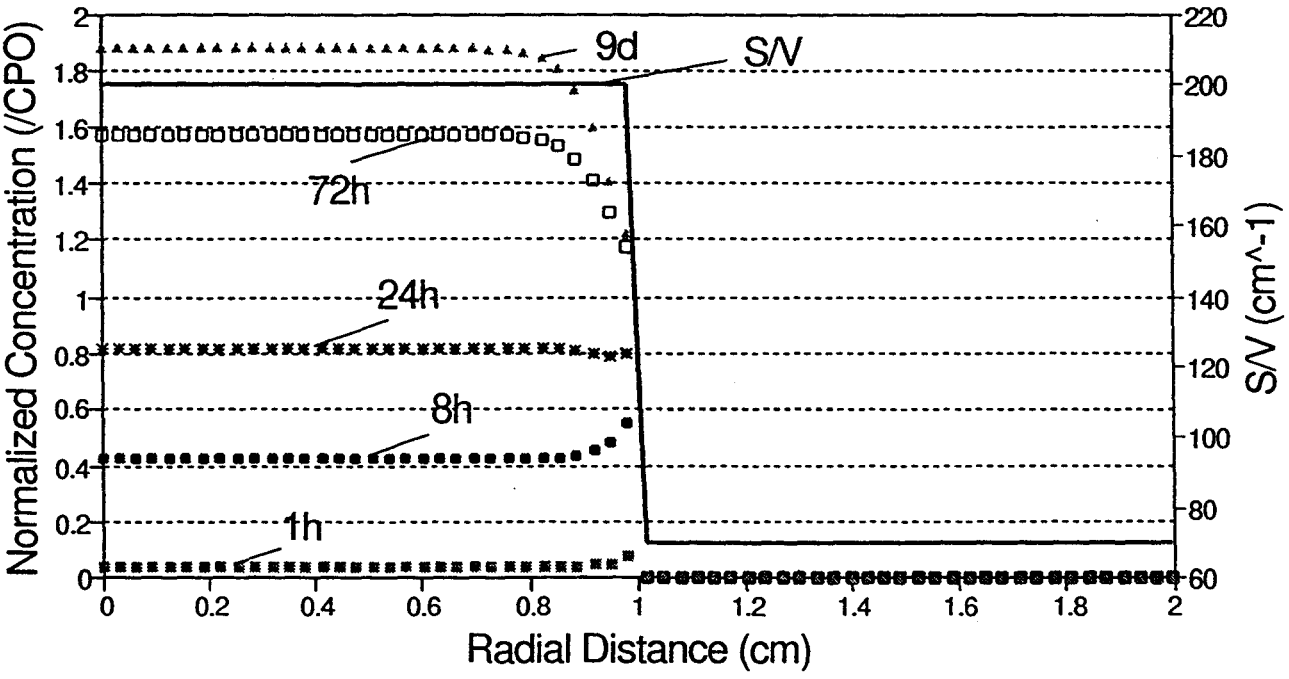

Fig. 4.8 The radial variation in a R=1cm tumour of the dimensionless bound Fab fragment concentration at 1h (light-filled squares), 8h (dark-filled squares), 24h (asterisks), 72h (empty squares), 9d (light-filled triangles) for constant perfusion.

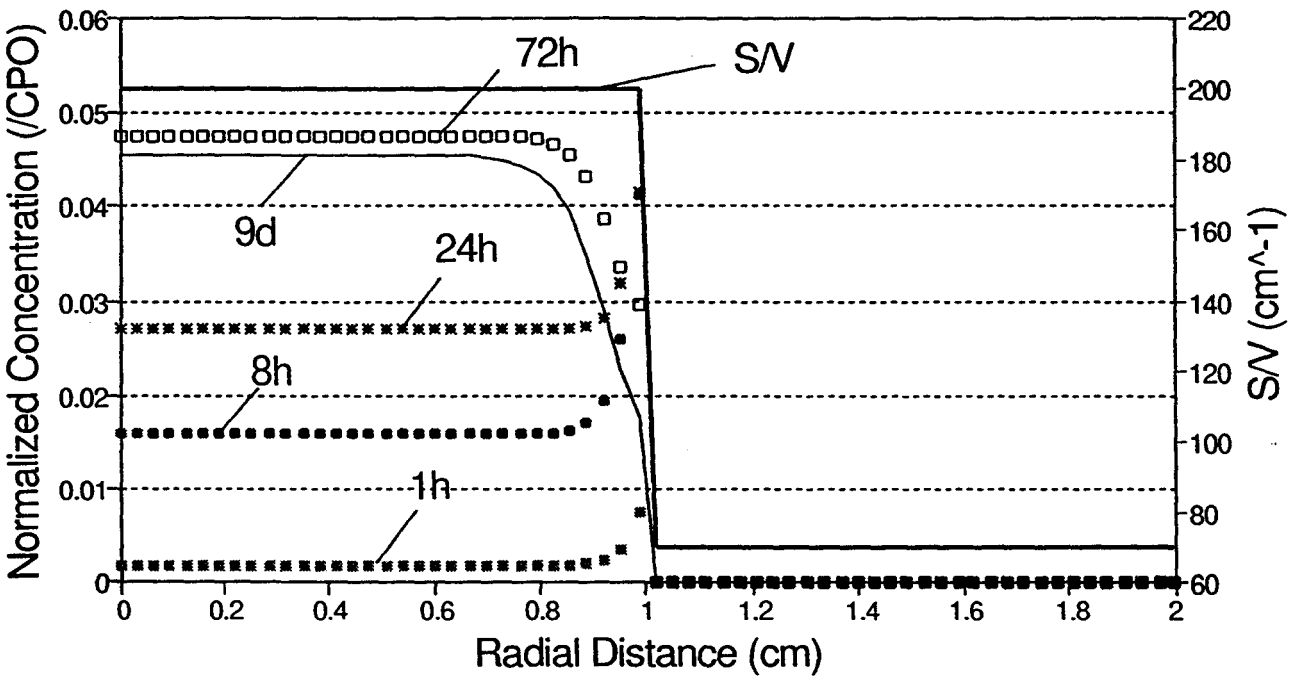

Fig. 4.9 The radial variation in a R=1cm tumour of the dimensionless bound Fab fragment concentration at 1h (light-filled squares), 8h (dark-filled squares), 24h (asterisks), 72h (empty squares), 9d (light-filled triangles) for a single bolus i.v. injection at t=0 (see eq. 4.4).

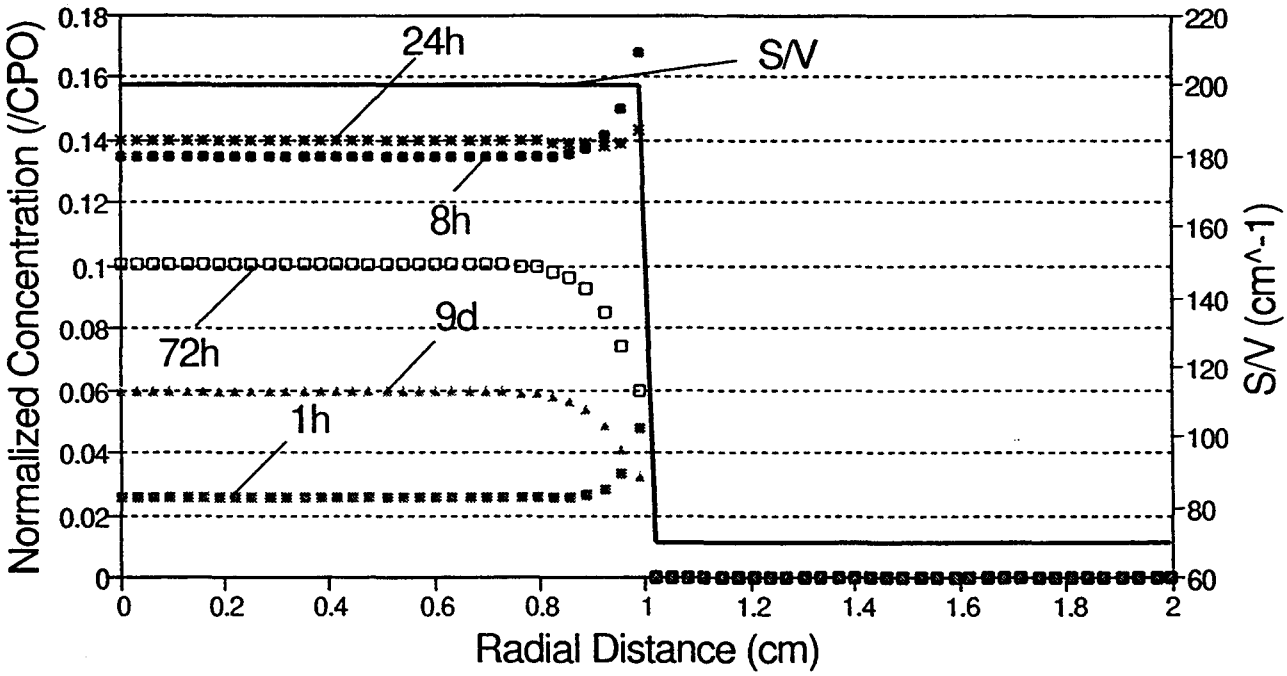

Fig. 4.10 The radial variation in a R=1cm tumour of the dimensionless bound Fab fragment concentration at 1h (light-filled squares), 8h (dark-filled squares), 24h (asterisks), 72h (empty squares), 9d (light-filled triangles) for a single bolus i.v. injection at t=0 (see eq. 4.4).

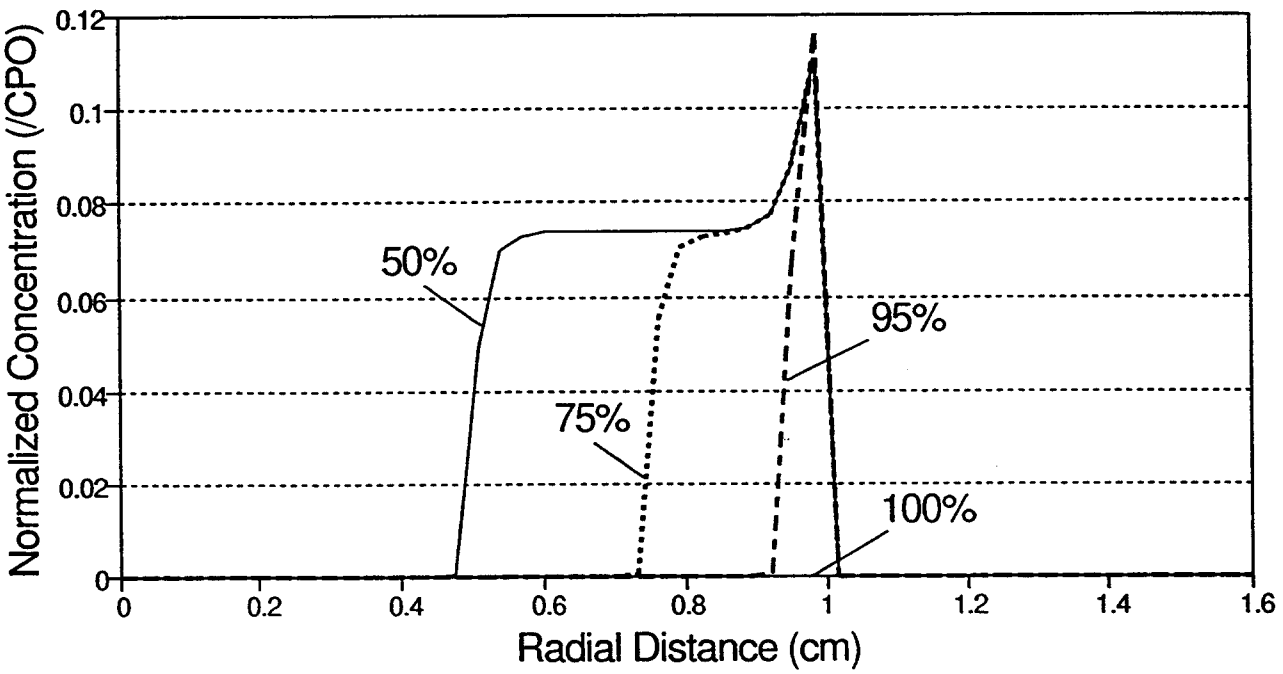

Fig. 4.11 The radial variation of the dimensionless bound IgG concentration after a 24hr constant perfusion in a R=1cm tumour having 50% (solid line), 75% (dotted line), 95% (centered line), and 100% (dashed line) of its radius being necrotic.

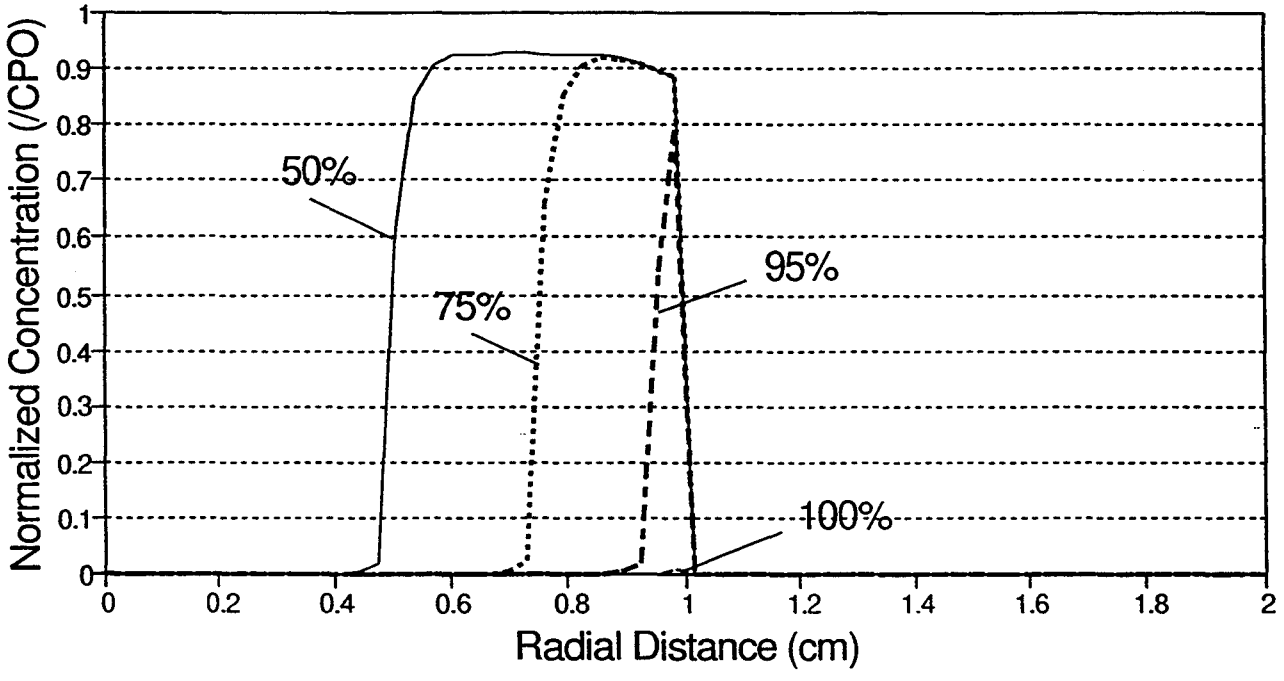

Fig. 4.12 The radial variation of the dimensionless bound Fab fragment concentration after a 24hr constant perfusion in a R=1cm tumour having 50% (solid line), 75% (dotted line), 95% (centered line), and 100% (dashed line) of its radius being necrotic.

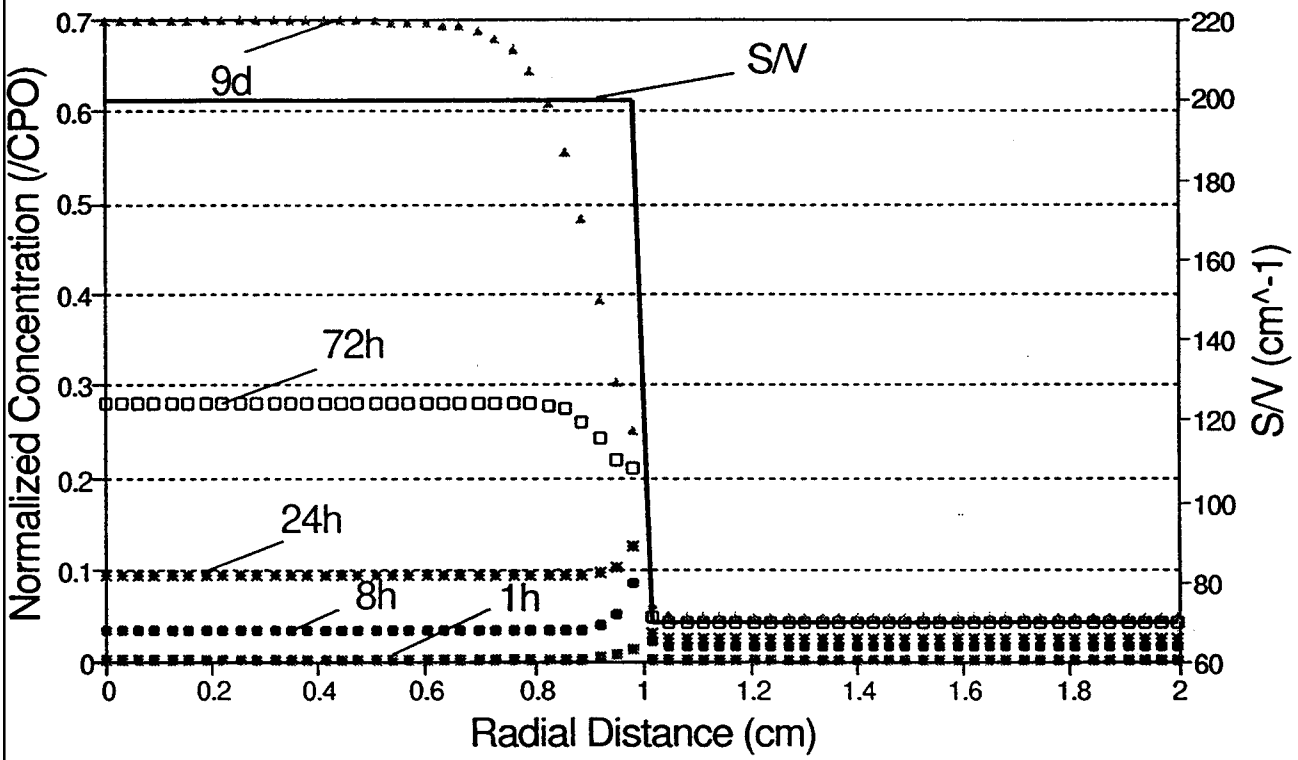

Fig. 4.13 The radial variation in a R=1cm tumour of the dimensionless total IgG concentration at 1h (light-filled squares), 8h (dark-filled squares), 24h (asterisks), 72h (empty squares), 9d (light-filled triangles) for constant perfusion.

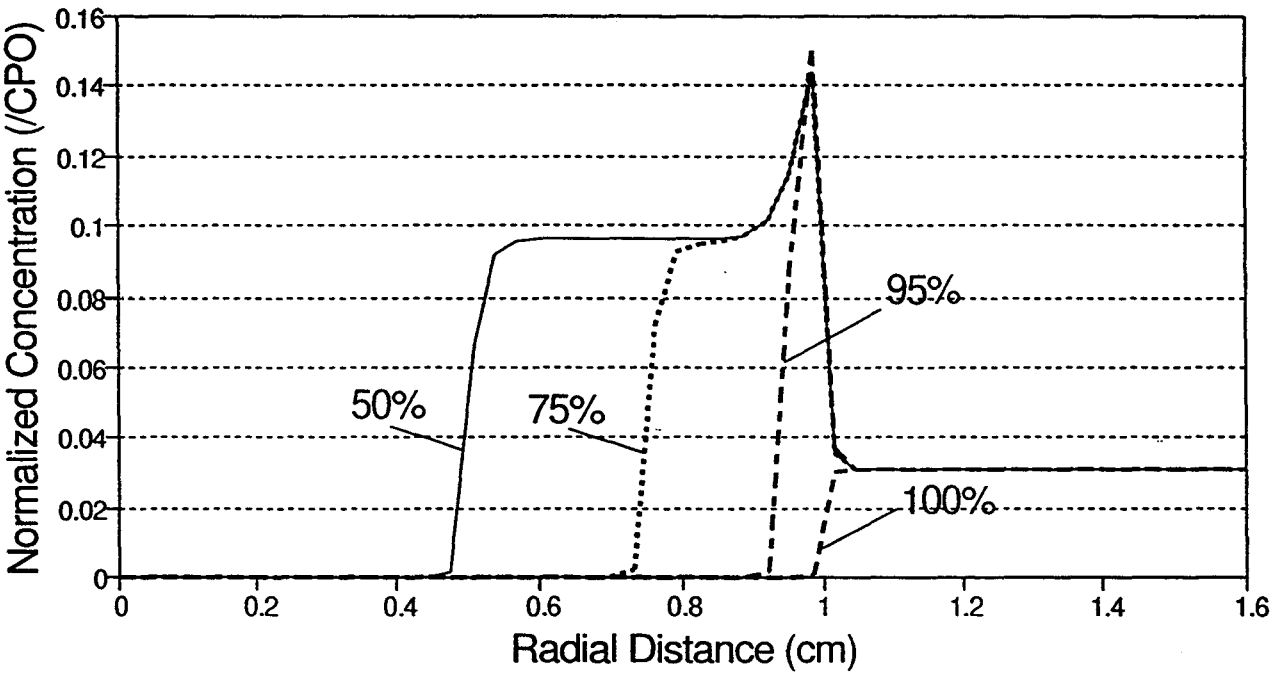

Fig. 4.14 The radial variation of the dimensionless total (free + bound) IgG concentration after a 24hr constant perfusion in a R=1cm tumour having 50% (solid line), 75% (dotted line), 95% (centered line), and 100% (dashed line) of its radius being necrotic.

as a percentage of bound C_{av}. It is an interesting parameter because the tumour centre is the hardest area to be reached by macromolecules in real-life tumours. This is because of the pressure build-up, and the radially decreasing S/V both having their largest effect in decreasing macromolecule perfusion there.

(iii) The index of spatial non-uniformity (ISN) defined by eq. 4.17, as a function of time. This will help illustrate which are the important physiological parameters that determine the spatial heterogeneity of macromolecule perfusion and give possible directions towards reducing it.

It should be noted that the definition of ISN (Fujimori 1990) is a valid definition of a normalized variance and a useful tool in describing the inhomogeneity in perfusion of multicellular spheroids, but was not found to be a very sensitive tool when considering vascularized tumours in the proposed 'distributed source' model. The reason is that the only macromolecular transport mechanism in the former is diffusion and the resulting concentration profiles are a lot steeper (ISN's larger by ~10^4 times). This means that for the macromolecule ISN's of two tumours with slightly different vascular distributions to be distinguishable, one has to take care in ensuring the accuracy of the numerical calculation.

4.2.1 The Effect of Binding Affinity and Metabolism

The macromolecule binding affinity (B_a) is defined as the ratio of the forward and reverse rate constants, k_f and k_r respectively. When both were increased by a factor of 10 keeping their ratio at baseline, all macromolecule radial profiles were identical to the baseline ones, as expected. Fig. 4.15 shows the total IgG radial profiles after a 72hr constant perfusion with B_a varying from 10^{-1} to 10^3 times the baseline value. Since the convective plasma flux peaks at a narrow region near the interface, as demonstrated in fig. 3.1, this is where the bound IgG peaks too. Also, it is seen that an increase in B_a by more than a factor of 100 has no effect, as all the available IgG binds to antigen. Whether the curvature of the concentration profile is upward, or downward near the interface was

found to be dependent both on B_a and length of perfusion. Increasing B_a tends to make all profiles curve upward. On the contrary, a constant 72hr perfusion with B_a 10^{-2} of the baseline value gives a downward curved profile with a sharp peak just outside the tumour due to free IgG wash-off. Increasing the length of constant perfusion increases the total macromolecule concentration but has a somewhat increased wash-off effect at the tumour's edge. This was deduced from comparing the 24hr constant perfusion results with the respective 72hr ones. Similar sets of results were obtained for the $F(ab')_2$ and Fab fragments as for the intact IgG. The curvature of the respective concentration profiles were almost identical to those of intact IgG, but the 'plateau' plasma concentration was approached at earlier time points with decreasing m.w. for the same length of perfusion.

If one increases the binding affinity for all macromolecule types by a factor of 10, the C_{av} increases by a factor of ~3 with increased uptake at later times especially for Fab. Another important consideration is how much larger C_{av} is from the non-specific macromolecule uptake in surrounding normal tissue. The dominant factor was found to be the ratio of B_{max} in tumour to that of normal tissue. For successful immunotherapy, this ratio should be 10^2-10^3.

When metabolism is included in the model, although the bound C_{av} is reduced, the C_c percentage increases. This is because of the convective flux and the resulting increased binding near the tumour's surface. Since k_c and B_{max} are independent in the proposed model, this leads to a larger percentage of macromolecule being metabolized at the tumour surface than near its centre. For an R=1cm tumour with a 90% necrotic core and bi-exponential clearance, the presence of metabolism increases the maximum C_c reached by ~1% for Fab. No IgG, or $F(ab')_2$ ever reaches the tumour centre. All C_c vs. t curves with bi-exponential clearance show a fast rising portion, and then a less steep one in the initial increase part peaking at ~75hr. This is a reflection of the bi-exponential clearance laws since they have a larger effect on the total bound macromolecule near the surface of the tumour where the solvent flux is greatest. Thus, C_c follows the inverse of that trend and increases in a similar manner. Increasing B_a for all macromolecule types by a factor of 10 has an effect on C_c similar to doubling the tumour radius. In the presence of metabolism and bi-exponential clearance, there is an initial C_c rise from 57%

to 62% for IgG, 64% to 69% for $F(ab')_2$, and 72% to 76% for Fab at the peak C_c time point of ~75hr. The decrease at longer times is very slow showing an enhanced 'reservoir' effect with each macromolecule type having a C_c (t<1hr) close to the one at 360hr post-injection.

For constant perfusion the ISN's for bound macromolecule are very similar to the ones obeying a bi-exponential clearance law for the first 150hr. This shows that the ISN's are not very sensitive to the exact form of the plasma clearance law. Increasing the binding affinity for all macromolecule types by a factor of 10 increases all ISN's in a way similar to the one described in section 4.2.2 below, when making S/V steep. Antigen metabolism increases all ISN's when saturation of binding sites has not been reached since a smaller proportion of free macromolecule will be available to move towards the less well perfused areas.

4.2.2 The Effect of S/V and the Tumour Radius

The macromolecule radial profiles were studied for a radially variable S/V in the tumour. Fig 4.16 shows the resulting profiles for constant IgG perfusion for an exponentially decreasing S/V according to eq. 3.20 (A=1, B=5). The calculated ISN (eq. 4.15) for the vascular distribution (ISNG) was always less than the ISN's of free (ISNF), bound (ISNB), and total (ISNT) IgG concentration distributions. This turned out to be an observation for all macromolecule types. This means that the macromolecule distribution is always more non-uniform than the vascular distribution. The ISN's for concentration reduce with time but they never reach ISNG.

This effect is more pronounced when considering exponentially decreasing S/V's (e.g. eq. 3.20, A=1, B=5). The ISNB increases by a factor of ~2 w.r.t. the constant S/V case, for all macromolecule types and the higher the m.w. the higher the ISNB is at all times with no minimum in the curve. This is related to the fact that ~40% of the tumour has a very low value of S/V and diffusion of macromolecule from the area near the edge of the tumour, where the dominant mode of transport is convective, to the central area determines the ISNB. For a steeper, exponentially decreasing vascular distribution (A=1,

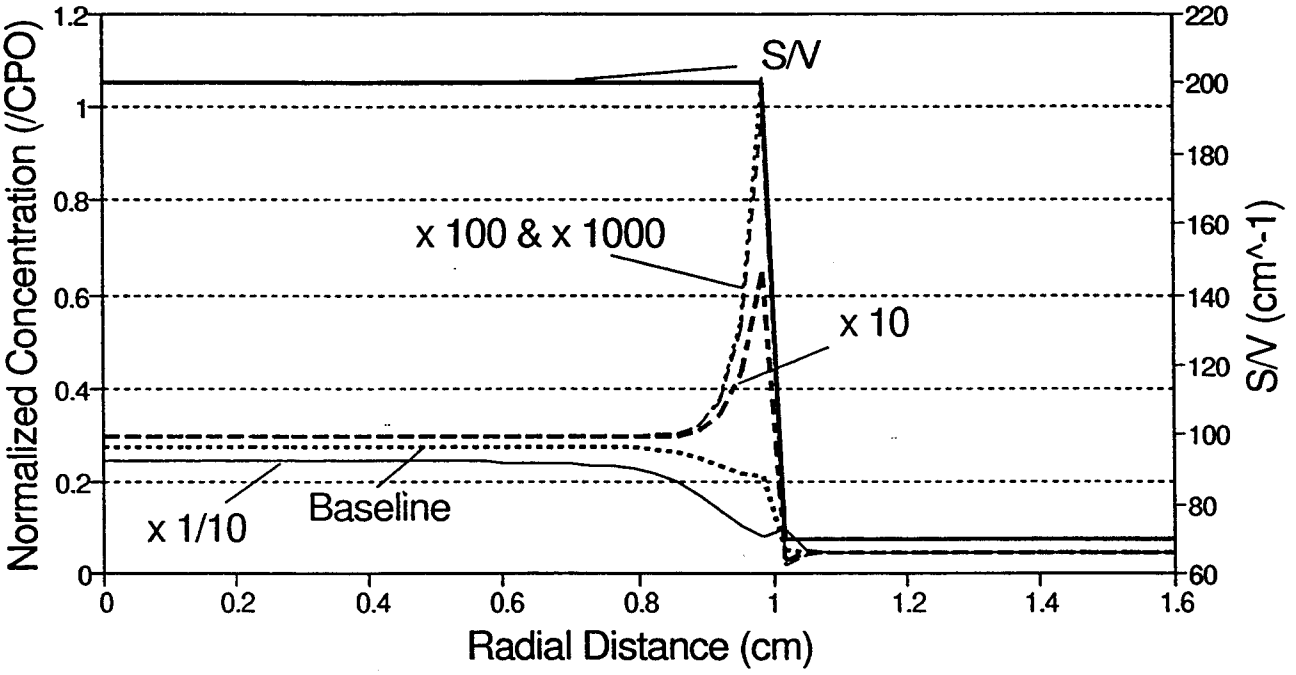

Fig. 4.15 The total IgG radial profiles after a 72hr constant perfusion with the binding affinity B_a having values of 10^{-1} (solid line), 10^0 (dotted line), 10^1 (centered line), and 10^3 (dashed line) times the baseline value.

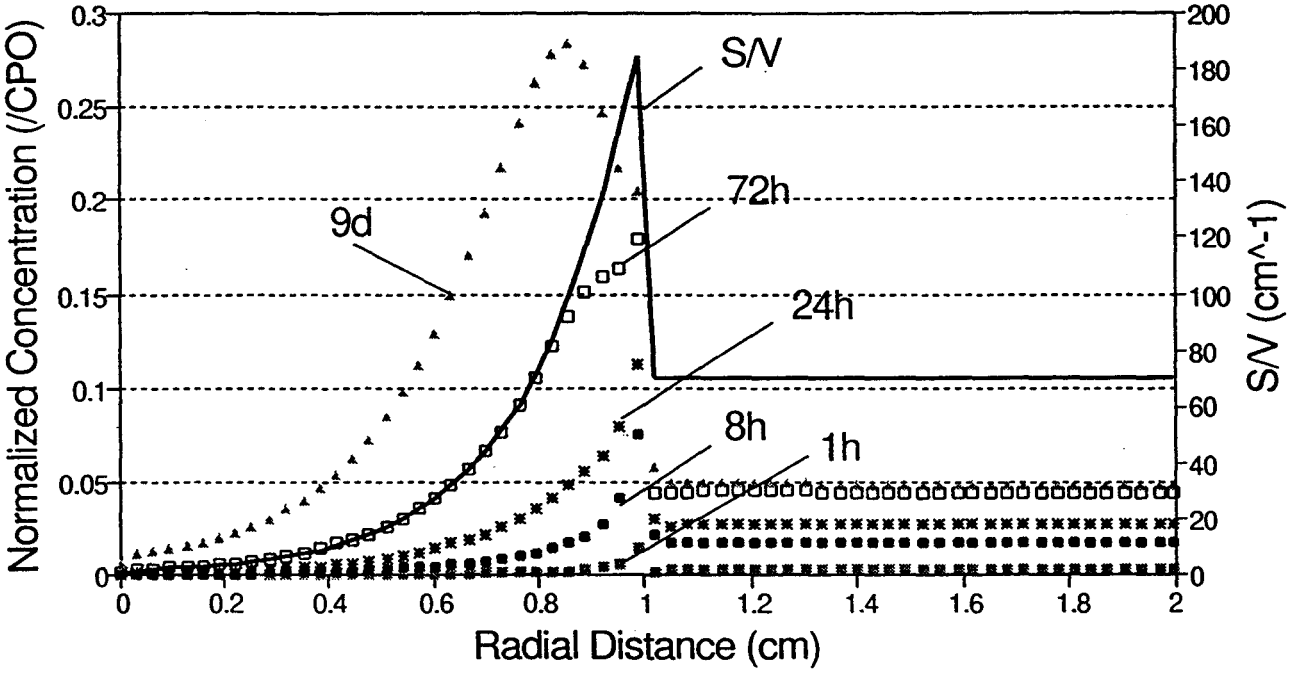

Fig. 4.16 The total IgG radial profiles for constant perfusion and an exponentially decreasing S/V (eq. 3.20, A=1, B=5) at 1h (light-filled squares), 8h (dark-filled squares), 24h (asterisks), 72h (empty squares), 9d (light-filled triangles), all else being baseline.

B=10) and constant IgG perfusion the ISN's are larger, as expected. However, they decrease with time faster than the former case, but only manage to catch up at long, physically unattainable times. Doubling the radius of the well perfused tumour to 2cm makes very little difference w.r.t. baseline for all macromolecule ISN's.

The case of a sigmoid-shaped vascular radial distribution (eq. 3.19) was also studied (A=1, B=0.15, C=1/14, D=0). Since the vascular distribution for this choice of parameters was uniform near the surface and dropped abruptly near the centre of the tumour, the resulting concentration profiles combined characteristics of both figs. 4.13 and 4.16, but added no physical insight.

Another case studied was that of constant perfusion and exponentially decreasing vascular distribution (A=1, B=5) with B_a increased by a factor of 10. More antibody was bound for the same length of constant perfusion. The ISN's changed less with time. For A=1, B=5 and $F(ab')_2$ and Fab fragments, more binding was predicted for decreasing m.w. at constant perfusion. The ISN's for $F(ab')_2$ were somewhat lower but very close to the corresponding IgG case, and decreased in steps of similar size between time points where the solution was evaluated. For Fab the ISN's were reduced by a factor of ~3 w.r.t. IgG and even more binding was predicted for constant perfusion.

Fig. 4.17 shows the variation of C_{av} of bound IgG, $F(ab')_2$, Fab as a function of time post-injection with the plasma concentrations obeying their respective bi-exponential clearance laws (eq. 4.4). If S/V is decreasing exponentially (eq. 3.20, A=1, B=5), the C_{av} is decreased, more so for the heavier macromolecules especially at early times when Fab extravasates and spreads faster in the tumour interstitium. These trends remain the same and are enhanced for a steeper S/V (eq. 3.20, A=1, B=10). The bound C_{av}'s for all macromolecule types follow the trends of their respective total C_{av}'s, as the bound concentration is the dominant component when baseline parameters are assumed. For a R=1cm tumour with a 90% necrotic core and bi-exponential clearance, no Fab reaches the centre in the first 10hr post-injection. After that, there is a sharp rise of C_c for Fab in the first ~75hr to only 2.5% of C_{av} and then a much more gradual decay. No IgG, or $F(ab')_2$ reaches the centre at any time.

If the radius of a well perfused tumour is increased to 2cm the total bound

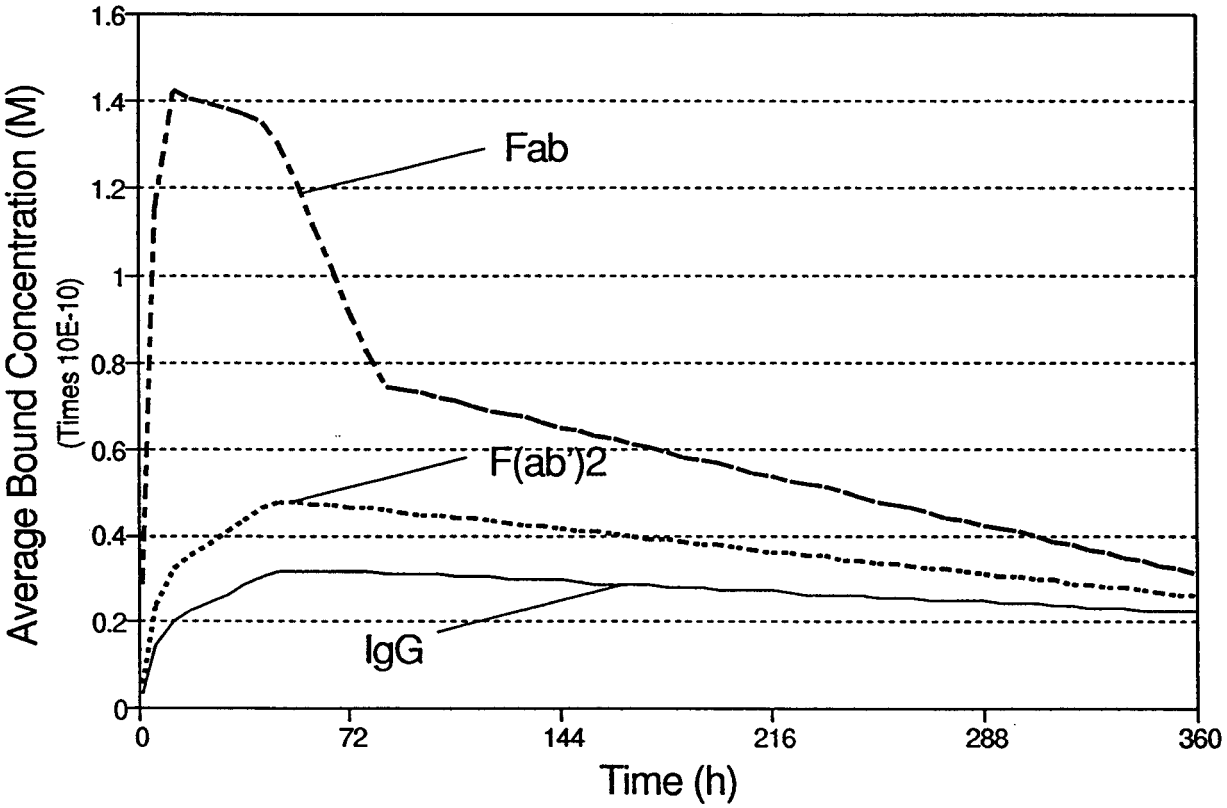

Fig. 4.17 The average over a whole tumour of R=1cm of the total bound IgG (solid line), $F(ab')_2$ (dotted line), and Fab (dashed line) concentrations as a function of time after a single bolus i.v. injection at t=0.

macromolecule is increased by a factor of ~8 w.r.t. the 1cm case which is consistent with the volume ratio of the two. In the case of constant perfusion the bound and total macromolecule concentrations are ever-increasing with the respective Fab concentration always being higher, more so at early time points. This holds true for all tested for all S/V's and tumour radii. For the R=2cm well perfused tumour, everything else being baseline, the time point where C_c peaks remains at ~75hr, but the peak values decrease, more so for higher molecular weights. For IgG it drops from 90.5% to 70%, for $F(ab')_2$ from 93% to 74%, and for Fab from 89.5% to 78%. This is both because of the larger extent of the interstitial pressure plateau where only diffusive transport can occur, and the presence of metabolism which reduces the amount of macromolecule available to diffuse towards the centre. Also, the rate of decrease of C_c at longer times is slower showing an enhanced 'reservoir' effect, again due to larger extent of the interstitial pressure plateau.

Finally, the C_c vs. t for an exponentially decreasing S/V (eq. 3.20, A=1, B=5) in the presence of metabolism and bi-exponential clearance was examined. The peak time point values were 1.5% for IgG, 1.7% for $F(ab')_2$, 3.4% for Fab, a lot less than the respective values for a well perfused tumour. The slope in the increasing C_c part of the curve at early times depends on the form of S/V and increases with decreasing m.w..

4.2.3 The Effect of Diffusive Permeability (P) and Molecular Weight

The effect of macromolecular m.w. and its effect on the microvascular permeability to them, can be seen in the concentration radial profiles for IgG, $F(ab')_2$, and Fab at a particular point in time. Fig. 4.18 shows the total macromolecule concentrations in the interstitium of a tumour for a 72hr constant perfusion in the presence of metabolism. It shows that the lower m.w. fragments attain larger interstitial concentrations as they extravasate more readily. Increases in total macromolecule concentrations are not linearly proportional to increases in m.w. with Fab total concentrations ~6 times more than $F(ab')_2$ and the latter ~2.5 times more than IgG. If the effective diffusive permeability (P) is increased by a factor of 10 for all macromolecule types, all concentrations are increased,

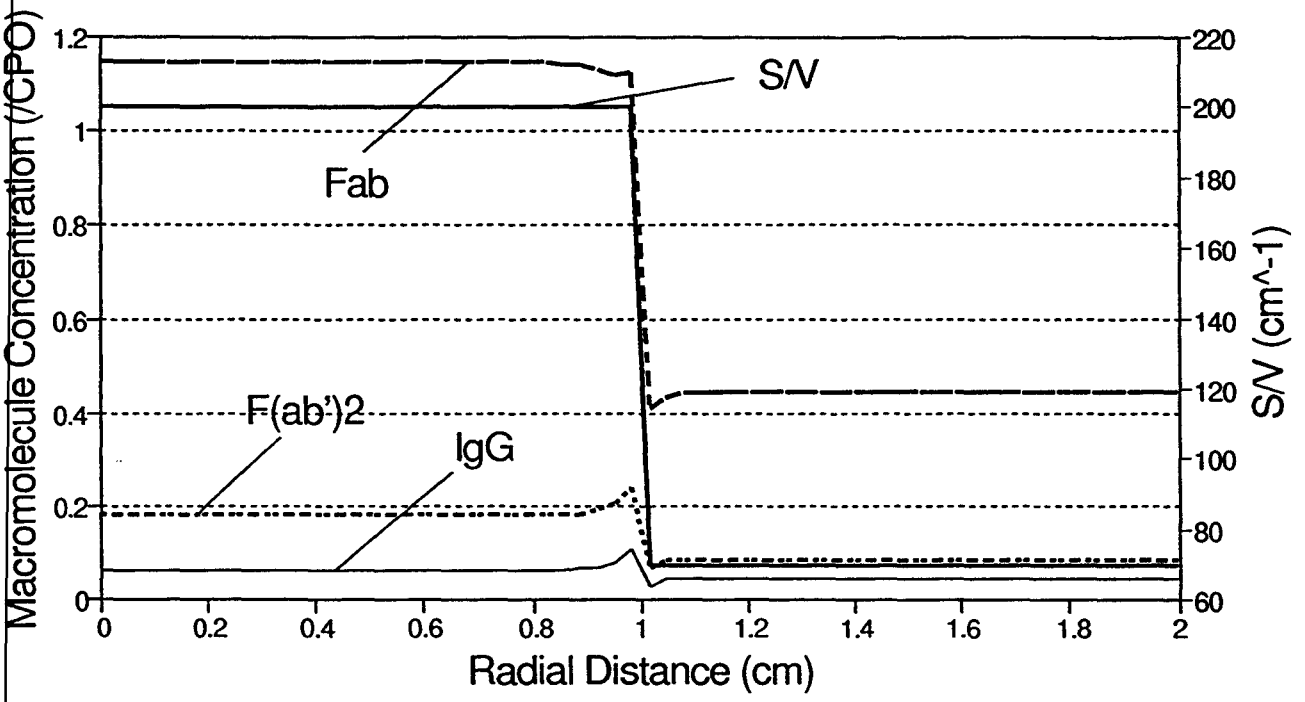

Fig. 4.18 The total IgG (solid line), $F(ab')_2$ (dotted line), and Fab (dashed line) concentrations in a R=1cm tumour for a 72hr constant perfusion in the presence of metabolism.

but not by the same amount. The total IgG is increased by a factor of ~7, the $F(ab')_2$ by a factor of ~6.5, and the Fab by a factor of ~2. If the P's are all increased by a factor of 100, the $F(ab')_2$ is the macromolecule type with the highest concentration, and if P is increased even further the IgG becomes the one with the highest concentration. This counter-intuitive result demonstrates one of the inadequacies of the transport model (see section 4.3, part 3). It was also found that increasing the average value of S/V by a given percentage and keeping P constant has a similar effect to keeping S/V constant and increasing P by the same percentage.

When the macromolecules obey their respective bi-exponential clearance (eq. 4.4) laws, the total concentrations are lower w.r.t. the constant perfusion cases at all times, for the same initial plasma concentration. The Fab fragment still has the highest concentration and $F(ab')_2$ the second highest. This is in contradiction to what was observed from experiment (Sharkey *et al.* 1990, Vogel *et al.* 1993) where except for early time points, the IgG has a higher total concentration than $F(ab')_2$ and the latter higher than Fab. The respective C_{av} results are also not consistent with experimental observations of macromolecule uptake over the whole tumour (e.g Fand *et al.* 1992, Vogel *et al.* 1993), as they tend to overestimate the total extravasated quantity of $F(ab')_2$ and Fab relative to IgG. Increasing P in the presence of bi-exponential clearance gives similar trends to the ones described above for constant perfusion.

In the case of an exponentially decreasing S/V (eq. 3.20, A=1, B=5) and bi-exponential plasma clearance, at 72hr post-injection, the peak of the macromolecule distribution does not coincide with the maximum value of S/V in radial position. The former is near, but not at the edge of the tumour and the lower the m.w. the deeper it goes. At early time points no significant peak in the macromolecule distribution has built-up. The case of a 90% necrotic core tumour was also examined. It predicted that free macromolecule spreads further inside the necrotic core than bound, as expected, although the actual amount is only a small percentage of the macromolecule found in the well perfused area. It was found that the two most important factors in determining the amount and spread of macromolecule in the necrotic core were P, and the binding affinity. However, even for baseline and higher P's the model predicts that $F(ab')_2$ spreads

the furthest in the necrotic area which is contrary to what is intuitively expected i.e. the Fab fragment, because of its smaller molecular weight.

For constant macromolecule perfusion of a well perfused tumour, and baseline parameters proposed by Baxter and Jain (1989c), the C_c percentage values for bound IgG, $F(ab')_2$, and Fab were 57%, 65%, and 72% respectively for t<1h. At times longer than ~75hr they all reached, at similar rates, their asymptotic values of 73%, 77%, and 81% respectively. When the macromolecules follow bi-exponential clearance (eq. 4.4), all else being baseline, the relative magnitude of the percentage for each macromolecule type changes with time. The initial percentages were identical to the ones mentioned above for constant perfusion. However, at 360hr post-injection although little macromolecule remained in the tumour as a whole, C_c was 107% for IgG, 104% for $F(ab')_2$, and 87% for Fab. This demonstrates a 'reservoir' effect at longer times which increases with higher molecular weights. Fig. 4.19 shows the C_c profiles for bi-exponential clearance in the presence of metabolism with all baseline permeability values increased by a factor of 10. This permeability increase changes the relative magnitudes of C_c for different macromolecule types, as it did for the overall spatial macromolecule distributions (see section 4.3, part 3). Fig. 4.19 also demonstrates the reservoir effect for IgG.

Fig 4.20 shows the ISN for bound macromolecule and bi-exponential clearance all else being baseline. Initially, the macromolecule spreads in the tumour and ISN decreases, but at later times ISN increases again because of clearance and the 'reservoir' effect. Thus one ends up having the most uniform distribution ~55hr post-injection. It is interesting to note that the time point of the peak value of the average bound concentration (see fig. 4.17) is close, though not identical to the minimum ISNB time point. The existence of a minimum in the ISNB curve has also being observed in the case of IgG percolating multicellular spheroids (Van Osdol *et al.* 1991). The minimum ISNB time point occurs later with increasing m.w. and as a result, there is a time interval over which the fragments have higher ISN's than the intact antibody. Smaller m.w. macromolecules diffuse further and hence produce lower ISN's. The same trends are observed for even steeper S/V profiles (eg. eq. 3.20, A=1, B=10, or a 90% necrotic core). The ISNB's are similar to the ISN's for the total since the bound is the dominant component.

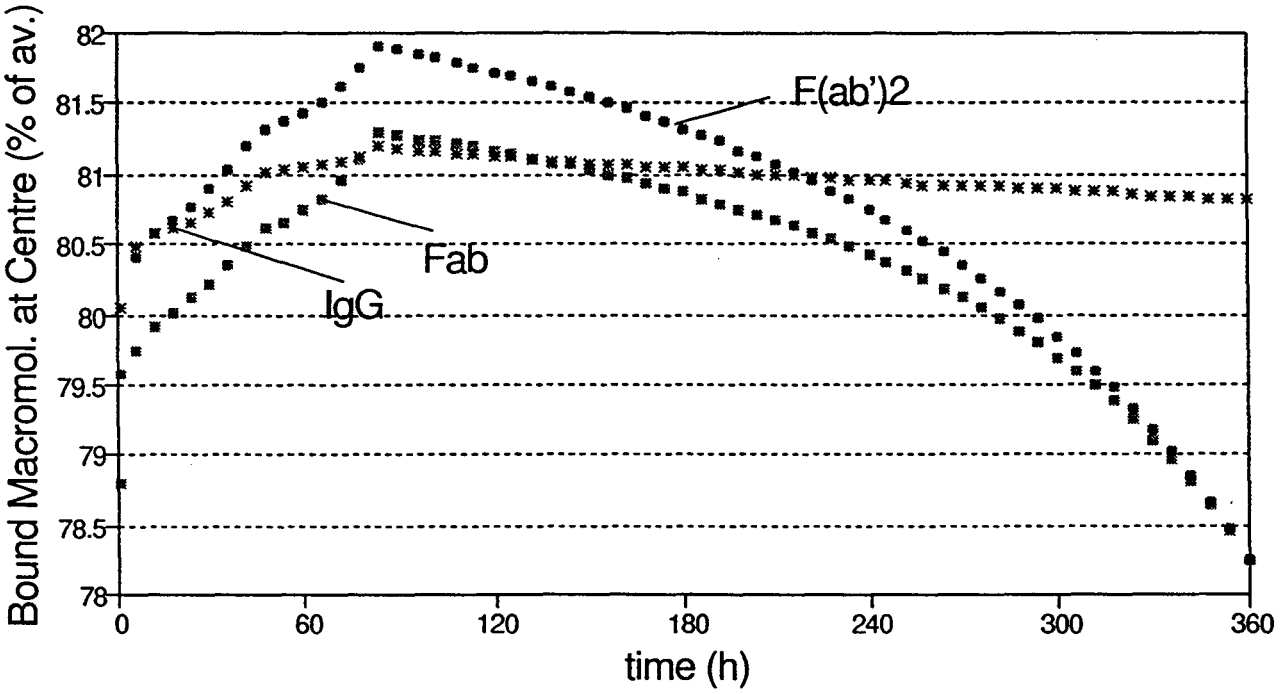

Fig. 4.19 The bound macromolecule concentration at the centre of the tumour expressed as a fraction of the total bound concentration over the whole tumour, as a function of time for IgG (asterisks), $F(ab')_2$ (dark-filled squares), and Fab (light-filled squares). All vascular permeabilities P_{eff} are 10 times their baseline values.

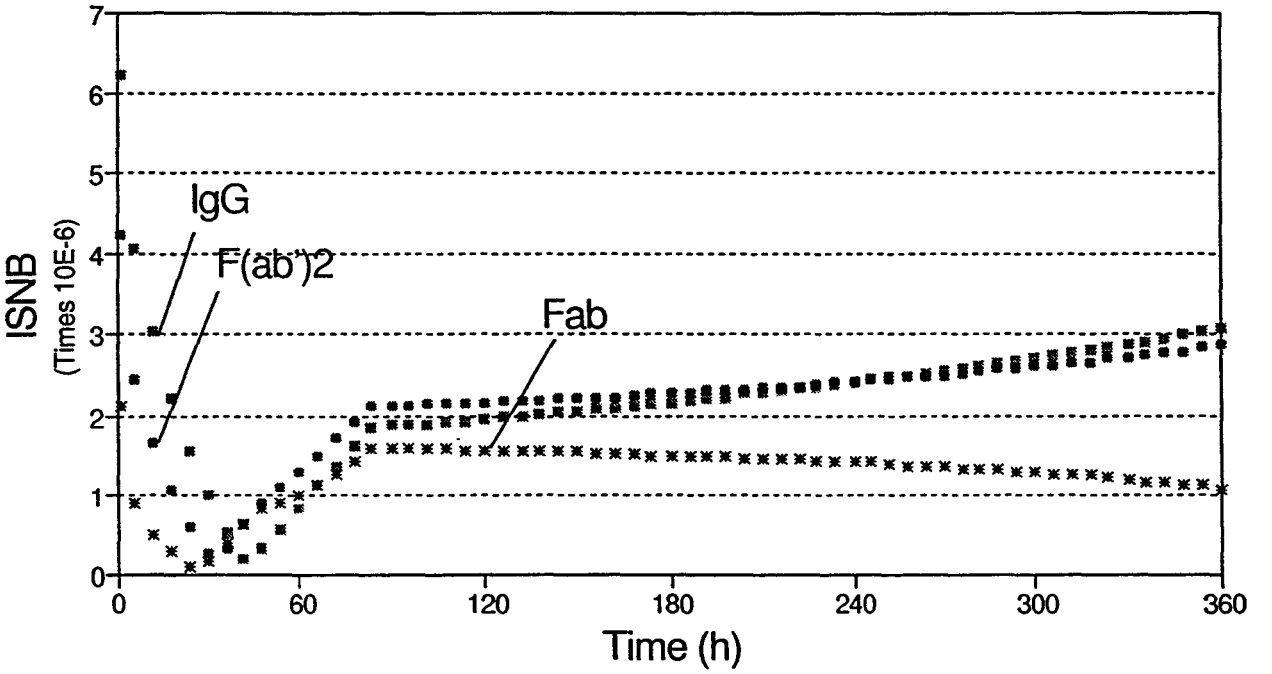

Fig. 4.20 The variation of the ISN (eq. 4.15) for bound IgG (light-filled squares), $F(ab')_2$ (dark-filled squares), and Fab (asterisks) with time in a R=1cm tumour. The plasma clearence is bi-exponential (eq. 4.4) and all parameters are baseline.

If the effective diffusive permeability is increased by a factor of 10 the ISN profiles change significantly. Although the maximum ISN values are ~2.5 times less than baseline, implying a more uniform perfusion, they don't occur at t=0, but at t≈90hr. Before the peak time point, the ISN's increase sharply and after it they gradually decrease. This implies that at early time points the increased amount of extravasation near the tumour's edge increases the overall ISN's. However at later times, the increased concentration at the periphery tends to spread towards the inner of the tumour thus gradually decreasing the ISN's. Increasing P by a factor of 100 further decreases the ISN's in a similar manner.

4.3 Limitations of the model

The following limitations of the model were realized upon detailed examination of the origin of input parameters, the nature and results of the interstitial plasma and macromolecule transport equations. Comparison with experimental data was made, where available.

1) The solutions of the macromolecule transport equations (eqs. 4.2, or 4.12 and 4.13) are mildly numerically unstable upon variation of the radial grid density. This occurs predominantly in the tumour-normal tissue interface region where the physiological parameters change abruptly and the interstitial fluid pressure gradient is steep. At t=72hr this translates to a <5% change in the local free macromolecule concentration values just within the tumour's surface for a uniform 10-fold decrease in grid spacing over the whole domain. Just outside the tumour's surface the change in local free macromolecule concentration values could be >10%. The error is not very conspicuous for t<24hr, but it builds up at later times. It is not clear which component of the formulation causes this instability. A demonstration of the inadequacy is that the plasma Peclet number (eq. 3.21) needs to be defined in a way that deviates from the conventional definition in order to accommodate the distributed source model. The standard definition (e.g. Van Osdol 1991) requires it to be constant and positive. In the present model it varies with radial position and assumes large negative values in the normal tissue just outside the tumour edge. The

above suggests that the 'distributed source' model used to describe a spatially averaged plasma and macromolecule transport across the capillaries, and into the interstitium of a vascularized tumour needs to be refined.

2) The radial interstitial plasma pressure profile on either side of the tumour - normal tissue interface is steeper than the one observed in real tumours (Jain 1987). There are three components in this:

(i) The physiological parameters change abruptly at the tumour - normal tissue interface. In practise, some lymphatics found in the surrounding normal tissue will penetrate the tumour and will somewhat relieve the pressure build-up near the interface. Also, the blood vessels in normal tissue recruited by the tumour to provide its blood supply penetrate the tumour and provide the starting points of tumour vessel angiogenesis. Thus, the transport properties of some of the vessels near the interface are those of ones in normal tissue i.e. less leaky.

(ii) The source term (eq. 3.3) is assumed to have radial symmetry in order to avoid mathematical complexity, but retain the main physical characteristics of the plasma transport model. Homogeneous perfusion from a single, net flow source term, however, overestimates the spatial extent of the plateau pressure build-up and the steepness of the macroscopic interstitial pressure gradients, and limits the areas where convective plasma transport occurs. Also, convective transport is the dominant form of macromolecule transport (Baxter & Jain 1989) and has a profound effect on the predicted macromolecule distribution.

(iii) The vascular pressure and the osmotic pressure of the interstitial fluid are assumed spatially invariant in this model. It is known from vascular physiology (e.g. Tortora & Grabowski 1993, p. 631) that the capillary vascular pressure varies from ~35mmHg in the arterial end to ~16mmHg in the venous end. The spatially invariant vascular pressure used in the model for both tumour and normal tissue (p_V=15.6mmHg for a dog forelimb, Brace & Gyton 1977) is at the lower end of the physiological range for humans unless one incorporates the even lower pressure of the post-capillary venules in the average. Since the difference between the osmotic pressures of plasma and interstitial fluid changes little between the arterial

and venous ends (*ibid* pp.632-3), the net flow reverses from outward in the former to inward in the latter. Given the convoluted structure of the capillary network and assuming the same transport parameter for capillaries and post-capillary venules, it is reasonable to use a single, net flow source term. However, the local variations of net transcapillary flow imply an effect on the local value of the steady state interstitial osmotic pressure. The latter is assumed to be an independent constant in eq. 3.3.

3) The distributed solute source term (eq. 4.3) obtained using the single-pore model for transcapillary exchange (Curry 1984) includes the effective diffusive permeability (P), and the infused macromolecule reflection coefficient (σ) of the capillary wall in its definition. Also, the distributed solvent source terms (eqs. 3.3 & 3.4) contain the hydraulic conductivities of the capillary and lymphatic walls (L_p, L_{pL}) and the average plasma protein reflection coefficient (σ_T). All of these physiological parameters are implicitly a function of pore size. It makes sense intuitively that if the pore size is increased eg. using a vasodilator, then more plasma fluid and proteins, as well as infused macromolecules will be able to cross the capillary and lymphatic walls. This will increase the hydraulic conductivities and the effective diffusive permeability and reduce the reflection coefficients. However, these parameters are presented as independent on input in this model. This opens the question of whether the input parameter values are consistent with each other since they have been gathered from a number of different investigators (see sections 3.0 & 4.0) and experimental conditions. Also, this does not allow one to vary the magnitudes of these parameters to determine which ones are more important, without making an error in the estimation of the contribution of the related parameters to fluid and macromolecule transport. For example, the model seems to be insensitive to the variation of σ.

4) A single pore model may be insufficient to determine capillary permeability. Evidence for that comes from Baxter (1994) who incorporated a two-pore model in a pharmacokinetic model. He reported that the two-pore model gives better agreement with biodistribution data, and that the former overestimated capillary permeability by a factor of 1000. The pores of the model are the fenestrations in the plasma membrane, or

intercellular clefts of the endothelial cells constituting the capillary walls. Due to the higher metabolic rate of the cancer cells, rapid, but haphazard angiogenesis occurs. The number and size of the resulting capillary fenestrations are larger making the 'pore' pathway the dominant form of transport. The pores can be of variable size, but in order to avoid mathematical complexity, the least number of different sizes should be used to simulate accurately the observed extravasation profiles.

5) The input parameters of the model have been collected from a wide variety of reports in the literature both from humans and animal models. The resulting quality of these parameters is questionable. For example, the value of σ_T for subcutaneous tissue was used for the normal tissue value, and that of frog mesentery for the tumour value. For some parameters there was no available data and only a ballpark estimation was possible. For example, the value of L_p for normal tissue was estimated from knowledge of the values for skeletal muscle and intestinal capillaries. There is no value available for the diffusion coefficients of macromolecules in necrotic tumour tissue, and so the respective coefficients for viable tumour were used ignoring the structural differences between the two. Also, the maximum concentration of bound macromolecule (B_{max}) and the metabolism rate constant are assumed independent of each other. This implies an automatic recycling of the antigen presenting site in view of the lack of information on antibody-antigen metabolism kinetics. Also, the quality of the effective diffusion coefficient (D_{eff}) and the effective permeability (P) in tumour as determined by Gerlowski and Jain (1986) is dubious. The reason is that they were obtained by fitting their macromolecule spatial distribution data to a purely diffusive transport equation whereas in the present model Baxter and Jain (1989a) predict that the dominant mode of transport is convective. The latter model is insensitive to variations of D_{eff}, but P_{eff} is one of the dominant factors in determining the amount of macromolecule extravasation. The former report lumps the convective and diffusive contributions into an 'effective diffusive permeability coefficient' and is used as input in the latter. In defense to the above rough estimates made to provide input for the model, one has to point out the sheer difficulty of measuring accurately the required physiological parameters in vivo.

6) The actual spatial distributions of all physiological parameters required as input in

the model are very inhomogeneous. For example, the predicted plasma gradients around individual capillaries are very steep (Fleischman *et al.* 1986) and the observed tumour specific IgG distribution concentrates in narrow regions around blood vessels (Juweid *et al.* 1992). The heterogeneous IgG distribution is one of the major limitations of this cancer therapy modality. Moreover, it is currently impossible to determine from experiment the actual spatial distributions of capillaries and venules as well as the spatial permeability variations of individual vessels and related physiological parameters in vivo. While working towards a deterministic model, in addition to the mathematical complexity of the possible formulation, one would encounter huge data acquisition, computation time and RAM, and numerical analysis problems. Also, each tumour originating from the same cell line is different in its detailed structure, but has the same macroscopic physiological characteristics. All the above indicate that the development of a sound non-deterministic transcapillary transport model is a lot more feasible and useful in practice. However, it is still necessary for one to develop a detailed model of transcapillary transport across a single, or combination of a few, capillaries and compare with the actual profiles obtained from experiment. This will help one to determine which the more important parameters are, of the many used in the current formulation, and also what features a model of the whole tumour should have so that the macromolecule concentration in areas away from vessels is not grossly overestimated. The above will also provide a bridge between the micro-scale of individual capillaries, and the macro-scale of tumour tissue.

As a result of all the above limitations of the model, the predicted total macromolecule concentrations as a function of time does not agree with available experimental data (Kwok *et al.* 1995). Limitations (1) and (4) are considered to be the most important ones. The former, because the numerical instability shows that there is a problem with the formulation of the equations, and the latter because of existing two-pore biodistribution models (Baxter *et al.* 1994). In fig. 4.21 the dotted line shows the measured total IgG concentration in ovarian (OVCAR) solid tumours grown in nude mice. The model used a fitted bi-exponential plasma clearance rate obtained from the experiment and assumed a tumour of 0.38cm radius which was the estimated average size

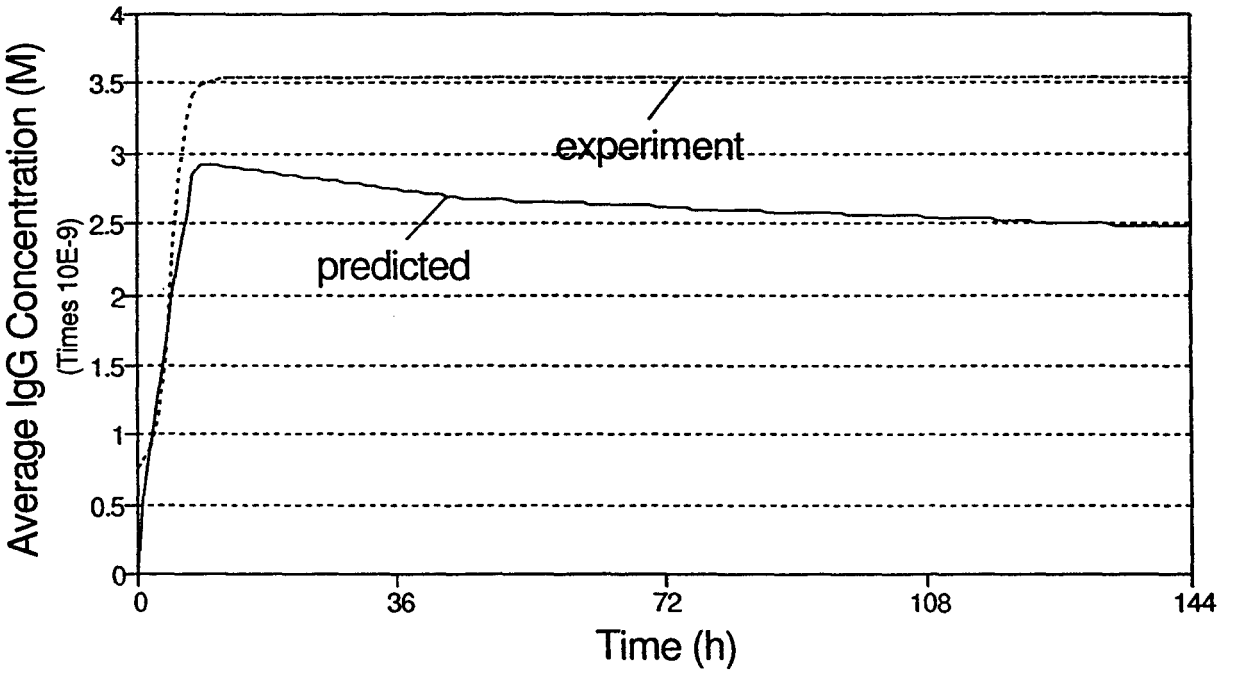

Fig. 4.21 The experimentally determined (dotted line) total IgG uptake in human ovarian OVCAR tumours (Kwok *et al.* 1996) and the theoretically predicted one (eqs. 4.15 & 4.16). The binding affinity B_a, and the vascular permeability P_{eff} were assumed to have 32 and 270 times their baselines values respectively, for an R=0.375cm tumour.

of tumours grown for the experiment. The solid line shows the model's prediction. The binding affinity was increased by a factor of 32 and the effective diffusive permeability (P) by a factor of 270 w.r.t. baseline. The vascular volume corresponding to the assumed tumour radius was calculated from the data of chapter 2 and the intravascular amount of IgG was estimated and added to the model prediction (~5% correction). Despite all the above, the model underestimates the measured values. This agrees with the work of Baxter *et al.* (1994) in which they compare a single to a two-pore model incorporated to a pharmacokinetics compartmental model and finds that in the former, the permeability-surface areas product (PS) and the binding rate constant (k_f) acquire unusually high values to fit the experimental data. The inadequacy of the source term must also be a contributing factor. Fig. 4.22 shows the respective results for the Fab' fragment. The span of the time axis is only 48hr here because of the faster clearance of the Fab fragment making it hard to obtain experimental data at later time points. In this case, k_f was increased by a factor of 2.5 and P by a factor of 12. The latter implies that one needs not increase the permeability as much for Fab' to get a good match with experiment which is misleading (see section 4.3, part 3). The baseline value (Gerlowski & Jain 1986, $P=14.9\times10^{-6}$ cm/sec for Fab) is significantly higher than the one proposed by Fujimori *et al.* (1989, $P=10^{-6}$ cm/sec). Although neither of them when used in the present model predict the total tumour Fab concentration values or time profile accurately, the latter (fig. 4.23) gives a better qualitative agreement in the relative concentration magnitudes w.r.t. IgG as measured in experiment. The $F(ab')_2$ always has a lower concentration than IgG (e.g. Vogel *et al.* 1993), for the same initial plasma concentration. The Fab has a higher concentration than IgG only in the first ~72hr, which is a time scale overestimation. In the work by Kowk *et al.* (1995) the latter was observed only in the first ~18hr. The P values proposed by Gerlowski and Jain (1986) do not result in such relative concentration profiles, as they predict the bound Fab concentration to be higher than the IgG one at all times (fig. 4.18).

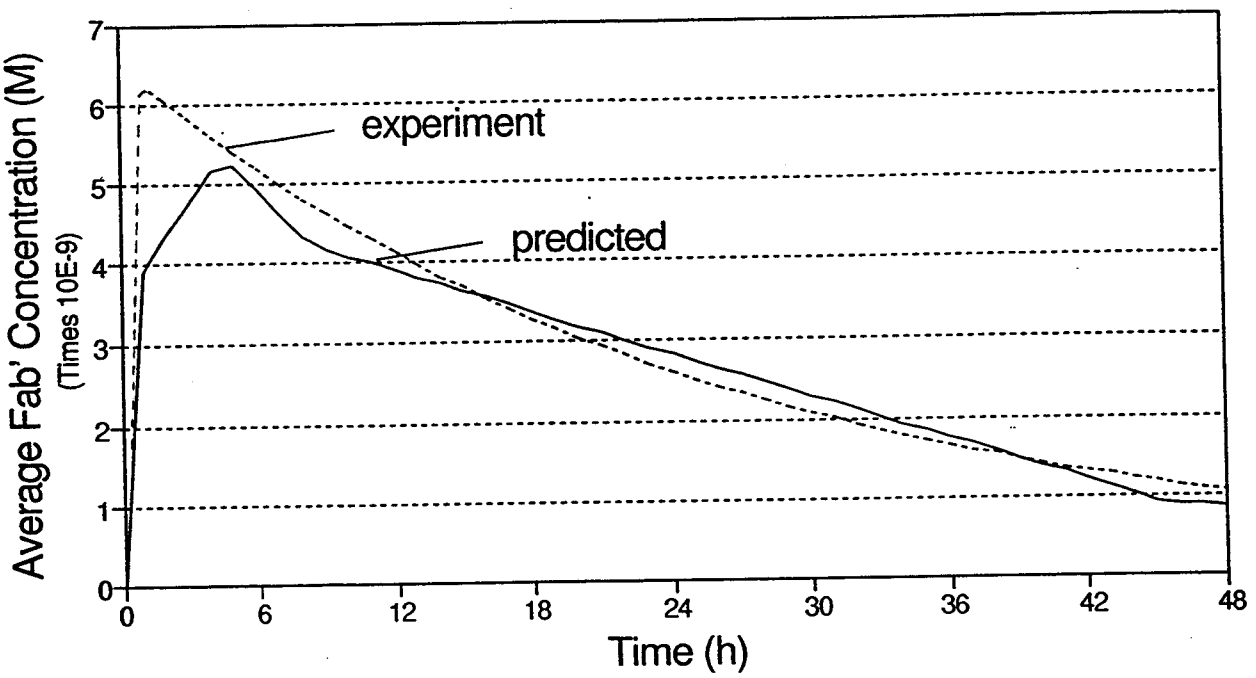

Fig. 4.22 The experimentally determined (dotted line) Fab' average concentration in human ovarian OVCAR tumours (Kwok *et al.* 1996) and the theoretically predicted one (eqs. 4.15 & 4.16). The association rate constant k_f, and the vascular permeability P_{eff} were assumed to have 2.5 and 12 times their baselines values respectively, for an R=0.375cm tumour.

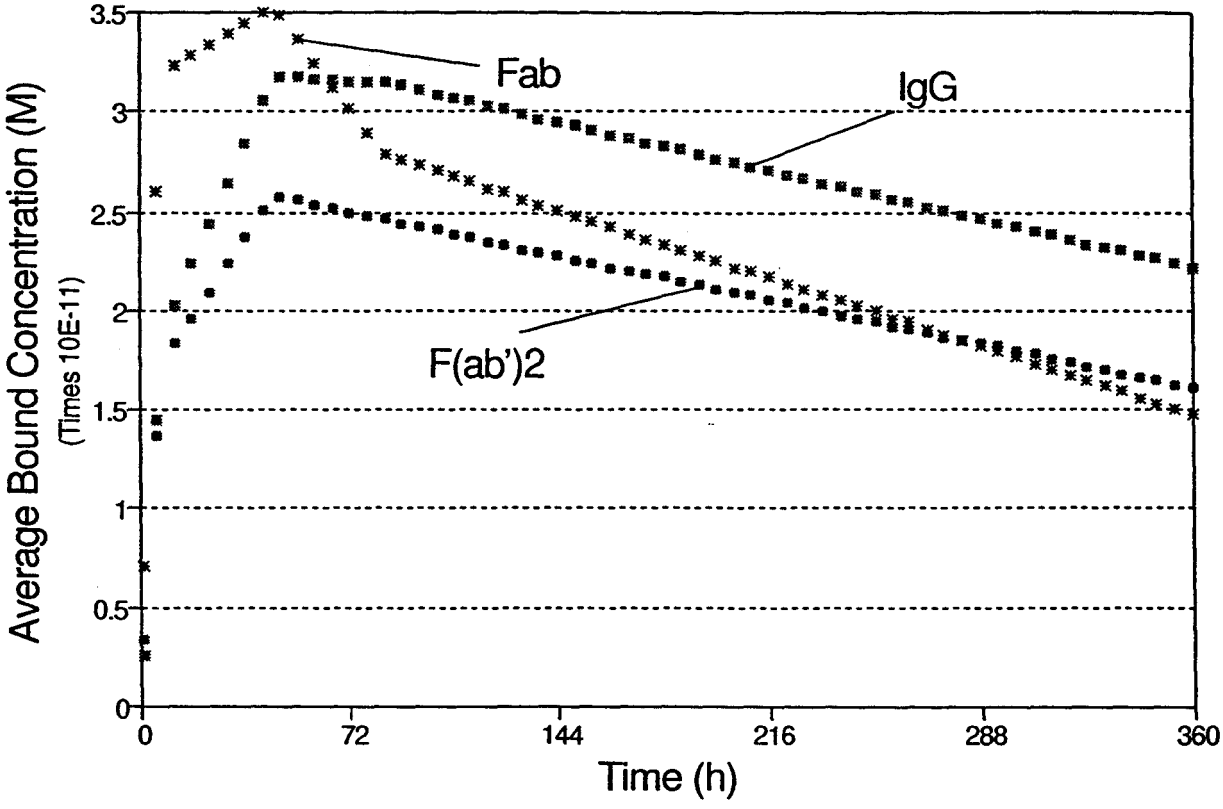

Fig. 4.23 The theoretically predicted average over a R=1cm tumour of the total bound IgG (light-filled squares), Fab'$_2$ (dark-filled squares), and Fab (asterisks) in a using the P_{eff}'s proposed by Fujimori *et al.* 1989.

PART IV: A COMPUTATIONAL TOOL DERIVING TUMOUR VASCULAR DISTRIBUTION PARAMETERS

5. A Proposed Method for the Determination of the Radial Variation of Vascular Volume and Vascular Surface Area per Unit Volume of Tumour.

The predictions of the models presented in chapters 3 and 4 rely heavily on a large number of physiological parameters including the radial variation of vascular area per unit volume of tumour S/V (section 3.1). However, since there is no available data in the literature for S/V this chapter proposes a method for its determination and the measurement of the radial variation of vascular volume per unit volume of tumour $V_a(\rho)/V$. The relevant computational tools have been developed and tested.

5.0 An Algorithm for 'Peeling' an Arbitrary Convex Object.

Solid tumours and their vascular trees have widely varied shapes. On the other hand, the formulation of the transport of macromolecules in solid tumours in the last two chapters assumed spherical tumours and radial symmetry in their physiological parameters. One of the parameters, which was actually assumed to be a constant in the initial work by Baxter & Jain (1989), $S(\mathbf{r})/V$. Since IgG does not travel far from the vessel wall once it extravasates (Juweid *et al.* 1992), the actual vascular distribution plays a key role in determining the spatial inhomogeneity of extravasated macromolecule.

In the hope of avoiding unsurmountable mathematical and computational complexity for an arbitrarily shaped convex tumour, but retaining the important features of the spatial variation of macromolecule perfusion, a radially symmetric $S(\rho)/V$ was proposed and an algorithm for deriving this function was developed. The algorithm constructs a surface inner to that of the tumour by moving vertically inward from each point on the tumour by the same distance, thus creating a 'peel' of uniform thickness. The average radial distance of each 'peel' from the centroid of the tumour is ρ. $\Delta V_a(\rho)$ and $\Delta S(\rho)$ falling between the two surfaces are then computed and divided by the tumour volume ΔV they define. If the procedure is repeated for several consecutive surfaces, continuous functions for the radially symmetric V_a/V and S/V can be fitted to the discrete points. A brief description of the algorithm is given here.

(i) On input the surface of the tumour is represented as a discrete set of (x,y,z) coordinates of points. The origin is the centroid of this set of points which is very close to the actual surface centroid if a large enough number of them is included in the set. Hence, an arbitrary origin needs to be chosen first to assign coordinates to the selected surface points. Then, the centroid can be computed and the surface points recalculated w.r.t. it. Small FORTRAN codes that can perform this task plus the conversion of the input cartesian coordinates to spherical polars were written, and used as calling subroutines in the main 'peeling' code.

(ii) The next step in the algorithm is to interpolate between points on the tumour's surface. For this purpose, subroutine SPHERE (Dierckx 1993) is called. It determines a smooth bicubic spherical b-spline approximation $s(\theta,\phi)$ to a given set of input data points (r,θ,ϕ). An option was chosen where the number of knots in each direction and their position are chosen automatically by the routine. The smoothness of $s(\theta,\phi)$ is then achieved by minimizing the discontinuity jumps of the derivatives of the spline at the knots. There is a tradeoff between the smoothness s_0 and the closeness of the fit. In the current application one wants to preserve the irregularities of the tumour's surface and so s_0 is set to zero. However, this increases the number of knots and computation time considerably. The values for all parameters, RAM space required by SPHERE, and other developed subroutines to be described below are declared in this part of the program.

(iii) Once the tumour's surface has been approximated by $s(\theta,\phi)$, it is possible to compute r for any (θ,ϕ). Subroutine BISPEV (Dierckx 1993) is used to evaluate $s(\theta,\phi)$ on a regular θ, ϕ grid. Using regular grids is advantageous because the code complexity and computation time required by SPHERE and BISPEV are reduced. Also, this is the only way to visualize the surface as a mesh plot in many commercially available graphics packages.

(iv) The partial derivatives of $s(\theta,\phi)$ w.r.t. θ and ϕ, $\partial s/\partial\theta$ and $\partial s/\partial\phi$ at the grid points defined in (iii) are evaluated using subroutine PARDER (Dierckx 1993). The convex surface approximated by $s(\theta,\phi)=r$ can also be expressed as $F(x,y,z)=0$. Hence, the cartesian partial derivatives of F were computed using the relevant Jacobian transformations and the calculated values of $\partial r/\partial\theta$ and $\partial r/\partial\phi$ from PARDER for each θ,

ϕ pair.

(v) Once the partial cartesian derivatives of F at (x,y,z) are known, all three direction cosines cosα, cosβ, and cosγ of the normal to the surface can be found. From Courant (1936, p.124):

$$\cos\alpha = \frac{F_x}{\sqrt{F_x^2 + F_y^2 + F_z^2}} \qquad (5.1)$$

Similarly, cosβ has F_y and cosγ has F_z at the numerator. The direction cosines define the unit normal vector:

$$\hat{n} = \cos\alpha\, \boldsymbol{i} + \cos\beta\, \boldsymbol{j} + \cos\gamma\, \boldsymbol{k} \qquad (5.2)$$

One can now define a step of length $|\Delta \mathbf{r}|$ down the normal and define a new coordinate point at $r_2=r+\Delta r$ that could be part of an inner surface. The above procedure is repeated for all (r,θ,ϕ) in the initial data set.

(vi) Each coordinate point of the set created in (v) has to satisfy two criteria before it is considered a valid point of an inner surface:

(1) The new point must not be outside the 'source' surface that created it. The distance $|\mathbf{r}_2|$ of the new point at $r_2(\theta+\Delta\theta,\phi+\Delta\phi)$ from the centroid of the tumour is compared with the radial distance $|\mathbf{r}_1|$ from the 'source' surface that BISPEV calculates for the same $\theta+\Delta\theta$, $\phi+\Delta\phi$ coordinates. If $|\mathbf{r}_2|>|\mathbf{r}_1|$, then the new point is rejected from the data set forming an inner surface (fig. 5.1).

(2) The new point may be inside the surface that created it, but its minimum distance to the latter is less than $|\Delta \mathbf{r}|$. To check that, the coordinate of the new point becomes the centre of a sphere of radius $|\Delta \mathbf{r}|$. It is checked whether the sphere intersects the outer surface. This is done by computing the radial distances from the tumour centroid of points on a regular θ, ϕ mesh on the sphere and comparing them with the ones from the 'source' surface given by BISPEV for the

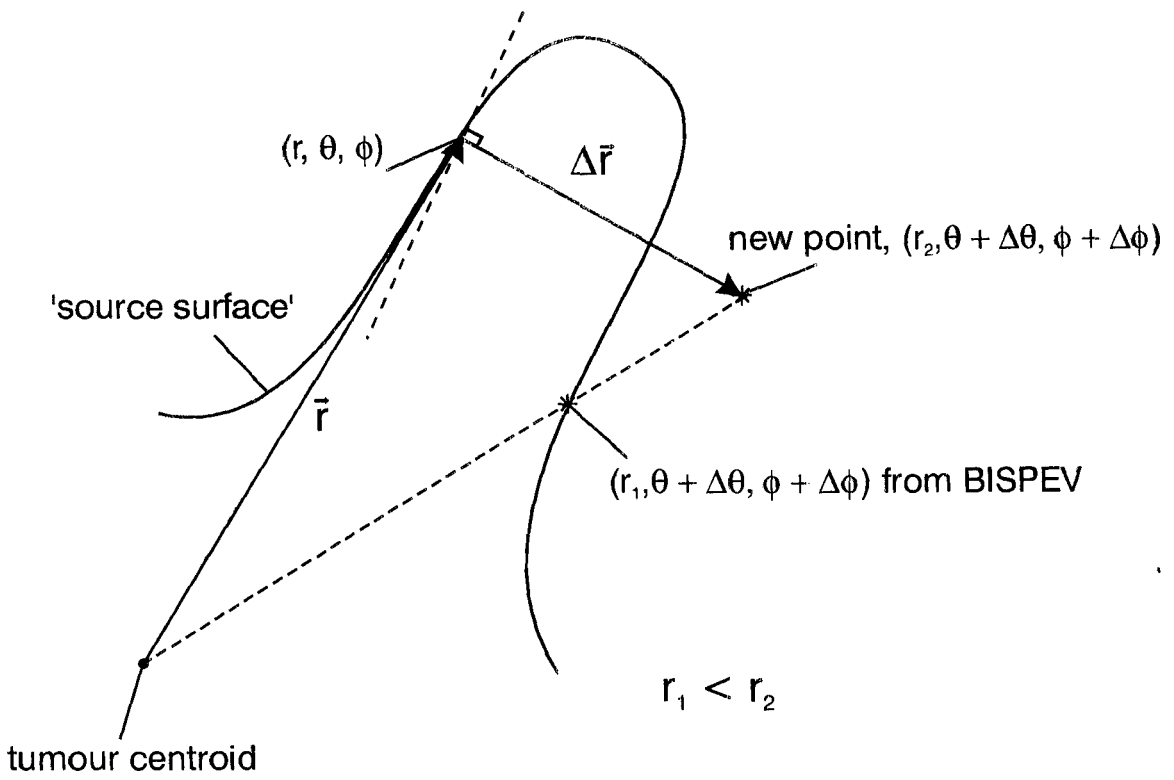

Fig. 5.1 The new point (r_2,θ,ϕ) is outside the 'source' surface that created it, and is an invalid inner surface data point.

same θ, ϕ pair. If the former is larger than the latter, the new point, which is the centre of the sphere, is excluded from the final data set of points comprising the new surface (fig. 5.2).

Step (2) is computationally intensive. If $\delta\theta$ and $\delta\phi$ of the mesh on the sphere are set to 1°, then the program may need a day to run on a VAX 4000 for a tumour surface comprising of 3000 points that have to be checked against the above two criteria. If the intervals are increased to 10°, it only takes half an hour. Hence, there is a compromise between the size of sampling intervals (i.e. the resulting accuracy in the construction of the new surface) and computation time. For reasonably smooth surfaces like an ellipsoid, the above two sampling intervals were tested and it was found that the latter does not affect the accuracy of the final result.

All steps of the 'peeling' algorithm were tested by computing the respective analytical results for chosen ellipsoids. The resulting inner surfaces were smaller ellipsoids having all their principal axes shortened by $|\Delta\mathbf{r}|$ in each 'peeling' step. The 'peeling' of an ellipsoid A with principal axes (1,1,2) in steps of $|\Delta\mathbf{r}|$=0.25 is shown in fig. 5.3. The generated ellipsoids B and C have principal axes (0.75,0.75,1.75) and (0.5,0.5,1.5) respectively.

The algorithm also handles the special case of a perfect sphere where $\partial r/\partial\theta$ and $\partial r/\partial\phi$ are always zero, or when both these derivatives happen to vanish on an irregular surface. In these cases the algorithm assumes that the local curvature is that of a sphere and creates an inner surface point a radial distance Δr towards the centroid of the tumour. If after a 'peeling' step there are no, or very few, points in the output data set the program signals that no further inner surfaces can be generated using the current $|\Delta\mathbf{r}|$ setting. Finally, the format of the output file was made suitable for exporting into a selected graphics package (TECPLOT v.6.0/94, i-j ordered mesh plots) in order to simultaneously visualize several surfaces as in Fig. 5.3. Finally, a subroutine was written that calculates the volume enclosed by the 'source' surface in each 'peeling' step, by integrating the interpolated surface over all solid angles.

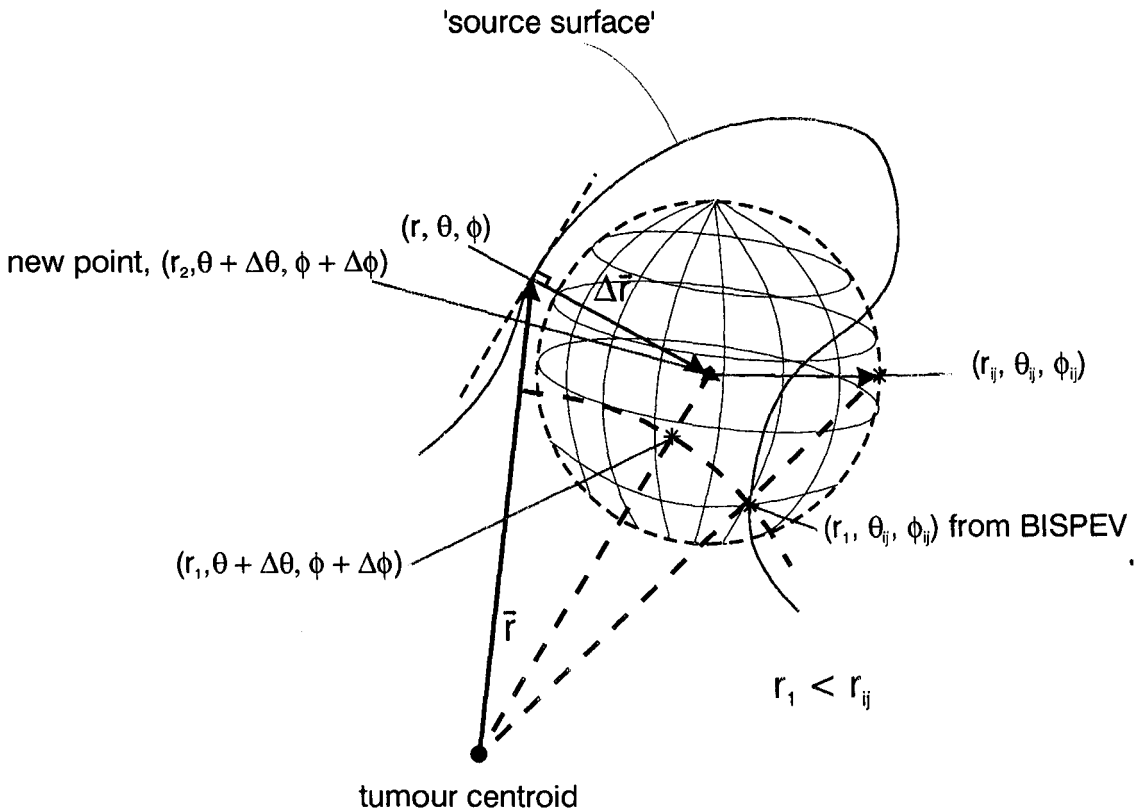

Fig. 5.2 The new point lies inside the 'source' surface. However, if one uses the new point (r_2,θ,ϕ) as the centre of a sphere of radius $|\Delta\mathbf{r}|$ the latter surface intersects the former. This means that there is at least one radial distance $\mathbf{r}_{ij}$ calculated on the regular mesh on the sphere that is larger than the corresponding 'source' surface radial distance for the same θ, ϕ ($r_1 < r_{ij}$). Hence, (r_2,θ,ϕ) is an invalid inner surface point as its minimum distance from the 'source' surface is less than $|\Delta\mathbf{r}|$.

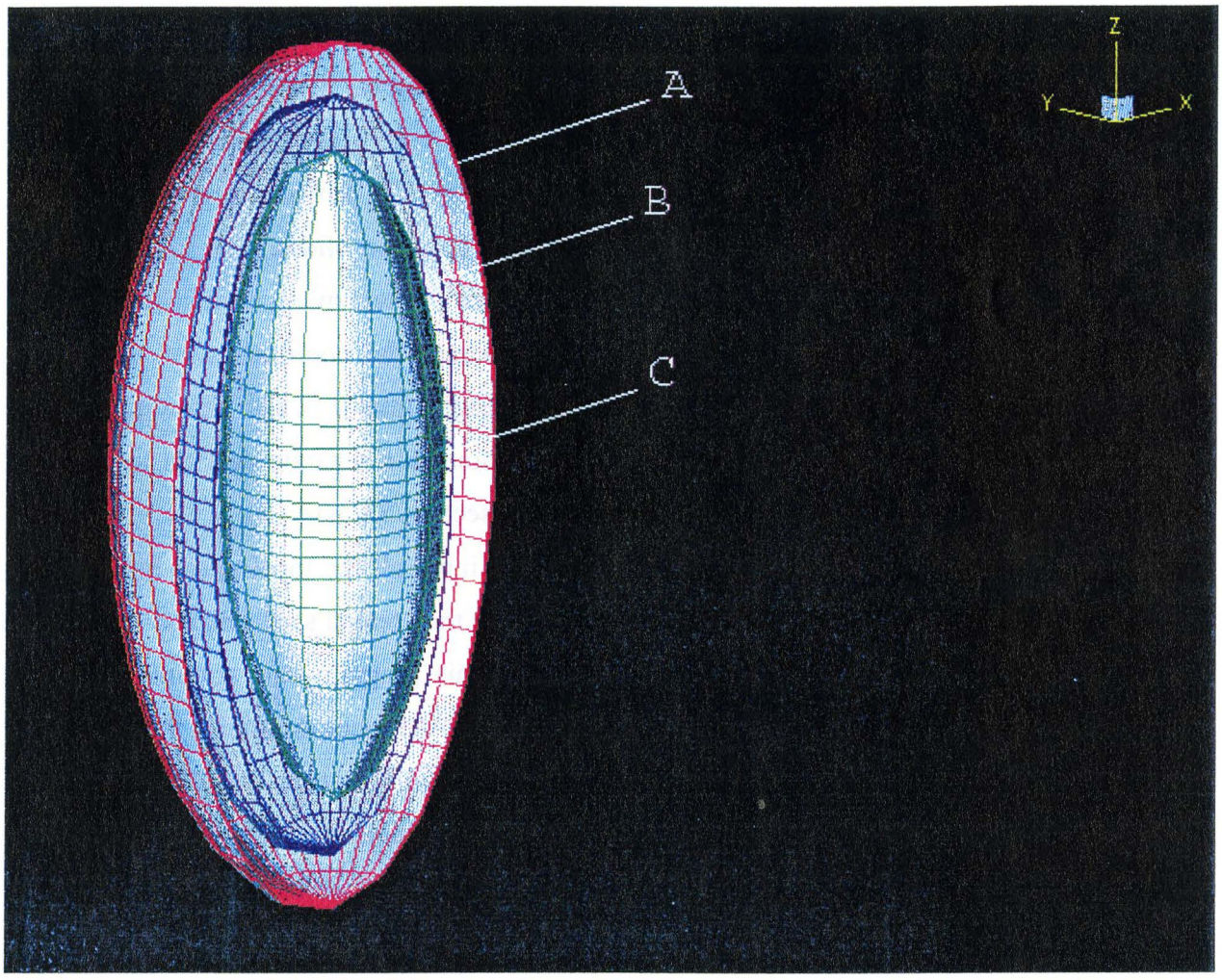

Fig. 5.3 The result of 'peeling' twice an ellipsoid A with principal axes (1,1,2) in steps of $|\Delta \mathbf{r}| = 0.25$, are ellipsoids B (0.75,0.75,1 75), and C: (0.5,0.5,1.5).

5.1 A Proposed Method for the Determination of Vascular Volume and Surface Area per Unit Volume of Tumour.

Once the tumour has been divided into annular zones of uniform thickness, one can record the vascular attributes of interest that fall within each one and deduce the effective radially symmetric distribution for each attribute. To provide experimental input, serial sections of a solid tumour can be cut and fixed on slides. The slides can be captured as digital images on an image analysis system. After having established a global coordinate system for all the slides, one can extract the coordinates of the pixels comprising the area occupied by blood vessels in each slide. It is also essential to store enough coordinate points on the surface of the tumour in a separate data set to produce an accurate surface reconstruction as described in section 5.0 part (ii).

A program has been developed to accept as input all the topological information created by the 'peeling' algorithm, to reconstruct all the created surfaces, and to process the data sets of the selected vascular attributes. This program was not linked to the 'peeling' program because the latter required a lot of RAM space to process the large data sets of coordinates. The radial distance from the centroid to each voxel of the blood vessels is evaluated and is compared with the radial distances of any two consecutive surfaces for the same θ, ϕ values calculated using subroutine BISPEV. If the voxel radial distance falls between the two surfaces, then that voxel is added to the number counted in the zone enclosed by them (e.g. A and B in fig. 5.3). Since voxel volume is the product of slice thickness and pixel area, the vascular volume in each zone is the sum of the voxel volume of all enclosed voxels. BISPEV was called to calculate the radial distances of any two consecutive surfaces on a regular mesh of θ, ϕ values, and therefore the average radius of the zone defined by the two surfaces. Also, the volume of the zone can be calculated by subtracting the total volumes enclosed by its upper and lower surfaces as computed in the last step of the 'peeling' program. Dividing the total vascular volume in a zone by its volume gives the vascular volume per unit volume of tumour tissue for the calculated average radius. By repeating the procedure for all consecutive surfaces, one can obtain a continuous fit to the discrete points for the vascular volume

density vs. average radial distance from the centroid of the tumour.

The surface area of the vessels in the vascular tree can also be estimated. In the same serial tumour sections one should select and record all the pixels comprising the periphery of vessels that appear to run perpendicular to the surface of the slide. There are routines available in all image analysis systems that allow one to obtain the centroid and mean radius r_m of each of the selected vessels. Vessels that appear to run parallel, or at an angle to the plane of the slide are not included in the calculation of r_m which may affect its estimation. Selecting all the vessels running perpendicular to the slide is subjective to the user of the image analysis system. The latter is a shortcoming of the method. However, if a large number of vessels is selected the resultant error in r_m should not be large. Using the same volume exclusion algorithm described at the beginning of this section, one can assign the centroids of the vessels in a zone of average radius ϱ. Hence, a two dimensional frequency distribution function $F(\varrho,r_m)$ can be obtained. One can evaluate the average $<r_m>$ of r_m for each zone, by taking the mean of each $F(\varrho=\text{const.},r_m)$ slice, and so calculate $<r_m>$ as a function of radial distance from the centroid of the tumour. The discrete function can be fitted to a continuous one ($<r_m(\varrho)>$). Since the surface of a cylindrical tube of radius r and length L is $S= 2\pi rL$ and the volume is $V_a= \pi r^2 L$, the total vessel surface area $S(\rho)$ in a zone of radius ϱ is:

$$S(\varrho) = \frac{2V_a(\varrho)}{<r_m(\varrho)>} \qquad (5.3)$$

where $V_a(\varrho)$ is the vascular volume as a function of zone radius calculated in the last paragraph.

Finally, one can obtain the vessel surface area per unit tumour volume by dividing $S(\varrho)$ by the volume V of each zone of that average radius ρ. This will produce a discrete function $S(\varrho)/V$ that can be fitted to a continuous one. The latter would provide the suitable input parameter for the model analyzed in chapters 3 and 4.

5.2 Limitations of the Method.

The following factors are likely to be the ones limiting the accuracy and ease of implementation of the method:

(i) It is known from physiology (e.g. Tortora & Grabowski 1993, p.630) that the largest contribution in vessel surface area for trans-vessel exchange in the cardiovascular system comes from the capillaries. The diameters of fenestrated capillaries in healthy tissue range from 70 to 100nm (*ibid.* p.628). It is also a common experimental observation that capillaries are the dominant form of vessel permeating viable tumour tissue and have diameters similar in magnitude with the healthy ones (e.g. Hilmas & Gilette 1974). On the other hand, one may find arterioles, or venules in a tumour especially near its surface. Their diameters range from 5-15μm for the former (Williams & Warwick 1980, p.625) and 20-30μm for the latter (*ibid.* p.629). This means that in trying to record the coordinates of all vessels of a tumour on an imaging system, one may have to combine information from images at different magnifications. One will also need to develop appropriate software to correlate the coordinates of selected objects in an image at high magnification to their global coordinates e.g. w.r.t. the tumour's centroid.

(ii) Another aspect of data acquisition of blood vessel coordinates is the storage memory space required for this information. The memory could easily reach the order of Gbytes for a 0.5cm tumour due to the vast number of capillaries in it, and their convoluted geometry. This also increases considerably the computation time and RAM required by the data processing algorithms.

(iii) In order for one to achieve a moderately accurate reconstruction of capillaries, the tumour slices should be a few microns thick. Thus, the making of the slides and their processing on an imaging system becomes a work intensive procedure. For example, a 5mm tumour produces 10^3 5μm thick slices. Combined with the anticipated memory and computation time problems mentioned above in (ii), this limits the method to tumours of at most 1mm diameter for computers with a 20 Gbyte RAM memory. For larger tumours one can only take random samples of the slices to process and apply statistics to estimate

the uncertainty of the measured vessel parameters (Hilmas & Gilette 1974). However, in doing that one may lose the spatial distribution information about these parameters.

(iv) If one is interested in simultaneously determining the spatial distribution of an injected labelled macromolecule for a given vascular distribution, the above method is invasive and provides a single time point in the observed macromolecule distribution. On the other hand, there is no available medical imaging modality (e.g. CT, PET) that has the spatial resolution required to do the above non-invasively. Efforts have been made to develop efficient 3D reconstruction algorithms of vascular distributions from a small number of projections (Peters & Henry 1996). Their results are encouraging in applications like angiography that has a spatial resolution of ~1mm. The algorithms can presumably be applied to capillary trees too if a medical imaging modality ever offers the required resolution.

(v) A marker specific to endothelial cells is required to facilitate the selection of the blood vessels in an image. It should not cross-react with any tumour cell antigens, connective tissue, or RBC's in the lumen as that would obscure the selection of the desired objects in the image. In order to make the colour threshold of the target features more distinct, the markers could be conjugated to a fluorescent dye (e.g. FITC). The images can then be captured on a fluorescence microscope before bleaching occurs. There are several good human endothelial cell markers (e.g. CD31, p-selectin). However, since experiments are done on animals, the endothelial cells are those of the host. Endothelial cell markers for other species are not as readily available in preparations for immunohistochemical staining.

(vi) The estimation of $S(\varrho)$ in the method above relies on selecting all the vessels that appear to run perpendicular to the plane of the tumour slice. Doing this by eye will lead to some error, as there is no way that one knows if a vessel runs exactly perpendicular by looking at a single slice. This will inevitably lead to some error in the estimation of $\langle r_m(\varrho) \rangle$ (eq. 5.3), although when averaging small random deviations from the true normal in a large number of vessels, the error may partially be compensated. A more accurate estimation of $\langle r_m(\varrho) \rangle$ can be made if one considers the coordinates of the same vessel on adjacent slices. A simple algorithm can be developed that calculates the vector along

which each capillary runs relative to the normal to the plane of each tumour slice. Then, by projecting the computed normal of the effective cylindrical section to the normal of the tumour slice for each vessel, one can derive a more accurate aggregate value for $<r_m(\varrho)>$. This method however, is computationally intensive.

(vii) Possible irregular details of the tumour surface, like sharp corners, will be rounded off by the interpolation algorithm. Good fitting in areas with rapid curvature changes requires higher order b-splines. If the surface is concave in parts, it is possible that after one or more 'peeling' steps, the created inner surface will be separated in two or more disconnected 'peels'. A vascular attribute counted in both 'peels' corresponding to the same distance from the surface of the tumour, are then added up to form a single data point in the effective radial function of that attribute. The developed algorithm does not have a check for local curvature changes to do the coordinate separation and vascular attribute addition steps automatically. Instead, they have to be done by the user in each 'peeling' step thereof.

(vii) Structural knowledge of the vascular tree in a tumour yields no information about the local variations in vascular permeability. The latter needs to be determined by an independent method in conjunction with the one presented here.

It should be said that an advantage of the method is its generality. The topological information it can extract may apply to other organs (e.g. kidney, spleen). However, if one wants to link this information with mathematical predictions for a drug distribution in the latter, one also has to consider the unique physiological conditions in each one which are very different from those in tumour.

PART V: SUMMARY AND RECOMMENDATIONS FOR FUTURE WORK

6. Conclusion

The theoretical and experimental results obtained in this project as well as the limitations used to derive them, were discussed in detail at the end of the relevant chapters. Here, a brief summary of conclusions for the project is outlined for quick reference. A section with recommendations for future work is also included.

6.0 Summary of Conclusions

A. The Nude Mouse Model

Following the method proposed by Song & Levitt (1970):

(i) The total vascular volume of individual SKOV3ip1 human ovarian tumours grown in nude mice was quantified.

(ii) The total plasma fluid extravasation rate in each tumour was quantified.

Linear correlations of (i) and (ii) with tumour weight were found, with coefficients of correlation equal to r=0.955 for the former and r=0.948 for the latter, implying rapid angiogenesis in pace with tumour growth. The fit was somewhat worse for (ii) than (i), implying a variability in the average vascular permeability between tumours of the same type. The SKOV3ip1 xenograft model in nude mouse did not show any appreciable necrotic core even for about 1g size tumours.

B. The Interstitial Fluid Pressure and Velocity Spatial Distributions in Tumours.

A mathematical model proposed by Baxter & Jain (1989) was examined and expanded to include a radial variation of the average vascular surface area per unit volume of tumour tissue (S/V).

(i) The analytical solutions for the steady state interstitial fluid pressure and velocity distributions for a well perfused tumour, and one having an arbitrary size necrotic core were calculated. The results found were different from the published ones which are incorrect.

(ii) Computational methods were developed to calculate the fluid distributions in (i)

numerically and good agreement was found with the calculated analytical solutions reported in this thesis.

(iii) Computer codes were developed to include the case of a radially variable S/V distribution, for which, a general analytical solution of the equations does not exist. The interstitial fluid pressure and velocity profiles were calculated for a variety of S/V radial distributions. It was found that the profiles were not very sensitive to the numerical values of S/V, or to the size of the necrotic core except for extreme cases. This is because plasma fluid floods interstitial space creating a pressure build-up which suppresses transcapillary convective transport under steady state conditions.

(iv) The model predicts that there is a narrow region near the tumour surface where convective transcapillary transport of plasma fluid occurs into the tumour interstitium and a central region where only diffusive transport occurs because of the fluid pressure build-up. This is supported by experimental evidence of Peterson *et al.* (1994). The model also predicts that the tumour size affects the interstitial pressure plateau value only for radii up to $R \approx 0.2$cm. Larger tumour radii give interstitial pressure plateaux of larger spatial extent without an increase in the pressure values. There is no direct experimental evidence to verify this.

(v) The value of the total fluid extravasation rate (0.41 ml/g/hr) predicted by the mathematical modelling on the SKOV3ip1 tumour in nude mice compared well with the experimentally measured value of (0.50 ± 0.26 ml/g/hr).

C. The Spatial and Temporal Macromolecule Distributions in Tumours.

A mathematical model by Baxter & Jain (1989,1990,1991a) predicting the spatial & temporal distributions of IgG, $F(ab')_2$, and Fab macromolecules in tumours was examined. The model was expanded to include a radially variable S/V as in (B) above. The relative importance of a number of physiological parameters in optimizing delivery was investigated.

(i) The proposed equation for non-binding macromolecule has no analytical solution and computational methods were developed to obtain a numerical solution.

(ii) Computational methods were also employed to solve the transport equations for

binding macromolecules.

(iii) The spatial distributions in tumour and surrounding normal tissue for the three macromolecule types, binding and non-binding ones, were obtained. The cases of well perfused tumours, tumours with specified necrotic core sizes, and tumours with different types of S/V radial distributions were examined.

(iv) The sensitivity of the overall tumour perfusion to variation of the macromolecule m.w., binding affinity and metabolism, S/V, tumour radius, and microvascular permeability was investigated. It was found that:

iv.(1) The microvascular permeability is an important factor in modulating the macromolecule perfusion in tumour. The increase in the vascular permeability leads to a small increase in the pressure built-up opposing the extravasation of plasma fluid. The simulations, however, also showed that increasing the microvascular permeability (P) leads to an increase in macromolecule uptake. The latter cannot be correlated with the increase in the plasma fluid extravasation rate because of the lack of a pore theory formulation linking the relevant physiological parameters. It was also found that matching the predicted tumour uptake of intact IgG, and its fragments with experimental observations (e.g. Kwok *et al.* 1996) requires assigning appropriate values to the microvascular permeability (P).

iv.(2) The binding affinity not only increases the amount of macromolecule uptake, but also the inhomogeneity of its distribution until saturation of binding sites occurs. Hence, macromolecule binding affinity and the homogeneity of its distribution are two competing factors in the optimization of immunotherapy. This phenomenon known as the 'binding site barrier' has been reported by other investigators too (e.g. Juweid *et al.* 1992).

iv.(3) The baseline value of binding affinity results in a lot higher bound macromolecule concentration in tumour than the free one for realistic plasma concentrations.

iv.(4) Metabolism reduces the amount of bound macromolecule and also the inhomogeneity of its distribution. The latter occurs because in the mathematical modelling it is assumed that an antibody-antigen complex is instantaneously internalized and processed and the antigen is presented again at the cell's surface and so, a smaller percentage of the extravasated macromolecule is available to perfuse areas away from

capillaries.

iv.(5) An increased tumour radius decreases the average macromolecule uptake per gram of tumour tissue, because it increases the percentage of its volume where the maximum pressure build-up suppresses convective transport.

iv.(6) The molecular weight of the macromolecule determines its extravasating rate, as well as the distance it travels away from the capillaries. As a general rule, the lower m.w. fragment both extravasates and clears away faster than the intact IgG. Except for early times, the former will be present at lower quantities than the latter, and will always have higher tumour to blood ratios. The spread of the fragments into less well perfused areas is marginally higher than the intact IgG. The higher m.w. of intact IgG inhibits it from travelling far into the tumour interstitium, but also prevents it from washing away back into the circulation, thus creating a 'reservoir' effect at long times after infusion. This is supported by all tumour uptake quantitation experiments (e.g. Vogel *et al.* 1993).

iv.(7) The actual form of the vascular distribution represented by the radial distribution of S/V plays a dominant role in determining the heterogeneity of the macromolecule distribution, as all the three macromolecule types do not travel far from the area where they extravasated.

(v) The following limitations of the mathematical model examined were found:

v.(1) The numerical solutions of all macromolecule transport equations were mildly numerically unstable. This indicates a possible problem with the formulation of these equations and/or the boundary conditions.

v.(2) The predicted interstitial pressure profiles are steeper than the ones measured in vivo (Jain 1987). This is attributed to the uniform averaging of physiological parameters, including the vascular distribution, over the whole tumour and their abrupt change at the tumour-normal tissue interface.

v.(3) Several physiological parameters related to fluid and macromolecule transport including L_p, σ_T, σ, and P, as defined in chapter 1, are intuitively related via the pore model description of transcapillary transport. However, there is no formulation linking them at present, and they appear as independent parameters on input. This makes the

estimation of their impact on macromolecule transport during sensitivity analysis difficult.

v.(4) A two-pore formalism is more appropriate in describing capillary permeability. The single-pore one was found to grossly overestimate the value of the microvascular permeability (P) in order to match the experimentally observed macromolecule uptake in tumour from the work of Kwok *et al.* 1996. This is supported by Baxter *et al.* (1994).

v.(5) There is a lack of accurate values for most physiological parameters needed in mathematical modelling. Values obtained from in vivo and in vitro experiments in different species, including humans, were agglomerated to simulate the macromolecule uptake in human tumours.

v.(6) The effects of spatial heterogeneity of the vascular distribution, the presumed discrete distribution of pores along a capillary, and capillary-capillary interaction are absent from the model. It is difficult to estimate the effect of these factors on macromolecule transport.

D. A Method for Quantifying the Radial Variation of Vascular Density and S/V of Arbitrary Shape Convex Tumours.

The computational tools needed to calculate effective spherically symmetric distribution functions for the vascular density, and S/V from serial tumour sections were developed. This allows input of such experimental data in an expanded version of the formulation of the macromolecule transport, which include S/V. The tools include:

(i) An algorithm for interpolating the surface of an arbitrary shape convex object and 'peeling' it into zones of uniform thickness.

(ii) Computer programs to determine the vascular density and S/V effective spherical distribution functions using the tumour surface and the resulting consecutive 'zones' defined in (i) as input.

The developed computer codes were successfully tested in 'peeling' ellipsoids of different principal axis ratios. Lack of knowledge of the variations in vessel permeability for a given vascular tree, and the large amounts of computer memory and computational effort incurred by the size and complexity of the vascular tree, are the main limitations of the method.

6.1 Recommendations for Future Work

The following ideas for future experimental and theoretical work in the area of macromolecule transport in tumours emerged as a natural sequel of the methods studied and developed in this project.

(1) A more detailed formulation for the spatial distribution of the source term $\phi_S(r)$ (eq. 4.3) in a tumour is needed. Averaging out the source term in every volume element of the tumour overestimates the interstitial pressure build-up. Consequently, the percentage of the tumour volume where convective transport occurs is underestimated. The above also results in a pressure gradient at the tumour's surface steeper than experimentally measured values (Jain 1987). It is proposed that a new distributed model is developed in which the tumour volume is divided into cubic elements. The tumour blood vessels can then be represented as consecutive cubic source elements each following the physics of $\phi_S(r)$, but at the same time approximating the spatial structure of an actual vascular tree. The remaining tumour elements representing the extravascular space can be assigned the relevant macromolecule transport parameters through a porous medium, estimated from experiment. The boundary conditions at the tumour interface with normal tissue will then be adjusted to continuity of both fluid and macromolecule fluxes and concentrations for the 'porous medium' elements and to continuity of blood flow for the source elements. This should help eliminate the numerical instability observed at the tumour's surface. The cubic element approach has the potential for high versatility, describing macromolecule transport in tumours of any shape. This will allow a better insight into the macromolecule perfusion of real-life vascularized tumours.

(2) A physical description of L_p, σ_T, σ, and P, as defined in chapter 1, is required in terms of the pore size(s) of capillaries and other relevant physiological parameters. This will allow one to vary the pore size(s) and calculate the relative changes in the above parameters which currently appear as independent input parameters to the model. This will illustrate whether a vasodilator will help increase tumour perfusion with macromolecule. More specifically, it will show whether the increase in P and the decrease in σ, helps increase the macromolecule perfusion of the tumour despite the inevitable

simultaneous increase in interstitial pressure suppressing convective transport because of the increase in L_p and the decrease in σ_T. The basis for such a formulation has been laid by Curry (1984). The shortcoming of developing a detailed physical description of these parameters is a need for more parameters, like the plasma fluid viscosity. The values of these parameters in vivo can only be roughly estimated. The needed formulation linking L_p, P, and the σ's goes beyond the identification of some fundamental physical parameters in terms of which they can be defined. The formulation also includes a non-linear weighting function which takes into account the geometry of the pore and the solute, as well as its concentration and net charge. Curry (1974) developed such an expression for a dilute, neutral spherical solute through a rectangular slit. A lot more work needs to be done for non-spherical solutes and/or more concentrated solutions, where solute-pore and solute-solute interactions remain largely unevaluated. The complex behaviour of flexible macromolecules through fine pores is also not well understood.

Once progress in this area has been achieved, a rigorous parameter analysis should be performed by varying the value of each parameter, or combinations of them, for continuous ranges of values and looking at their impact on the tumour uptake as a function of time.

(3) A non-invasive method to measure transport parameters of plasma fluid and macromolecules in vivo in the vicinity of an isolated capillary is required. Examples of such parameters are the hydraulic conductivity of the vessel wall L_p, and the velocity of fluid through the vessel wall pores. This may also lead to an indirect estimation of P and the σ's as discussed in (2) above. The method to determine these parameters may involve measuring the rate of spatial expansion of a tracer dye out of a capillary. It may be an improvement of the intravital microscopy method proposed by Kaufman & Jain (1991). There are two main purposes for which such a method is needed:

(a) There is currently no non-invasive way of measuring plasma fluid pressure gradients near a capillary wall. This is mainly because of the microscopic scale of the capillary system. The only currently available way of measuring the interstitial pressure in vivo is with a needle pressure transducer piercing the tissue, thus obtaining an average value for a surrounding tissue volume element. The very small difference of this pressure

with atmospheric and the fact that the needle damages the tissue where the measurement is performed have cast doubt on the results of the method. Hence, it is obvious that this method cannot yield the sensitivity and spatial resolution required for the measurement of near-capillary pressure gradients. The lack of such information has prevented knowledge of the relative importance of diffusion and convection in transcapillary transport of molecules. It has also reduced the quality of other parameters like P_{eff} and D_{eff}, measured in vivo by Gerlowski & Jain (1994), as they were forced to assume pure diffusive transport in order to fit model parameters with experimental observations. It should also be mentioned that a value of D_{eff} in tumour necrotic tissue for any kind of macromolecule does not exist in the literature.

The non-invasive method could also be used to quantify the transport of fluid and macromolecules at the tumour-normal tissue interface. There are no experimental measurements of the pressure gradients of interstitial fluid in that region, which determine the amount of washing-out of macromolecule into the normal tissue. The spatial extent of neighbouring normal tissue lymphatics into the tumour tissue and their effect on local pressure gradients also have to be determined. It is also not known to what spatial extent the normal blood vessels providing blood supply to the tumour retain their normal physiological properties in the tumour tissue, and how that affects the pressure gradients at the interface.

(b) If the method has adequate spatial resolution, it will help determine the actual physical mechanism represented by the 'pore' model. The 'pores' may be gaps between endothelial cells, or effective vesicular pathways through them.

It is not clear whether the bulk of plasma fluid transport occurs through the same interendothelial gaps that the bulk of macromolecule transport occurs. Furthermore, it is not known what percentages of the total transcapillary transport rates of different plasma proteins , or injected macromolecules of different m.w.'s and net charges, occur via the vesicular transport pathway. The influence of the tracer on the tracer-tagged molecule on transcapillary transport is another related issue. Moreover, it is not known whether the fibre matrix of the capillary basement membrane filtering transcapillary flow is more important than the size of the interendothelial gaps in determining the macromolecule

extravasation rates.

(4) The two-pore theory of transcapillary exchange by Rippe & Haraldsson (1987) has only been applied to compartmental models in which the tumour is a black box. Baxter *et al.* (1994) showed that a compartmental model incorporating two-pore theory gives a better fit to experimental data of bulk macromolecule uptake in tumour. This above strongly suggest the advantage of a two-pore theory in a 'distributed source' model such as the one studied in this project where it was found that a single-pore model grossly overestimates capillary permeability. The only problem is the lack of accurate knowledge of values for the small pore (σ_S) and the large pore (σ_L) protein reflection coefficients and their respective weighting factors (α_S,α_L) that the new formulation introduces.

If at some point in time it is proved that it is the size of the of the interendothelial gaps that dominate transcapillary transport rates in tumour, it may be useful to obtain pore-size frequency distributions experimentally for arterioles, capillaries post-capillary venules, and lymphatics e.g. by studying samples of these vessel walls by electron microscopy. This will allow the formulation of a multi-pore theory to explain blood vessel permeability more accurately, and also show to what extent the two-pore simplification is satisfactory.

(5) The spatial distribution of capillaries and the blood flow through them has been studied by a large number of researchers, but only for small tumour tissue segments (e.g. Rijken *et al.* (1995). Capillary permeability has also been studied for individual vessels (Gerlowski & Jain 1994), or as an average over the whole tumour (e.g. Song & Levitt 1970). However, information on all the above parameters has never been simultaneously collected over a whole tumour. Strictly speaking, this is an almost impossible task, but there is still a lot of room for improvement in developing experimental methods to collect such data as a function of time and space within the tumour volume, as well as development of algorithms to automate data collection and processing. The above, together with the clarification of questions on the physical mechanism of transcapillary transport discussed in (3) will help explain the apparent lack of correlation between vascular volume, the permeability-surface area product (PS), and blood flow in tumours (Peterson *et al.* 1984).

The 3D spatial distribution of the capillary tree could be correlated to blood flow by modelling the former as an electronic circuit, with each branch represented by an Ohmic resistance equivalent to the hydraulic resistance to blood flow of that branch. Circuit analysis can then correlate sample pressure measurements in capillaries and venules to the measured blood flow rates at the same sites. This will enable one to simulate the effect of a vasodilator, or a vasoconstrictor on the spatial-temporal variation of blood flow within the tumour, as well as the 'shunting' of blood into the surrounding normal tissue if its resistance is lower. A rudimentary kind of modelling of this type has been done by Zlotecki *et al.* (1995). These results may further be correlated to local measurements of tumour tissue interstitial pressure to provide a link between the spatial distribution of interstitial pressure and that of blood flow in the tumour that currently doesn't exist.

(6) The current 'distributed source' models used to determine the spatial-temporal macromolecule concentrations in tumour have not been expanded to include the following cases:

(i) Two-step approaches (e.g. avidin-streptavidin chase), or even three step ones for macromolecule delivery to tumours (Goodwin *et al.* 1994). The binding affinity of the macromolecules, their m.w., and the time interval between their administration required to optimize the balance between spatial homogeneity of macromolecule distribution and total tumour uptake for different vascular distributions are parameters of interest.

(ii) Calculation of the macromolecule distribution if the method of its administration is other than intravenous, e.g. intraperitoneal for the therapy of ovarian tumours. In that case, the anti-cancer agent will diffuse into the tumour from its surface and transcapillary transport mechanics will be used to determine the agent's clearance out of the tumour rather than its passage into the tumour. Low m.w. agents will probably achieve deeper penetration in the tumour interstitium and a higher homogeneity of distribution, but at the same time will be cleared into the circulation faster. The latter will be the object of optimization in the relevant modelling. The calculated extravasation rate into the circulation can be linked to a pharmacokinetic model to calculate limits in toxicity of healthy organs.

(iii) In radioimmunotherapy regimens several bolus injections are administered at regular time intervals rather than a single large dose in order to limit the toxicity to healthy organs. This creates interest for three types of calculations:

(a) Prediction of the macromolecule concentration, spatial heterogeneity, and total tumour uptake as a function of time for different time intervals between injections.

(b) Development of a dynamic empirical model of tumour vasculature and cell growth, and remission due to the effect of tumour perfusion with anticancer agents. The type of calculations mentioned in (a) should be incorporated in this model.

(c) Calculations to correlate the radiolabelled macromolecule temporal-spatial distributions to their respective dose distributions. This can be achieved by convolving the calculated macromolecule distribution with a radiation dose point kernel (Leichner & Kwok 1993) characteristic of the isotope used. Estimates of the dose contribution of neighbouring organs to the tumour dose distribution can be incorporated. Once the dose distribution has been calculated , it can be correlated to survival curves specific to the cancer line, as well as to those of normal cells. Hence the spatial distribution of survival probability of cells inside the tumour and surrounding healthy tissue can be calculated. Lack of experimental data prevents correlation of the dose distribution to the spatial probability distribution of cancer causing mutations in surrounding healthy tissue. Since the tumours are usually observed to shrink after a treatment, it will be useful to incorporate the dynamic model mentioned in (b) and its effect on the spatial variation of the dose distribution. It is also interesting to look at the effect of varying the time interval between treatments, mentioned in (a), on the local percentage changes of the probability of survival of cancer cells. It would be essential to include the effect of radioimmunotherapy on endothelial cells in this kind of modelling as it seems to decrease blood vessel permeability with time (Blumenthal *et al.* 1995).

(7) There is no experimental data linking antigen metabolic rate and surface antigen concentration for different cancer lines (Baxter *et al.* 1994). Also, there is no quantification of antigen shedding and its effect on the bound antibody concentration. This is information needed both in compartmental and 'distributed source' models to calculate tumour uptake more accurately.

(8) Since both capillaries and lymphatics are constituted of endothelial cells, it is of interest to investigate why tumour angiogenesis stimulates growth of the former, but not of the latter. Pressure build-up in the tumour interstitium is one of the main reasons of poor tumour perfusion with anticancer agents. Inducing the growth of lymphatics in the tumour will release that pressure build-up. However, one has to investigate whether this advantage is offset by greatly increased macromolecule clearance and danger of metastasis.

APPENDIX I

For copies of the programs described in this thesis please contact:

George Alexandrakis
Hamilton Regional Cancer Centre
(4th floor, Research)
699 Concession Street
Hamilton, Ontario
L8V 5C2

REFERENCES

Ballard, K., and W. Perl 1978 Osmotic Reflection Coefficients of Canine Subcutaneous Adipose Tissue Endothelium, *Microvasc. Res.* **16** (224-236)

Ballmer-Weber, B.K., R. Dummer, E. Küng, G. Burg, and P.E. Ballmer 1995 Interleukin 2-induced increase of vascular permeability without decrease of the intravascular albumin pool, *BJC* **71 (1)** (78-82)

Bartolini, A., B. Gasparetto, M. Furlan, R. Amore, L. Sullo, and A. Tartaglione 1993 Functional Vascular Volume and Blood-Brain Barrier Permeability Images by Angio-CT in the Diagnosis of Cerebral Lesions, *Computerized Medical Imaging and Graphics* **17** (35-44)

Baxter, L.T., H. Zhu, D.G. Mackensen, W.F. Butler, and R.K. Jain 1995 Biodistribution of Monoclonal Antibodies: Scale-up from Mouse to Human Using a Physiologically Based Pharmacokinetic Model, *Cancer Res.* **55** (4611-4522)

Baxter, L.T., H. Zhu, D.G. Mackensen, and R.K. Jain 1994 Physiologically Based Pharmacokinetic Model for Specific and Nonspecific Monoclonal Antibodies and Fragments in Normal Tissues and Human Tumour Xenografts in Nude Mice, *Cancer Res.* **54** (1517-1528)

Baxter, L.T., F. Yan, R.K. Jain 1992 Pharmacokinetic Analysis of the Perivascular Distribution of Bifunctional Antibodies and Haptens: Comparison with Experimental Data, *Cancer Res.* **52** (5838-5844)

Baxter, L.T., and R.K. Jain 1989 Transport of Fluid and Macromolecules in Tumors (I. Role of Interstital Pressure and Convection), *Microvasc. Res.* **37** (77-104)

Baxter, L.T., and R.K. Jain 1990 Transport of Fluid and Macromolecules in Tumors (II. Role of Heterogenous Perfusion and Lymphatics), *Microvasc. Res.* **40** (246-263)

Baxter, L.T., and R.K. Jain 1991a Transport of Fluid and Macromolecules in Tumors (III. Role of Binding and Metabolism), *Microvasc. Res.* **41** (5-23)

Baxter, L.T., and R.K. Jain 1991b Transport of Fluid and Macromolecules in Tumors (IV. A Microscopic Model of the Perivascular Distribution), *Microvasc. Res.* **41** (252-272)

Blumenthal, R.D., R. Kashi, R.M. Sharkey, and D.M. Goldenberg 1995 Quantitative and Qualitative Effects of Experimental Radioimmunotherapy on Tumour Vascular Permeability, *Int. J. Cancer* **61** (557-566)

Bossi, P., G. Viale, A.K.C. Lee, R.M. Alfano, G. Coggi, and S. Bosari 1995 Angiogenesis in Colorectal Tumors: Microvessel Quantitation in Adenomas and Carcinomas with Clinopathological Correlations, *Cencer Res.* **55** (5049-5053)

Brace, R.A., and A.C. Guyton 1977 Interaction of Transcapillary Starling Forces in the Isolated Dog Forelimb, *Am. J. Physiol.* **233** (H136-H140)

Buist, M.R., P. Kenemans, C.F.M. Molthoff, J.C.Ross, W. Den Hollander, M. Brinkhuis, and J.P.A. Baak 1995 Tumor Uptake of Intravenously Administered Radiolabeled Antibodies in Ovarian Carcinoma Patients in Relation to Antigen Expression and Other Tumour Characteristics, *Int. J. Cancer (Pred. Oncol.)* **64** (92-98)

Buraggi, G.L., L. Callegaro, G. Mariani, A. Turrin, N. Cascinelli, A. Attili, E. Bombardieri, G. Terno, G. Plassio, M. Dovis, N. Mazzuca, P.G. Natali, G.A. Scasseliati, U. Rosa, and S. Ferrone 1985 Imaging with ^{131}I-Labeled Monoclonal Antibodies to a High Molecular Weight Melanoma-Associated Antigen in Patients with Melanoma: Efficacy of Whole Immunoglobulin and Its F(ab')$_2$ Fragments, *Cancer Res.* **45** (3378-3387)

Chamayou, J.M.F. 1982 Program for B-Spline Interpolation of Surfaces with Application to Computer Tomography, *Comput. Phys. Commun.* **27** (187-199)

Chappell, M.J., G.D. Thomas, K.R. Godfrey, and A.R. Bradwell 1991 Optimal Tumor Targeting by Antibodies: Development of a Mathematical Model, *J. Pharmacokin. Biopharm.* **19 (2)** (227-260)

Clauss, M.A., and R.K. Jain 1990 Interstitial Transport of Rabbit and Sheep Antibodies in Normal and Neoplastic Tissues, *Cancer Res.* **50** (3487-3492)

Covell, D.G., J. Barbet, O.D. Holton, C.D.V. Black, R.J. Parker, and J.N. Weinstein 1986 Pharmacokinetics of Monoclonal Immunoglobulin G_1, F(ab')$_2$, and Fab' in Mice, *Cancer Res.* **46** (3969-3978)

Curry, F.E., 1984 Mechanics and Thermodynamics of Transcapillary Exchange, in *"Handbook of Physiology, Section 2: The Cardiovacular System"* (E.M. Renkin and C.C. Michel, Eds.), (309-374), Amer. Physiol. Soc., Bethesda, MD

Curry, F.E., 1974 A Hydrodynamic Description of the Osmotic Reflection Coefficient with Application to the Pore Theory of Transcapillary Exchange, *Microvasc. Res.* **8** (236-252)

Deen, W.M., 1987 Hindered Transport of Large Molecules in Liquid Filled Pores, *AIChE Journal* **33 (9)** (1409-1425)

Dierckx, P. *Curve and Surface Fitting with Splines, Monographs on Numerical Analysis*, 1993, Oxford University Press

Dvorak, H.F., J.A. Nagy, J.T. Dvorak, and A.M. Dvorak 1988 Identification and Characterization of the Blood Vessels of Solid Tumors That Are Leaky to Circulating Macromolecules, *Am. J. Pathol.* **133 (1)** (95-109)

El-Kareh, A.W., and T.W. Secomb 1995 Effect of Increasing Vascular Hydraulic Conductivity on Delivery of Macromolecular Drugs to Tumor Cells, *Int. J. Radiation Oncology Biol. Phys.* **5** (1419-1423)

El-Kareh, A.W., S.L. Braunstein, and T.W. Secomb 1993 Effect of Cell Arrangement and Interstital Volume Fraction on the Diffusivity of Monoclonal Antibodies in Tissue, *Biophys. J.* **64** (1638-1646)

Fand, I., R.M. Sharkey, J.P. Grundy, and D.M. Goldenberg 1992 Localization by Whole-Body Autoradiography of Intact and Fragmented Radiolabeled Antibodies in a Metastatic Human Colonic Cancer Model, *Nucl. Med. Biol.* **19 (1)** (87-99)

Fleischman, G.J., T.W. Secomb, and J.F. Gross 1986 Effect of Extravascular Pressure Gradients on Capillary Fluid Exchange, *Math. Biosci.* **81** (145-164)

Fujimori, K. 1990 Heterogeneity of Monoclonal Antibody Distribution and Radiation Dose in Tumors: A Modelling Analysis, *Hokkaido Medical Journal* **66 (3)** (369-384)

Fujimori, K., D.G. Covell, J.E. Fletcher, and J.N. Weinstein 1990 A Modelling Analysis of Monoclonal Antibody Percolation Through Tumors: A Binding-Site Barrier, *J. Nucl. Med.* **31** (1191-1198)

Fujimori, K., D.G. Covell, J.E. Fletcher, and J.N. Weinstein 1989 Modelling Analysis of the Global and Microscopic Distribution of Immunoglobulin G, $F(ab')_2$, and Fab in Tumors, *Cancer Res.* **49** (5656-5663)

Gerald, C.F., P.O. Wheatley, *Applied Numerical Analysis*, (5th edition), Addison-Wesley Inc., 1991, Menlo Park CA, U.S.A.

Gerlowski, L.E., and R.K. Jain 1986 Microvascular Permeability of Normal and Neoplastic Tissues, *Microvasc. Res.* **31** (288-305)

Goodwin, D.A., C.F. Meares, N. Watanabe, M. McTigue, W. Chaovapong, C.McK. Ransone, O. Renn, D.P. Greiner, D.L. Kukis, and S.I.Kronenberger 1994 Pharmacokinetics of Pretargeted Monoclonal Antibody 2D12.5 and ^{88}Y-Janus-2-(p-Nitrobenzyl)-1,4,7,10-tetraazacyclododecanetetraacetic Acid (DOTA) in BALB/c

Mice with KHJJ Mouse Adenocarcinoma: A Model for ^{90}Y Radioimmunotherapy, *Cancer Res.* **54** (5937-5946)

Harkness, J.E., and J.E. Wagner *The Biology and Medicine of Rabbits and Rodents*, 2nd edition

Hagan, P.L., S.E. Halpern, R.O. Dillman, D.L. Shawler, D.E. Johnson, A. Chen, L. Krishnan, J. Frincke, R.M. Bartholomew, G.S. David, and D. Carlo 1986 Tumor Size: Effect in Monoclonal Antibody Uptake in Tumor Models, *J. Nucl. Med.* **27** (422-427)

Hamberg, L.M., P.E.G. Kristjansen, G.J. Hunter, G.L. Wolf, and R.K. Jain 1994 Spatial Heterogeneity in Tumor Perfusion Measured with Functional Computed Tomography at 0.05μl Resolution, *Cancer Res.* **54** (6032-6036)

Henri, C.J., and Peters T.M. 1996a Three-Dimensional Reconstruction of Vascular Trees. Theory and Methodology, *Med. Phys.* **23 (2)** (197-204)

Henri, C.J., and Peters T.M. 1996b Three-Dimensional Reconstruction of Vascular Trees: Experimental Evaluation, *Med. Phys.* **23 (5)** (617-627)

Hilmas, D.E., and E.L. Gillette 1974 Morphometric Analyses of the Microvasculature of Tumours During Growth and After X-Irradiation, *Cancer* **33** (103-110)

Hindmarsh, A.C. *Odepack, a Systematized Collection of ODE Solvers in Scientific Computing*, R.S. Stepleman *et al* editions, North-Holland, Amsterdam, 1983, pp. 55-64

Jain, R.K., and L.T. Baxter 1988 Mechanisms of Heterogeneous Distribution of Monoclonal Antibodies and Other Macromolecules in Tumors: Significance of Elevated Interstial Pressure, *Cancer Res.* **48** (7022-7032)

Jain, R.K. 1987a Transport of Molecules Across Tumor Vasculature, *Cancer Metast. Rev.* **6** (559-593)

Jain, R.K. 1987b Transport of Molecules in the Tumor Interstitium, *Cancer Res.* **47** (3039-3051)

Juweid, M., R. Neumann, C. Paik, M.J. Perez-Bacete, J. Sato, W. Van Osdol, and J.N. Weinstein 1992 Micropharmacology of Monoclonal Antibodies in Solid Tumors: Direct Experimental Evidence for a Binding Site Barrier, *Cancer Res.* **52** (5144-5153)

Kaufman, E.N., and R.K. Jain 1992 Effect of Bivalent Interaction upon Apparent Antibody Affinity: Experimental Confirmation of Theory Using Fluorescence Photobleaching and Implications for Antibody Binding Assays, *Cancer Res.* **52** (4157-4167)

Kaufman, E.N., and R.K. Jain 1991 Measurement of Mass Transport and Reaction Parameters in Bulk Solution Using Photobleaching, *Biophys. J.* **60** (596-610)

Kedem, O., and A. Katchalsky 1958 Thermodynamic Analysis of the Permeability of Biological Membranes to Non-Electrolytes, *Biochim. Biophys. Acta* **27** (229-246)

Kairemo, K.J.A., K. Ljunggren, T. Wahlström, T. Stigbrand, and S. Strand 1994 Correlation of Beta-Camera Imaging and Immunohistochemistry in Radioimmunotherapy Using ^{90}Y-Labelled Monoclonal Antibodies in Ovarian Cancer Animal Models, *Cell Biophys.* **24/25** (293-300)

Kobayashi, H., H. Sakahara, K. Endo, M. Hosono, Z. Yao, S. Toyama, and J. Konishi 1995 Comaprison of the Chase Effects of Avidin, Streptavidin, Neutravidin, and Avidin-Ferritin on a Radiolabeled Biotinylated Anti-Tumor Monoclonal Antibody, *Jpn. J. Cancer Res.* **86** (310-314)

Kobayashi, H., H. Sakahara, K. Endo, M. Hosono, Z. Yao, S. Toyama, and J. Konishi 1994 Improved Clearance of Radiolabeled Biotinylated Monoclonal Antibody Following the Infusion of Avidin as a "Chase" without Decreased Accumulation in the Target Tumor, *J. Nucl. Med.* **35** (1677-1684)

Kwok, C.S., J. Li, R. Maharajh, S. Gyorffy, G. Alexandrakis, S.E. Lee, M. Tinkl, V. Sniekus, V.V. Somayaji, and A.A. Noujaim 1996 Effect of Labelling Isotope on Monoclonal Antibody Dosimetry in Nude Mice Carrying Human Tumor Xenografts, Submitted to the *Proceedings of the 6th International Symposium of Radiopharmaceutical Dosimetry*, Oakridge TN, U.S.A.

Kwok, C.S., S.K. Yu, and S. Lee 1995 Mathematical Models of Antitumor Antibodies in Human Melanoma Spheroids, *Antibody, Immunoconjugates, and Radio-pharmaceuticals* **8 (3)** (155-169)

Kwok, C.S., A. Crivici, W.D. MacGregor, and M.W. Unger 1989 Optimization of Radioimmunotherapy Using Human Malignant Melanoma Multicell Spheroids as a Model, *Cancer Res.* **49** (3276-3281)

Landis, E.M., 1927 Micro-Injection Studies of Capillary Permeability: The Relation Between Capillary Pressure and the Rate at which Fluid Passes Through the Walls of Single Capillaries, *Am. J. Physiol.* **82 (2)** (217-238)

Leichner, P.K., and C.S. Kwok 1993 Tumour Dosimetry in Radioimmunotherapy: Methods of Calculation for Beta Particles, *Med. Phys.* **20 (2)** (529-534)

Levick, J.R. 1994 An Analysis of the Interaction Between Interstial Plasma Protein, Interstitial Flow, and Fenestral Filtration and Its Application to Syvonium, *Microvasc. Res.* **47** (90-125)

McFadden, R., and C.S. Kwok 1988 Mathematical Model of Simultaneous Diffusion and Binding of Antitumor Antibodies in Multicellular Human Tumor Spheroids, *Cancer Res.* **48** (4032-4037)

Messner, A.M., and G.Q. Taylor 1980 Algorithm 550 (Solid Polyhedron Measures), *ACM Transactions on Mathematical Software* **6 (1)** (121-130)

Michel, C.C. 1978 The Measurement of Permeability in Single Capillaries, *Arch. Int. Physiol. Biochim.* **86** (657-667)

Milici, A.J., N.E. Watrous, H. Stukenbrok, and G.E. Palade 1987 Transcytosis of Albumin in Capillary Endothelium, *J. Cell Biol.* **105 (6)** (2603-2612)

Pappenheimer, J.R., E.M. Renkin, and L.M. Borrero 1951 Filtration, Diffusion and Molecular Sieving Through Peripheral Capillary Membranes: A Contribution to the Pore Theory of Capillary Permeability, *Am. J. Physiol.* **82** (13-46)

Patlak, C.S., D.A. Goldstein, and J.F. Hoffman 1963 The Flow of Solute and Solvent Accross a Two-Membrane System, *J. Theor. Biol.* **5** (426-442)

Pavel, D.G., A.M. Zimmer, and V.N. Patterson 1977 In Vivo Labelling of Red Blood Cells with ^{99m}Tc: A New Approach to Blood Pool Visualization, *J. Nucl. Med.* **18** (305-308)

Peterson, H.I., L. Appelgren, G. Lundborg, and B. Bosengren 1972 Capillary Permeability of Two Transplantable Rat Tumors as Compared with Various Normal Organs of the Rat, *Proc. of the 7th Europ. Conf. Microcirculation, Aberdeen 1972, Part II (511-518).* (Karger, Basel 1973)

Peterson, H.I., L. Appelgren, M. Alpsten, L. Karlsson, A.B. Kullberg, J. Mattsson, and D. Selander 1984 Intratumor Distribution of Capillary Permeability Surface Area Product (PS) Correlated to Tumor Vascular Space and Blood Flow, *Microcirculation, Endothelium, and Lymphatics* **1** (491-507)

Rijken, P.F.J., H.J.J. Bernsen, and A.J. Van Der Kogel 1995 Application of an Image Analysis System to the Quantitation of Tumor Perfusion and Vascualrity in Human Glioma Xenografts, *Microvasc. Res.* **50** (141-153)

Rippe, B., and B. Haraldsson 1987 Fluid and Protein Fluxes Across Small and Large Pores in the Microvasculature. Application of Two-Pore Equations, *Acta Physiol. Scand.* **131** (411-428)

Rippe, B., A. Kamiya, and B. Folkow 1978 Simultaneous Measurements of Capillary Diffusion and Filtration Exchange During Shifts in Filtration-Absorption and at Graded Alterations in the Capillary Permeability Surface Area Product (PS), *Acta Physiol. Scand.* **104** (318-336)

Schiesser, W.E. *The Numerical Method of Lines: Integration of Partial Differential Equations*, Academic Press Inc., 1991, San Diego CA, U.S.A.

Sevick, E.M., and R.K. Jain 1991 Measurement of Capillary Filtration Coefficient in a Solid Tumor, *Cancer Res.* **51** (1352-1355)

Sharkey, R.M., C. Motta-Hennessy, D. Pawlyk, J.A. Siegel, and D.M. Goldenberg 1990 Biodistribution and Radiation Dose Estimates for Yttrium- and Iodine-Labelled Monoclonal Antibody IgG and Fragments in Nude Mice Bearing Human Colonic Tumor Xenografts, *Cancer Res.* **50** (2330-2336)

Shockley, T.R, K. Lin, C. Sung, J.A. Nagy, R.G. Tompkins, R.L. Dedrick, H.F. Dvorak, and M.L. Yarmush 1992 A Quantiative Analysis of Tumor Specific Monoclonal Antibody Uptake by Human Melanoma Xenografts: Effects of Antibody Immuonological Properties and Tumor Antigen Expression Levels, *Cancer Res.* **52** (357-366)

Song, C.W., and S.H. Levitt 1970 Effect of X-Irradiation on Vascularity of Normal Tissues and Experimental Tumor, *Radiol.* **94** (445-447)

Sung, C., W.W. Van Osdol, T. Saga, R.D. Neumann, R.L. Dedrick, and J.N. Weinstein 1994 Streptavidin Distribution in Metastatic Tumors Pretargeted with a Biotinylated Monoclonal Antibody: Theoretical and Experimental Pharmacokinetics, *Cancer Res.* **54** (2166-2175)

Sung, C., R.J. Youle, and R.L. Dedrick 1990 Pharmacokinetic Analysis of Immunotoxin Uptake in Solid Tumors: Role of Plasma Kinetics, Capillary Permeability, and Binding, *Cancer Res.* **50** (7382-7392)

Swabb, E.A., J. Wei, and P.M. Gullino 1974 Diffusion and Convection in Normal and Neoplastic Tissues, *Cancer Res.* **34** (2814-2822)

Sykulev, Y.K., D.A. Sherman, R.J. Cohen, and H.N. Eisen 1992 Quantitation of Reversible Binding by Particle Counting: Hapten-Antibody Interaction as a Model System, *Proc. Natl. Acad. Sci. USA (Immunology)* **89** (4703-4707)

Terada, T., K. Nambu, G. Hyotani, K. Miyamoto, M. Tsuura, Y. Nakamura, T. Nishiguchi, T. Itakura, S. Hayashi, and N. Komai 1992 A Method for Quantitative Measurement of Cerebral Vascular Permeability Using X-Ray CT and Iodinated Contrast Medium, *Neuroradiology* **34** (290-296)

Thomas, G.D., M.J. Chappel, P.W. Dykes, D.B. Ramsden, K.R. Godfrey, J.R.M. Ellis, and A.R. Bradwell 1989 Effect of Dose, Molecular Size, Affinity, and Protein Binding of Tumor Uptake of Antibody or Ligand: A Biomathematical Model, *Cancer Res.* **49** (3290-3296)

Tortora, G.J., and S.R. Grabowski 1993 *"Principles of Anatomy and Physiology"* (7th Edition, Harper-Collins, N.Y. U.S.A.

Van Osdol, W.W., C. Sung, R.L. Dedrick, and J.N. Weinstein 1993 A Distributed Pharmacokinetic Model of Two-Step Imaging and Treatment Protocols: Application to Streptavidin-Conjugated Monoclonal Antibodies and Radiolabelled Biotin, *J. Nucl. Med.* **34** (1522-1564)

Van Osdol, K. Fujimori, and J.N. Weinstein 1991 An Analysis of Monoclonal Antibody Distribution in Microscopic Tumor Nodules: Consequenses of a "Binding Site Barrier", *Cancer Res.* **51** (4776-4784)

Vogel C.A., A. Bischof-Delaloye, J.P. Pèlegrin, N. Hardman, B. Delaloye, and F. Buchegger 1993 Direct Comparison of a Radioiodinated Intact Chimeric anti-CEA Mab with its $F(ab')_2$ Fragment in Nude Mice Bearing Different Human Colon Cancer Xenografts, *Br. J. Cancer* **68** (684-690)

Wahl, R.L., C.W. Parker, and G.W. Philpott 1983 Improved Radioimaging and Tumor Localization with Monoclonal $F(ab')_2$, *J. Nucl. Med.* **24** (316-325)

Warnke, P.C., F.J. Hans, A. Korst, C. Mall, and C.B. Ostertag 1994 Simultaneous Measurement of Bidirectional Capillary Permeability, Vascular Volume, Extracellular Space, and rCBF in Experimental Gliomas and Surrounding Edema, *Acta Neurochir. (Suppl.)* **60** (341-343)

Wielderhielm, C.A. 1979 Dynamics of Capillary Fluid Exchange: A Nonlinear Computer Simulation, *Microvasc. Res.* **18** (48-82)

Williams, L.E., R.B. Duda, R.T. Proffitt, B.G. Beatty, J.D. Beatty, J.Y.C. Wong, J.E. Shively, and R.J. Paxton 1988 Tumor Uptake as a Function of Tumor Mass: A Mathematical Model, *J. Nucl. Med.* **29** (103-109)

Yu, D., J.K. Wolf, M. Scanlon, J.E. Price, and M.C. Hung 1993 Enhanced c-erbB-2/neu Expression in Human Ovarian Cancer Cells Correlates with More Severe Malignancy That Can Be Supressed by E1A, *Cancer Res.* **53** (891-898)

Yuan, F., L.T. Baxter, and R.K. Jain 1991 Pharmacokinetic Analysis of Two-Step Approaches Using Bifunctional and Enzyme-Conjugated Antibodies, *Cancer Res.* **51** (3119-3130)

Yuan, F., H.A. Salehi, Y. Boucher, U.S. Vasthare, R.F. Tuma, and R.K.Jain 1994a Vascular Permeability and Microcirculation of Gliomas and Mammary Carcinomas Transpalanted in Rat and Mouse Cranial Windows, *Cancer Res.* **54** (4564-4568)

Yuan, F., M. Leunig, S.K. Huang, D.A. Berk, D. Papadjopoulos, and R.K. Jain 1994b Microvascular Permeability and Interstitial Penetration of Sterically Stabilized (Stealth) Liposomes in a Human Tumor Xenograft, *Cancer Res.* **54** (3352-3356)

Yuan, F., M. Leunig, D.A. Berk, and R.K. Jain 1993 Microvascular Permeability of Albumin, Vascular Surface Area, and Vascular Volume Measured in Human Adenocarcinoma LS174T Using Dorsal Chamber in SCID Mice, *Microvasc. Res.* **45** (269-289)

Zlotecki, R.A., L.T. Baxter, Y. Boucher, and R.K. Jain 1995 Pharmacologic Modification of Tumor Blood Flow and Interstitial Fluid Pressure in a Human Tumor Xenograft: Network Analysis and Mechanistic Interpretation, *Microvasc. Res.* **50** (429-443)